UNIVERSITY BREMEN

FB5 - GEOSCIENCES

MASTER THESIS

---

# A first glimpse into the *EGRIP* ice core: An analysis of the influence of deformation and recrystallisation on fabric and microstructures of the *Northeast Greenland Ice Stream*

---

*Author:*
Nicolas STOLL
(3071802)

*Examiners:*
Prof. Dr. Angelika HUMBERT
PD. Dr. Frank LISKER
*Additional Supervisor:*
J. Prof. Dr. Ilka WEIKUSAT

*A thesis submitted in the study program*
*Master of Science Marine Geosciences,*
*conducted at*

Section of Glaciology
Alfred Wegener Institute
Helmholtz Centre for Polar and Marine Research

February 7, 2019

# Abstract

Global sea level has been rising over the last century, and one of the contributors and the main source of projection uncertainties is ice sheet mass loss by solid ice discharge. Projections currently lack sufficient confidence, partly due to the difficulty in simulating ice flow behaviour, which is highly influenced by deformation modes and the physical properties of ice, such as grain microstructure and c-axis orientation anisotropy.

This thesis aims to deliver an overview about the deformation regimes and microstructural properties, as well as crystal-preferred orientation (CPO) anisotropy, of the Northeast Greenland Ice Stream (NEGIS) by examining an ice core from the East Greenland Ice Core Project (EGRIP). Ice streams are major features to conduct the discharge from inland ice towards the coasts and NEGIS is the largest and most dominant one in Greenland. Therefore, microstructure and fabric data from almost 800 thin sections were analysed by an automated Fabric Analyser and a Large Area Scanning Macroscope. The result is an almost continuous record of the physical properties of the upper 1714 m of the ice core.

The major findings regarding crystal-preferred orientations are (1) a much more rapid evolution of c-axes anisotropy in shallow depths compared to lower dynamics sites and (2) partly novel characteristics in the CPO patterns. These findings are accompanied by highly irregular grain shapes, the regular occurrence of protruding grains and further indicators for an early onset of dynamic recrystallisation. Grain size values are similar to results from other ice cores and show an increase in grain size, followed by a strong decrease in the Glacial.

Until a depth of 196 m, a broad single maximum CPO was observed, indicating vertical compression from overlaying layers. A crossed girdle of Type I and Type II, observed in natural ice for the very first time, dominates until 294 m, probably caused by a fluctuation between non-coaxial and coaxial deformation, accompanied by simple shear and the activation of multiple slip-systems. Between 294 and 500 m a transition into a vertical girdle CPO occurs. Extensional deformation along flow leads to a distinct vertical girdle between 500 and 1150 m. This CPO pattern develops into a horizontal maxima CPO, also observed as a novel feature in polar ice, which is probably caused by additional simple shear.

This new microstructure and fabric information improves our understanding of ice dynamics, and should be considered in future ice flow law parameterisations to improve ice-sheet models.

# Acknowledgements

Finishing this thesis is somehow the consequence of the last three and a half years. From the first step into the section of glaciology at AWI, to the preparations conducted for the upcoming EGRIP season. So first of all, a big thank you to Ilka for all the possibilities and the trust you have put in me. I have learned a lot and was able to experience many things due to your support during the last years.
Furthermore, I would like to thank my examiners Angelika and Frank, who enabled me to write this atypical thesis, combining geology and glaciology.
EGRIP is such a big project and I am thankful to everyone involved in it, making it possible. A special thanks to all the members of the PP-team, who helped in gathering this data and therefore provided the basis of this thesis. Pia, Ernst, Julien and Tomotaka - it has been a pleasure to share the cave with you! Cheers Frederik, for always keeping up the spirits in the camp. I also want to thank Daniela, Johanna, Jan, Martyn and Paul for the assistance in finding my way through the complicated world of structural geology, especially when it comes to merging ice and quartz. Additionally, a big thank you to everyone who read this thesis, helping me along the way and definitely improving the final result.
Last but not least, many thanks to my gorgeous flat mates, my family and especially Sonja for all the support during the last months.

# Contents

# List of Figures

# List of Tables

# List of Abbreviations

| | |
|---|---|
| **AWI** | **A**lfred **W**egener **I**nstitute Helmholtz Centre for Polar and Marine Research |
| **CCD** | **C**harge **C**oupled **D**evice |
| **CPO** | **C**rystal **P**referred **O**rientation |
| **DEP** | **Die**lectric **P**rofiling |
| **ECM** | **E**lectrical **C**onductivity **M**ethod |
| **EGRIP** | **E**ast **Gr**eenland **I**ce Core **P**roject |
| **EDML** | EPICA **D**ronning **M**aud **L**and |
| **FA** | **F**abric **A**nalyser |
| **GRIP** | **Gr**eenland **I**ce Core **P**roject |
| **GrIS** | **Gr**eenland **I**ce **S**heet |
| **LASM** | **L**arge **A**rea **S**canning **M**acroscope |
| **NEEM** | **N**orth Greenland **Eem**ian Ice Drilling |
| **NEGIS** | **N**orth**e**ast **G**eeenland **I**ce **S**tream |
| **NGRIP** | **N**orth **Gr**eenland **I**ce Core **P**roject |
| **pRES** | **p**hase-sensitive **R**adio **E**cho **S**ounding |

# 1 Introduction

## 1.1 Ice and its deformation

Ice is a special mineral and a broad overview about its relevant properties is given in this chapter. Nontrivial but important terms, such as *basal plane*, *c-axis* and *slip-system*, are explained.

### 1.1.1 The structure of ice

One oxygen and two hydrogen atoms are the essence of a water molecule, resulting in several important features of water, such as its polar nature and its characteristic hydrogen bonds. There are twelve solid phases of water, but the natural conditions on the surface of the Earth allow only one stable form, ice $I_h$ with an ordinary hexagonal form (Petrenko and Whitworth, 1999). Its rather open lattice, with an atomic packing factor of less than 34%, accounts for the pressure-induced reduction of its melting point at high temperatures and its unusual low density (compared to water in its liquid state) (Schulson and Duval, 2009). Each oxygen atom of the ice lattice (from now on "ice" always refers to hexagonal ice $I_h$) is surrounded by four hydrogen atoms, forming a regular tetrahedron (Figure 1.1). On the one side, hydrogen atoms are covalently bonded to an oxygen atom, while they are also linked to another hydrogen atom via hydrogen bonding on the other side. These bonds create a hexagonal crystal structure, similar to zinc blende (ZnS). At $-20°$C, the dimensions of the unit cell are: a= 4.5169 Å and c= 7.3570 Å (Hobbs, 1974).

The relatively open lattice of ice is constructed of two principal axes: the vertical *c-axis* (or optical axis) and three *a-axes*. a-axes are separated by 120° and normal to the c-axis, which is the major axis of symmetry of the mechanical and elastic properties of a crystal (Petrenko and Whitworth, 1999). The water molecules are arranged in layers of hexagonal rings parallel to the (0001) plane. These are the basal planes of the crystal and perpendicular to the c-axis (Duval et al., 1983) as displayed in Figure 1.1.

This thesis will mainly investigate different orientations of the c-axis found in ice crystals from Northeast Greenland, aiming to derive information about the local deformation history.

### 1.1.2 Polycrystalline ice and its formation

Each part of the terrestrial cryosphere, from small glaciers to vast ice sheets, is a product of snow accumulation followed by firn compaction. Fresh snow accumulates and increases the pressure on older layers of snow, consisting of an uncountable amount of single snow grains. Depending on the surrounding climatic conditions, the density ($\delta$) of fresh snow varies from $\delta$=50–100 $kg\,m^{-3}$. After settling, snow grains get newly arranged by grain-boundary sliding, which is driven by densification due to increasing pressure from overlaying snow layers ($\delta$=200–300 $kg\,m^{-3}$). Further rounding of the grains, removing of their spires and enhanced intergranular bonding is caused by transport mechanisms and surface diffusion (Gow, 1974). This process of densification is divided into three stages, leading eventually to the transition from loose snow into compact, porous and air permeable firn. In the first stage, density increases by settling and physical compaction of grains until $\delta$=550 $kg\,m^{-3}$. From this point on, grains cannot be packed tighter and the *critical density* is reached. This normally occurs in the uppermost 20 m of a firn column. The corresponding depth is called *critical depth*. *Sintering* is the major densification process in the following stage, which lowers the pressure stress by crystallisation and deformation of ice crystals ($\delta$=550–820 $kg\,m^{-3}$). Snow has finally turned into ice and air channels, connected to the surface, start to close off at $\delta$=830 $kg\,m^{-3}$. Air bubbles are formed in this firn-ice transition zone and their internal chemistry stays preserved because interaction with the atmosphere is no longer possible. This trapped air contains a sample of the atmosphere, and therefore information about past temperature and other aspects of the environment. For pure glacier ice $\delta$=917 $kg\,m^{-3}$, but values can reach up to $\delta$=923 $kg\,m^{-3}$ at mid-depths ranges in ice sheets (Cuffey and Paterson, 2010).

*Material creep*, the plastic deformation of a solid body under the influence of stress, further compresses existing air bubbles until the air pressure exceeds the dissociation limit. At this stage, normally occurring at a depth of 800 to 1000 metres, air bubbles disappear and the leftover air molecules are stored within a *clathrate hydrate* crystal structure (Paterson, 1994).

Due to the mentioned processes, glacial ice consists of a large number of ice crystals, also termed *grains*. There is a strong spatial and temporal variation of grain size, shape (*texture*) and lattice orientation (*fabric*), e.g grain size typically varies from diameters of less than a millimetre to up to several centimetres. Between grains, planar lattice defects create *grain boundaries*, which consist of molecules not following crystal alignment rules (Cuffey and Paterson, 2010).

### 1.1.3 The creep of ice

The plastic deformation of ice under the influence of stress leads to material characteristics similar to a viscous fluid. The viscosity of ice is very high and amounts to $10^4$ Pas at $-10°$C (Cuffey and Paterson, 2010).

Ice sheets and glaciers are large bodies of ice, deforming under their own weight and therefore, exhibiting plastic flow. Flow normally occurs from high regions down to valleys or coast lines, affected by viscosity alterations, which are caused by variable impurity contents (e.g. dust). This redistribution of mass depends on several aspects, the most important ones are the ice crystal structure (small scale) and the bedrock topography (large scale). Here, only the first one will be explained in detail and it is referred to Cuffey and Paterson (2010) for more information on the influence of bedrock topography.

On geological time scales, single crystals in an ice body deform, even under very low stresses. The orientation of the c-axis of an ice crystal is crucial for its deformation. Each individual grain has a high mechanical anisotropy and crystals with favourable orientations will deform first. Deformation along the basal plane (*easy glide*) is activated much easier than along a different plane (*hard glide*), resulting in higher deformation/movement if stress is applied perpendicular to the c-axis (*basal slip*) (Figure 1.1). This is caused by the strong bonds between molecules in the same basal plane, and the strong anisotropy of the plasticity of monocrystalline ice, facilitating or hampering the process of deformation (Duval et al., 1983). Once stress is applied, deformation along the basal plane is 60-100 times easier than along a different plane, resulting in basal glide and grain deformation (Ashby and Duval, 1985). This pattern is nicely displayed by thinking about the easiest way to deform a deck of cards. Vertically compressing it, requires a large amount of strength while sliding the cards sideways, deforms the deck without overcoming much resistance.

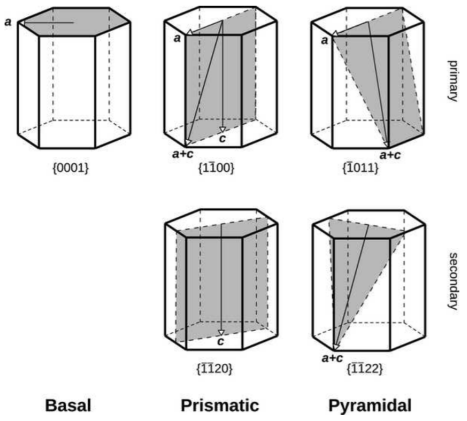


FIGURE 1.1: **Planes in a hexagonal crystal**

Different planes in a hexagonal crystal, such as ice. After Hondoh (2000), displayed by Faria et al. (2014b).

### 1.1.4 The fundamentals of dislocation theory and slip-systems

*Dislocations* can cause basal slip by moving through the crystal lattice and introducing additional half-planes to it, which results in linear lattice discontinuities. The *Burgers vector* is the vector between the start and the end location of a dislocation circuit, describing the character of a dislocation. The two most common dislocation

types are screw and edge dislocations (Figure A.1). The first one is characterised by a Burgers vector parallel to the dislocation line. The Burgers vector of an edge dislocation is perpendicular to the dislocation line. Screw and edge, and several more complex, dislocations move easily through the crystal lattice, enabling the slip of two parts of the lattice against each other, resulting in crystal deformation (*dislocation creep*). Slip-systems are combinations of slip planes, densely packed planes of the crystal, and slip directions, crystallographic directions with the shortest distance between ions or atoms (Jackson, 1991). In ice, dislocation creep occurs normally along the basal slip system and much higher stresses are required to activate non-basal slip-systems, such as on prismatic or pyramidal planes (Weertman and Weertman, 1992).

### 1.1.5 Recrystallisation

Crystal defects, such as dislocations and grain boundaries, are the result of bodies (e.g. ice sheets and rocks) storing free energy (e.g. intragranular lattice defect energy, grain boundary energy and chemical free energy). To reduce these vast amounts of energy, recrystallisation mechanisms occur and are therefore present in ice sheets or glaciers. Ice is constantly flowing, which results in deformation and recrystallisation during this process. Therefore it is termed *syntectonic* or *dynamic recrystallisation*. It is defined as the formation and/or migration of grain boundaries, often leading to the formation of new grains at the cost of older grains. The two basic regimes of dynamic recrystallisation are *grain boundary migration* and *rotation recrystallisation*. Processes, where deformation is absent, are *static recrystallisation* and *normal grain growth* (Urai et al., 1986).

- *Static Recrystallisation* occurs before of after deformation and is driven by grain boundary surface reduction.
- *Normal Grain Growth* occurs in the upper hundred metres below the surface of an ice sheet. Here, grain area increases linearly with time, driven by the reduction of internal free energy of grain boundaries. To achieve this, the total grain boundary area and its curvature must decrease. Normal grain growth is replaced by rotation recrystallisation under the following circumstances.
- *Rotation Recrystallisation* occurs when heterogenous local stresses start to bend grains. Dislocation glide sets in, if the orientation is favourable, and dislocations align. This results in the formation of a discontinuity in the crystal orientation and a new boundary originates. Further rotation of the two subgrains leads to an increasing misorientation angle until a regular high-angle boundary is fully developed between the grains.
- *Grain Boundary Migration* describes the mobility of grain boundaries, mainly controlled by temperature, pressure, crystal structure and impurity content in and around the grains. In ice, the main driver is the reduction of lattice energy

stored in point defects, dislocations and subgrain boundaries. It is common for grain boundaries to move towards regions with a high dislocation density (Drury and Urai, 1990).

### 1.1.6 Crystal Preferred Orientation

Information about the c-axis distribution is normally plotted using Schmidt nets, displaying the *crystal preferred orientation* (CPO) of a sample. It is a two-dimensional equal-area hemispherical projection of a sphere, in which every c-axis of the analysed sample is displayed as a point on the sphere. For all used samples, the vertical axis of the sphere is parallel to the axis of the ice core. CPOs are used to derive information about deformation modes in rocks and ice. During the last decades, it has been established that certain CPO patterns are caused by defined deformation mechanisms (Borradaile, 2003).

Ice core drilling is an expensive and challenging undertaking, which results in a small total number of ice cores which can be analysed regarding CPO patterns. All completed deep ice core drillings were conducted in similar conditions regarding deformation and ice dynamics, and therefore comparably few CPO patters have been observed. For other minerals (e.g. quartz), a large amount of CPO pattern has been observed and several interpretations of their origins can be found in the literature, e.g. by Lister and Williams (1979). A relatively common CPO for quartz is the *crossed girdle* of *Type I* and *Type II* (Figure 1.2). Two main hypotheses for its origin are:

1. Lister and Dornsiepen (1982) stated that the thermodynamic activation of multiple slip systems should be one of the most important factors affecting the nature of c-axis fabrics.

2. Kamb (1972) and Alley (1992) proposed the importance of dynamic migration recrystallisation under horizontal uniaxial extension.

In 2017, this crossed girdle CPO was observed for the very first time in an ice core. This thesis aims to find hints in the fabric and the microstructure, explaining this novel occurrence.

## 1.2 Ice dynamics

### 1.2.1 The Cryosphere

The most abundant mineral on the surface of our planet is ice, the main component of the cryosphere. The cryosphere is the frozen, or glacial, part of the global climate system and is therefore of major importance, interacting with and depending on the other sub-systems. The components of the cryosphere are highly sensitive to temperature change, resulting in a high vulnerability to climate change (IPCC, 2013).

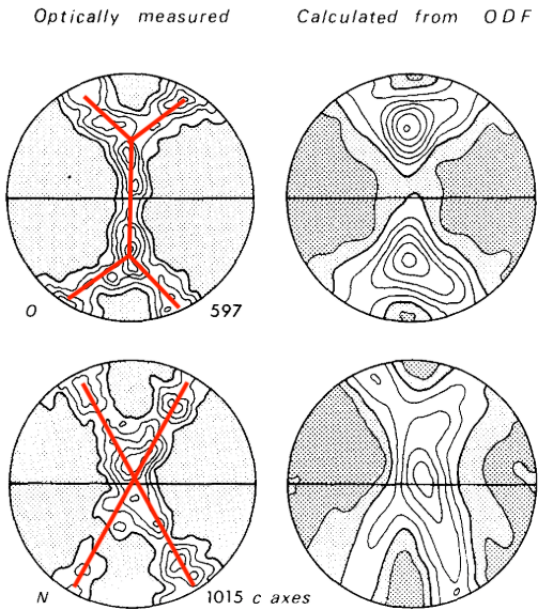


FIGURE 1.2: **Crossed girdle Type I and II**

Observed and calculated crossed girdles for quartz, the first row displays Type I and the second row Type II. The example of Type II is slightly asymmetric, and one part of the cross is stronger developed than the neighbouring one. Modified from Law et al. (1986).

The cryosphere consists of several parts, its terrestrial subsystems are flowing ice masses resting on solid ground: glaciers, ice caps and ice sheets (Greve, 2005). Ice bodies larger than 50 000 $km^2$ are termed ice sheets, or continental glaciers, which cover surrounding terrain. Greenland and Antarctica are the only currently existing ice sheets, both with parts of a thickness of ice of more than 3000 m. Ice caps are land-based ice masses covering less than 50 000 $km^2$, unconstrained by the underlying topography and often located in highland areas (e.g. Vatnajökull, Iceland) (Benn and Evans, 2010). Glaciers are smaller than ice caps and are located in mountain ranges on every single continent. There are roughly 160 000 glaciers on Earth, varying in size and volume, but usually constrained by topographical features (Monroe, 2009; Benn and Evans, 2010). 75% of the total fresh water on Earth is stored in glacial ice, covering 10% of the planet's surface. The produced melt water from melting glacial ice is estimated to account for nearly two-thirds of the observed global sea-level rise (Benn and Evans, 2010).

All of the mentioned ice bodies are dynamic systems, which flow and behave like viscoplastic fluids. This flow is caused partly by gravity-induced ice deformation and partly by sliding over lubricated bedrock. Vast parts of ice sheets and ice caps only flow with a velocity of several metres per year, while the most dynamic areas move much faster with up to 3000 metres per year (Figure 1.3). The latter statement holds true for ice streams, highly dynamic ice bodies which are introduced in Chapter 1.2.2 (Joughin et al., 1999; Margold et al., 2015).

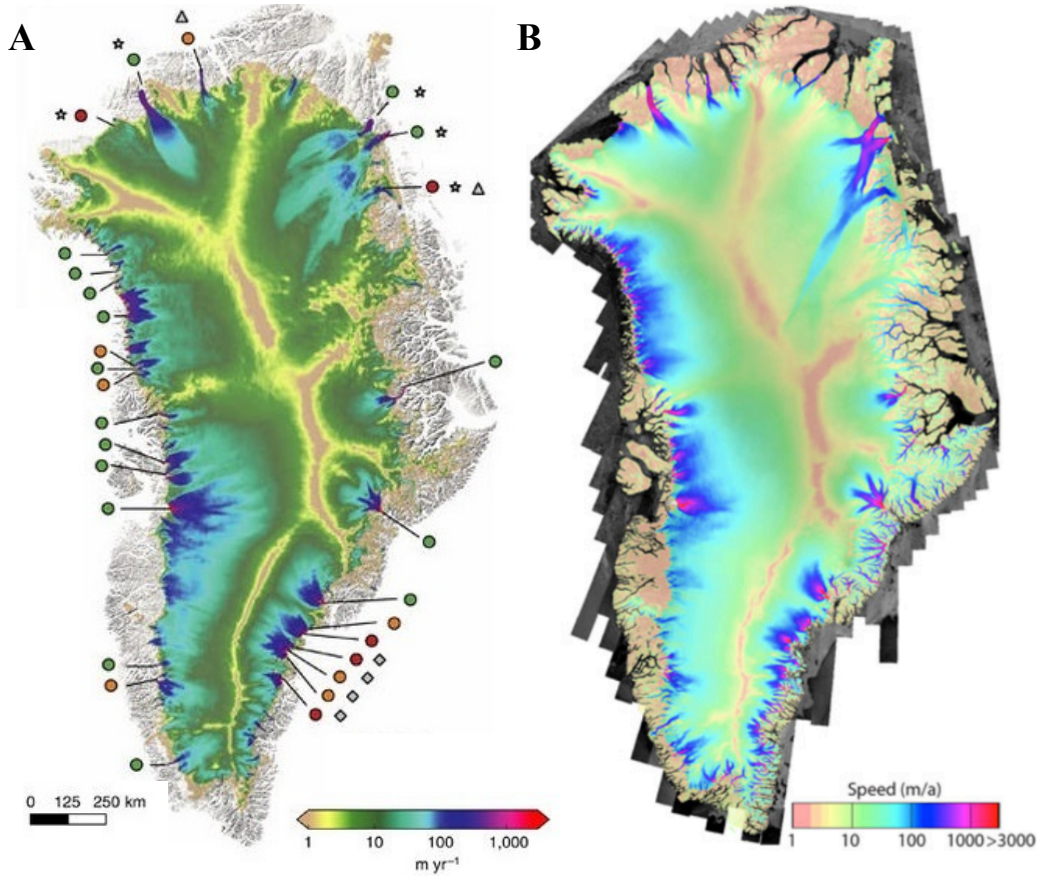


FIGURE 1.3: **Modelled and measured ice velocities of Greenland**

(A) Modelled ice flow velocities as presented by Aschwanden et al. (2016). Filled circles, diamonds and stars represent different glacier-types and correlation coefficients, which are further explained in Aschwanden et al. (2016) (B) Shown is a compilation of measured ice velocities derived from satellite data over 20 years (Joughin et al., 2017). Colours and absolute velocity ranges are different in each legend.

### 1.2.2 Ice streams

The two main processes contributing to ice sheet mass loss are melting and dynamic discharge of solid ice into the ocean, often via rapidly flowing ice streams (Margold et al., 2015). By studying ice sheet velocities, Joughin et al. (1999) and Rignot et al. (2011) were able to reveal ice stream patterns in Antarctica, as well as for Greenland (Joughin et al., 2010). The major pattern is similar for both ice sheets: smaller tributaries extend into the interior of the ice sheet and feed the main ice stream trunks (Figure 1.3). Recent studies reveal that ice streams account for approximately 90% and 50% of total mass loss of Antarctica and Greenland, respectively (Bamber et al., 2000; Broeke et al., 2009). Joughin et al. (2010) and Rignot et al. (2011) report typical ice stream flow velocities of a few metres per year in the ice sheet interior, increasing towards their termini to up to three thousand metres per year. These high velocities are caused by two major reasons, a weak bed of fine-grained, saturated sediment (pure type) or the existence of large topographic troughs filled with sediments and basal meltwater (topographic type) (Alley et al., 1986; Bentley, 1987; Payne, 1999).

In reality, these two types are only ideal end members and several transitional types can be observed. Furthermore, spatial and temporal properties (e.g. changes in flow velocity and trajectory, periods of flow and non-flow) of ice streams are highly variable (Conway et al., 2002; Joughin et al., 2003). This variability is caused by internal forcing (e.g. the availability and amount of till and lubricant water) or external forcing (e.g. changes in oceanic or atmospheric conditions) (Bennett, 2003). Climatically forced melting is a rather linear process, while the dynamics of ice streams add a significant non-linearity to the behaviour of ice sheets experiencing external forcing (Stokes et al., 2016). Therefore, understanding the physics and mechanisms behind increased ice stream discharge is of major importance due to their contribution to sea level rise (IPCC, 2013; Nick et al., 2013; Stokes et al., 2016).

### 1.2.3 The Northeast Greenland Ice Stream

The *Northeast Greenland Ice Stream* (NEGIS) (Figure 1.4) is the only ice stream in Greenland extending far into the interior, making it the largest ice stream of the *Greenland Ice Sheet* (GrIS) (Joughin et al., 2010). Its onset is located at the central ice divide and it flows 1000 km downstream until its terminus: the three outlet glaciers *Nioghalvfjerds isstrommen*, *Zachariae isbrae* and *Storstrommen* (Vallelonga et al., 2014). Studies by Fahnestock et al. (1993) and Fahnestock et al. (2001) identified the ice stream and allowed evaluations of the mass balance, basal characteristics and the velocity of NEGIS. Fahnestock et al. (2001) reports a regionally high geothermal heat flux at the ice divide causing strong basal melt, enhanced lubrication and fast flow and therefore the onset of NEGIS. Approximately 200 km downstream from its onset, the ice stream accelerates to 65 m/yr and to more than 1000 m/yr close to its termini (Joughin et al., 2017). The relatively recent discovery of NEGIS by Fahnestock et al. (1993) and the, hence, limited availability of field data about it, leads to a lot of questions regarding its role in the mass balance of GrIS (Vallelonga et al., 2014).

Deep ice cores are one possibility, to tackle the challenge of understanding NEGIS better, by extracting samples throughout the entire ice column, enabling detailed analysis of the physical properties. This is only possible due to the progress of ice core science and deep drilling over the last decades.

## 1.3 The evolution of polar microstructure analysis

This section gives a brief overview of the history of ice core science by only pointing out a few milestones and is far from being complete. Without a doubt, this is an unjust treatment to all unnamed men and women, who contributed many years of pioneering work.

The first scientific expedition interested in the microstructure of snow and ice was to the *Jungfraujoch* glacier in 1937, which led to many fundamental laws and

principles concerning the structure, mechanics and thermodynamics of snow, firn and ice (Perutz and Seligman, 1939; Seligman, 1941). These studies resulted in a broader scientific interest in the microstructure of ice and were followed by several expeditions to glaciers all around the globe. The discovery of the correlation between the amount of heavy oxygen isotopes in precipitation and the temperature at the location of precipitation by Dansgaard (1952), established the beginning of a novel research field of glaciology: ice core science. Several scientists developed the idea to retrieve ice cores, from glaciers and ice sheets, to study the climate of the past. Since this is a technically and logistically demanding task, in early years, only shallow ice cores were recovered. Dansgaard's discovery enhanced the need for science to drill deep ice cores, allowing to go further back in time (Faria et al., 2014a). Followed by the success of the International Geophysical Year (1957-1958) and a rapid development in drilling technology and analytic methods, the retrieving of deep ice cores became high-priority long-term research projects for the United States of America (Henri, 1962; Gow and Williamson, 1976).

Crystallographic and microstructural analyses were performed on the first deep ice cores reaching bedrock, the *Camp Century* core from Greenland (1963–1966) and the *Byrd station* core from Antarctica (1966–1968) (Herron et al., 1979; Herron and Langway, 1982). These operations proved that drilling through kilometres of creeping ice was possible, resulting in the *Greenland Ice Sheet Program* by the United States, Switzerland and Denmark. The retrieved *Dye 3* core was the first step to also establish European research programs, aiming to drill deep ice cores and to perform climate research (Langway et al., 1985; Faria et al., 2014a).

The last decades have been fairly successful and several deep ice cores were retrieved from both ice sheets by international teams of researchers. Figure 1.4 displays successful drilling operations in Greenland. The following recent studies on deep ice cores analysed microstructure and fabric:

- *Greenland Ice Core Project* (GRIP) by Thorsteinsson (1996) and Thorsteinsson et al. (1997),
- *North Greenland Ice Core Project* (NGRIP) by Wang et al. (2002),
- *EPICA Dronning Maud Land* (EDML) by Weikusat et al. (2009b) and Weikusat et al. (2017),
- *North Greenland Ice Core Project* (NEEM) by Eichler (2013) and Montagnat et al. (2014).

This thesis is based on the fundamentals established by decades of ice core science and microstructural analysis, but somehow approaches *terra incognita* by examining the first ice core from a fast flowing ice stream. The *East Greenland Ice Core Project* (EGRIP) makes it possible to study ice from such a dynamic site and lays the foundation for this thesis.

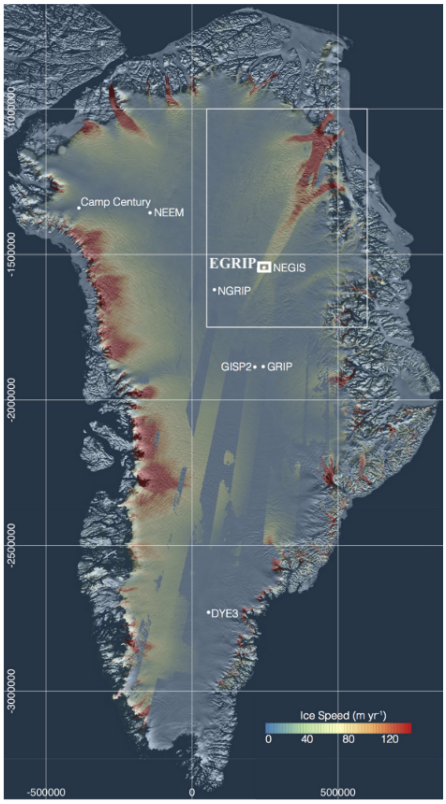


FIGURE 1.4: **Locations of deep ice core drilling sites in Greenland**

Locations of deep ice core drilling sites in Greenland are marked, modified from Vallelonga et al. (2014). The large white rectangle denotes the area of the Northeast Greenland Ice Stream. The location of the East Greenland Ice-Core Project (EGRIP) is indicated with a thick-lined rectangle. Colours represent ice speed velocities and were derived by interferomtric synthetic aperture radar.

## 1.4 Aim of this thesis

After several decades of glaciology and deep ice core drilling, the EGRIP ice core is the first ice core derived from a fast flowing ice stream. Obtaining an ice core from such a dynamic location is a difficult, but promising project in many ways. After two successful seasons and the exhumation of 1750 m of good quality core, it is finally possible to take a detailed look into the interior of an ice stream. Combining the slightly different approaches and views of structural geology and ice core science, this thesis aims to be a first step towards a better understanding of the dynamics, flow and material behaviour (*rheology*) of ice. Therefore, traditional methods from structural geology are applied to the "hot" topic of ice, allowing to examine fabric and microstructure of ice with a dynamic deformation history. These physical properties appear tremendously small-scaled, compared to the dimensions of ice sheets or ice streams. The material behaviour of ice, depending on these properties, is essential for ice flow and therefore a crucial boundary condition, e.g. for postulated flow laws and numerical models incorporating ice. This topic has been heavily discussed since Glen (1952) and Nye (1953) proposed a flow law for ice, which is still the base for many ice sheet models.

Major progress was made in terms of ice-flow modelling, but the basic mechanisms are still far from being sufficiently understood. According to IPCC (2013), models are still not able to simulate ice flow behaviour, and hence solid ice discharge into the ocean, with satisfying confidence, as displayed in Figure 1.3. It is crucial, in times of global climate change, to understand these processes in order to project future sea-level rise.

This thesis tries to lay the foundation for further work, regarding ice flow, by addressing the following research questions:

- What are the physical properties of the upper 1714 m of the EGRIP ice core?
- What are the crystal-preferred orientations throughout the core and what deformation history can be derived from this information?
- Crossed girdle CPOs have been observed in quartz before and were explained by an early onset of dynamic recrystallisation, and/or the activation of multiple slips-systems. Is there evidence in the upper part of the EGRIP ice core, indicating similar processes explaining this novel CPO pattern?

To answer these questions, thick and thin sections of ice were fabricated at the EGRIP camp during the 2017 and 2018 season. High-resolution images were taken by a *Large Area Scanning Macroscope* (LASM) and c-axis distributions were measured by an automated *Fabric Analyser* (FA). The derived data was processed at the *Alfred Wegener Institute Helmholtz Centre for Marine and Polar Research* (AWI) in Bremerhaven, Germany. The processed data was used to derive information about the physical properties of ice at the EGRIP site, at a depth range between 111 m and 1714 m.

The focus of my thesis lies on the analysis of crystal-preferred orientations obtained by polarised-light microscopy, allowing unique insights into the deformation modes occurring in ice streams. The evolution of the 2nd-order orientation tensor eigenvalues will be analysed and compared to older ice cores from lower dynamic sites, such as EDML, GRIP and NEEM. Furthermore, CPO patterns will be analysed aiming to establish a first record of the deformation history of NEGIS. This is combined with high-resolution images, enabling detailed investigations of grain shape and grain boundaries and therefore the possibility to find distinct deformation and dynamic recrystallisation features in the microstructure.

This will help to further examine the hypothesis about the origin of the occurrence of a novel CPO pattern, which has not been observed in ice before. Further data about eigenvectors, grain parameters and the visual analysis of microstructure will be used in this thesis to address the research questions mentioned above.

# 2 Working Area, Methods and Data

## 2.1 Working Area and the East Greenland Ice Core Project

The East Greenland Ice-Core Project is an international undertaking with the aim to retrieve a deep ice core from the fast flowing ice stream NEGIS. It is an, logistically and scientifically, international cooperation in the field and an ongoing close cooperation during sample analysis and data processing. EGRIP is coordinated by the Centre for Ice and Climate at the Niels Bohr Institute, University of Copenhagen and major partners are Germany, Japan, Norway, Switzerland, the United States of America and France. At the start of drilling, the drill site was located at 75°37.820 N and 35°59.556 W, 440 kilometres to the South-East of the old NEEM camp (Figure 1.4). It has been moving to the northeast due to its location on an ice stream. It is far enough away from the heavily crevassed margin at the coast to offer a safe working location, being the base for several research projects in the area (Petersen, 2016).

The project started in 2015 and during the first season, equipment, vehicles and buildings were transported from the old NEEM camp to the new site. In 2016, the camp, its runway and all needed logistics were constructed, electricity installed, the drill trench prepared and first drillings were conducted. A year later, full-time drilling started and 650 metres of good-quality ice were retrieved and partly processed (Petersen, 2016). Physical properties data from 2017 was processed after this season at AWI. This thesis continues, and builds upon, previous works.

In 2018, drilling continued successfully and 1750 metres of core were drilled, logged and partly processed by mid-August 2018. Microstructure and fabric have been analysed until a final depth of 1714 m. My investigated samples include all physical properties measurements from 2017 (275 measurements) and 2018 (522 measurements), consisting of 744 vertical and 53 horizontal thin sections. I was preparing samples and conducting measurements at the EGRIP camp between 29 June and 9 August 2018. In May 2019, the next season of drilling is planned to start. To reach bedrock at a depth of approximately 2550 m, further 800 metres of ice have to be drilled through.

The phenomena of the *brittle ice zone* Neff (2014) results in the lack of data between 900 and 1063 m. In Greenland, this zone is reported to appear averagely at a depth of 545±162 - 1132±178 m. The increasing overburden pressure from above results in pressurised air bubbles, which can fracture the core during its exposure to

atmospheric pressure. These fractures have the potential to degrade analyses, cause contamination and to reduce resolution (Neff, 2014). Therefore, ice from this depth regime is usually stored in a core buffer for several months (e.g. until the next season)(Figure A.3), and not processed until relaxation has occurred and the potential risk of damaging the samples is minimised. At EGRIP, large parts of the brittle zone were therefore processed in 2018 and the remaining 163 m are on the agenda for 2019.

## 2.2 Laboratory work and sample preparation

For a combined analysis of fabric and microstructure, it is necessary to fabricate thick and thin sections of ice (Figure A.2). These vary in size, depending on the ice core cut, but typical sizes for vertical thin sections are 96 x 70 x 0.3 mm. Thick sections are 96 x 70 mm, but the thickness varies from sample to sample and is in a range of 130 mm to 160 mm. Measurements were conducted every 10-15 m. Roughly every 100 m, a special volume sample was processed. In 2018, nine of these volume samples were cut into three vertical sections and two horizontal sections. The size of these vertical sections is similar to the dimensions mentioned above, only the width varied significantly from 30 to 83 mm due to the geometry of the sample. Horizontal sections had dimensions of 100 x 60 x 0.3 mm. Vertical samples were cut parallel to the main axis of the core. Horizontal samples were cut orthogonal to the core. At the EGRIP drill site, retrieved ice cores were stored and sampled in a snow trench approximately 8 metres below the surface. This resulted in temperatures seldom exceeding $-15°C$ to preserve original textures and fabrics, and prevent recrystallisation from occuring (Gow, 1994).

The preparation of ice thin sections is a time-consuming manual process, which was done directly in the field at the EGRIP site. The exhumation of the ice from the bore-hole leads to temperature changes and a strong decrease in hydrostatic pressure, resulting in material relaxation effects. Therefore, in-situ measurements were preferred to measurements in the ice laboratory at AWI.

The first step is the cutting of a 55 cm long piece of ice core, the so called "bag". A band saw was used to cut this bag manually into six small pieces of similar size, depending on the quality of the ice (e.g. cracks or breaks in the ice resulted in adjusted sample dimensions). Each sample was glued to a clean glass plate by applying a small amount of water on the edges of the sample, while putting a constant amount of pressure on it. For a stronger contrast at the following measurement, a black cloth was placed beneath the sample. A Leica microtome sledge (Figure 2.1), including a thick glass stage to fix the sample on, was used to polish the surface of the sample ("thick section"). This device was originally developed for the preparation of medical and biological thin sections. It consists of a mobile stage and an implemented sharp blade, which is repeatedly pushed across the surface of the sample. This procedure delicately takes off thin layers of ice, without scratching or damaging the

sample, while raising the stage slowly (10–20 $\mu$m). A micrometer screw allows the precise adjustment of the distance between the blade and the stage. After cutting off 1 mm, the surface is even and smaller steps were used to give the surface a final polishing (1–5 $\mu$m steps). The entire process takes about 15 minutes, depending on the size and surface unevenness of the sample. The sample was stored in a covered cupboard to minimise the ice-air interaction during sublimation, which took between one and four hours, depending on the properties and exhumation depth of the sample. Sublimation is the direct transition of a material from the solid to the gas phase, without passing through the liquid phase. This is done to enhance image quality, because small-scale cuts and pores disappear during sublimation. The thick section was now scanned by LASM (Figure 2.3b).

After a successful scan, further sample preparation was needed to obtain information about fabric and c-axis orientations. The thick section was carefully taken off the glass plate and glued onto a clean plate using a template. The sample was carefully aligned with the already polished ice surface facing the glass. The band saw was used to cut off the main part of the sample, which was packed away and stored for further measurements. The remaining sample was again glued onto the stage of the microtome and the second phase of polishing was started. Four drops of water, applied on every corner, made it possible to measure the thickness of the thin section without touching it. The section was carefully microtomed until the optimal thickness of 300 $\mu$m was reached, the final 100 $\mu$m were polished in small steps of 1–5 $\mu$m. The thin section was set aside for sublimation and after one to four hours measured by an automated FA (Figure 2.3a).

Working for months in the field, often for several hours at temperatures of $-15$–$-20^{\circ}$, increases the possibility for mistakes to occur. The preparation of thin sections might be affected by this, and common problems are e.g. scratching of ice while microtoming or leaving lints from gloves on thin sections. Precautions have been taken to avoid these things from happening, but of course, they cannot be ruled out completely. In total, the quality of the produced thin sections was *good* to *very good* and a large data set was be derived from the measurements.

## 2.3 C-axes measurements with an automated Fabric Analyser

Polarised light microscopy is used to measure the orientation of the c-axis, making use of the birefringence of polarised light in optical anisotropic media. This method only allows to measure one part of the full crystal orientation. The orientation of a-axes is only determinable with different methods like *X-ray Laue Diffraction* or *Electron Backscatter Diffraction* (EBSD). This loss of information is compensated by advantages like good applicability in the field. Another major advantage is the possibility to have automated measurements, which enable the gathering of large amounts of unbiased data and therefore, more reliable statistical analyses.


FIGURE 2.1: **Microtome for preparation of samples**

Microtome for removing thin layers of ice to derive the desired sample thickness and a polished surface.

### 2.3.1 Basics of birefringence

The majority of my results is based on data derived by polarised-light microscopy and the principles are explained in this section. This technique is used because it enables the possibility to take a unique look into the internal structure of crystals and to determine the optical crystallographic properties of the crystals.

Birefringence is a fundamental optical crystallographic property and is defined as the difference between the lowest and the highest refractive indices for anisotropic crystals, which has an impact on the refraction of light through a crystal. Birefringence can be calculated, or estimated by using the Michel-Levy chart (Petrenko and Whitworth, 1999).

For uniaxial anisotropy, the z-direction is the optical axis of the crystal. When light travels through an uniaxial crystal, it gets polarised at a random angle to the optical axis and disperses into the following two components:

- ordinary component, where the electric field E oscillates perpendicular to the optical axis and the refraction index

$$n_o = \sqrt{1 + X_{zz}}$$

- extraordinary component, where the electric field E oscillates parallel to the optical axis and the refraction index

$$n_e = \sqrt{1 + X_{xx}}$$

If the extraordinary ray is faster than the ordinary ray ($n_e > n_o$), a material is called positive. Ice is uniaxial positive due to its hexagonal lattice structure and its

c-axis represents the optical axis.

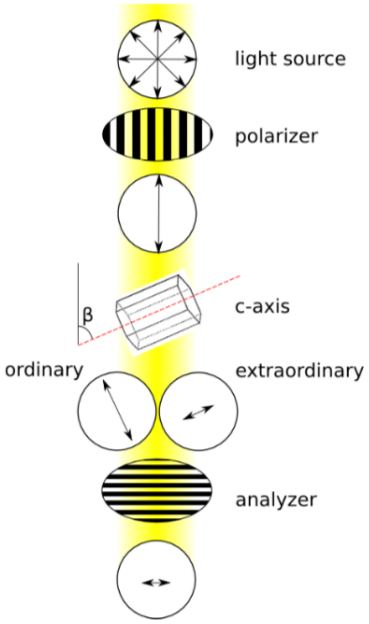


FIGURE 2.2: **Principle of the Fabric Analyser**

Linearly polarised light decomposes in the crystal into the extraordinary and the ordinary wave. These waves pass through an analyser, both components interfere and the resulting intensity is measured. Figure from Eichler (2013).

### 2.3.2 Polarised-light microscopy

The typical set-up consists of two polarisation filters: the analyser and the polariser. Both filters are situated parallel to each other in the x-y-plane and polarisation directions are perpendicular to each other. A light source below the crossed polaroids, expands monochromatic light in z-direction, which passes through the analyser and the polariser. The monochromatic light is absorbed by a *charge-coupled device* (CCD) camera and its intensity is measured. A thin section of ice, with a thickness of d, is put between the polaroids. To represent the c-axis, a unit vector in spherical coordinates is used:

$$c = \begin{pmatrix} \sin\,\theta\,\cos\,\varphi \\ \sin\,\theta\,\sin\,\varphi \\ \cos\,\theta \end{pmatrix}$$

The orientation of the vector is given by the azimuth $\varphi$ and the inclination $\theta$. Inside the crystal, linearly polarised light with an intensity of $A_p$ splits into the extraordinary and the ordinary component, each with a different amplitude. Refraction indices of both components differ, resulting in a phase difference between both waves.

Only the components parallel to the direction of polarisation of the analyser are able to pass at the second polarisation filter (i.e. 90° angle to the first polariser).

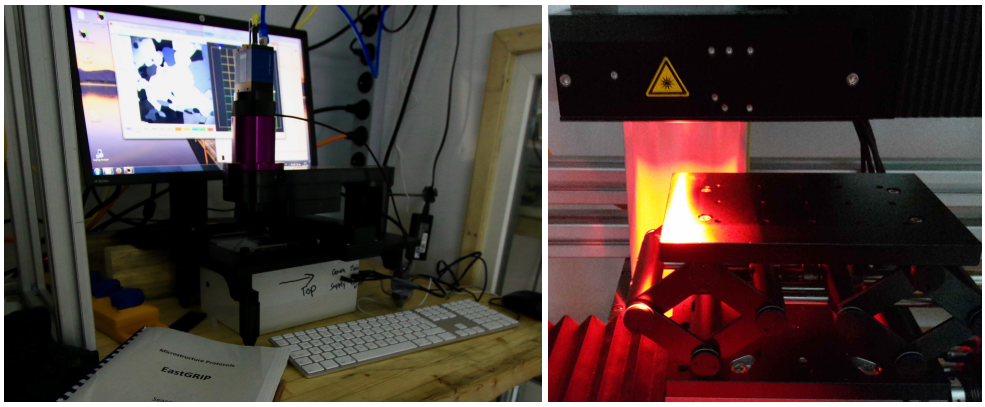

(A) (B)

FIGURE 2.3: **Fabric Analyser and Large Area Scanning Macroscope**

(A) The device and a defined measuring grid are presented. (B) The main stage of LASM, samples are placed here. Picture by J. Kerch.

The ordinary and the extraordinary beam interfere after passing trough the analyser, and the resulting intensity can be calculated. Different view angles are needed to determine the inclination $\theta$. Therefore, the light source position, the camera and/or the orientation of the sample can be changed. By rotating the coordinate system around the z- and x-axis, as well as applying the same transformation on the c-axis vector, four possible solutions for $\theta$ can be derived. If the coordinate system is rotated differently for another time, four more candidates for $\theta$ are produced. This amounts to eight possibilities of $\theta$, two of them being of the same value. This value is the true angle of inclination of the measured c-axis, while the true azimuth is the corresponding extinction angle.

### 2.3.3 Measuring C-axis with the automated Fabric Analyser G50

Measurements of 797 thin sections were all done with the AWI fabric analyser G50, developed by Russel-Head Instruments and described by Wilson et al. (2003). It is the fifth series of automated devices for c-axis measurements with a light source consisting of nine LEDs. Eight are inclined and one is vertical, all are arranged in a circle around the vertical axis. As shown in Figure 2.3a, a motor rotates the crossed polarisers from 0° to 90° in eight steps, and the transmitted light is recorded by a CCD camera. This camera is located above an objective lens and its field of view is a 10 x 10 mm square, resulting in a maximal resolution of 5 $\mu$m/pixel. The thin section is placed on an x-y-motorised stage, which moves according to a previously defined grid. This results in several fabric records of 10 x 10 mm, allowing the recomposition of the entire sample from its individual records. Maximum sample dimensions are 100 x 100 mm and the ideal thickness is 300 $\mu$m. Measurement times depends on the size of the selected grid and the chosen resolution (5–50 $\mu$m). Typical measurements of thin sections with a size of 70 x 10 mm, and a resolution of 20 $\mu$m take approximately 45 minutes.

Several precautionary measures were taken to avoid damaging, or changing the properties of the fabricated thin sections. Touching the sample was kept to a minimum, and only with latex gloves worn above normal gloves. Furthermore, scarfs were used to avoid breathing on the sample while working. Microtome blades were exchanged as soon as scratches appeared on the thin section, or scratching noises were registered. Polished samples were stored away for sublimation and thus, the interaction with the surrounding air was limited. While taking images with LASM and measuring fabric with FA, extensive movement was avoided to not disturb the measurements.

## 2.4 Output and Data

### 2.4.1 Primary Processing

The FA output is a binary file, which contains a raster of given resolution, where each data point displays the following data:

- Retardation quality
$$0 \leq rq \leq 100;$$
- Geometrical quality
$$0 \leq gq \leq 100;$$
- Azimuth angle of the c-axis vector
$$0^\circ \leq \varphi < 360^\circ;$$
- Inclination from the vertical axis
$$0^\circ \leq \theta < 90^\circ.$$

$gq$ and $rq$ estimate the confidence of the measured orientations; $\varphi$ and $\theta$ are the spherical coordinates of the c-axis vector. Besides this raw data, several image files are created, which are used to get a qualitative overview about the fabric and grain properties. For further processing, the data is manually checked and corrected for errors on the sample, e.g. cracks or drops of artificial ice on the surface of the sample. Before automated processing was started, manual image editing is done with *GIMP* for each sample. Negatively affected areas are cut off by producing background-images, indicating the area which is supposed to be analysed.

This pre-processing is followed by automated processing with *cAxes* (Figure 2.4), a programme developed at AWI and described by Eichler (2013).

It automatically detects grains, their c-axis orientations and grain boundaries. Data derived by *cAxes* delivers information about c-axis distribution, grain size, misorientation between adjacent grains and several more parameters. The analysis of

parameters other than grain size and c-axis distribution lies beyond the scope of this thesis. *cAxes* enables a much faster and more precise data acquisition and therefore a better statistical analysis. More information on *cAxes* can be found in Eichler (2013).

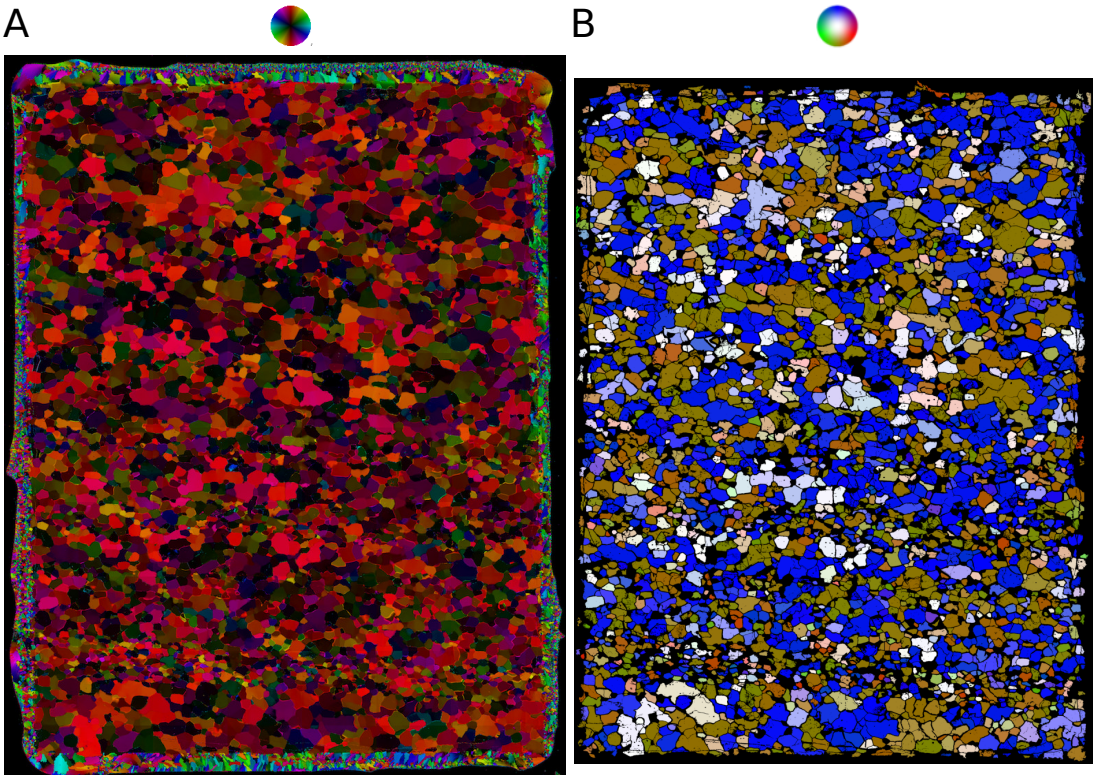


FIGURE 2.4: **Measured fabric image and processed *cAxes* image**

Sample from a depth of 1565,3 m. A) Original fabric image derived by the G50 Fabric Analyser. B) Image after processing with *cAxes*. The surrounding artificial ice, from glueing the sample to the plate, was digitally removed and the grain properties were measured. Colour wheels differ, colours represent the orientation of the c-axis.

### 2.4.2 Fabric statistics

An established method to analyse the shape of fabrics, is to perform eigenvalue calculations for each fabric diagram. Therefore, each measured c-axis orientation is converted into cartesian coordinates and the orientation tensor is determined by standard structural geology methods as stated by Wallbrecher (1986). The distribution of the c-axes is displayed as an ellipsoid, in which the eigenvectors (V1, V2 and V3) of the orientation tensor are representations of the three orthogonal unit vectors along the axes of this ellipsoid. The length of these axes is represented by the eigenvalues. Each eigenvalue is normalised, resulting in the normalised eigenvalues $\lambda_1, \lambda_2 and \lambda_3$, which obey the following conditions:

$$\lambda_1 + \lambda_2 + \lambda_3 = 1 \qquad \text{and} \qquad \lambda_1 \leq \lambda_2 \leq \lambda_3.$$

Eigenvalues are compared to obtain information about fabric shape, e.g.

- random fabric: $\lambda_1 \approx \lambda_2 \approx \lambda_3$, shape of a sphere;
- single maximum: $0 \leq \lambda_1 \approx \lambda_2 \leq \frac{1}{6}$ and $\frac{2}{3} \leq \lambda_3 \leq 1$, shape of a prolate ellipsoid;
- girdle fabric: $\lambda_1 < \lambda_2 = \lambda_3$, shape of oblate ellipsoid.

The strain shape of the finite strain ellipsoid can be calculated as follows:

$$k = \frac{\ln(\lambda_1/\lambda_2)}{\ln(\lambda_2/\lambda_3)}.$$

To distinguish between unimodal and girdle fabrics, Woodcock (1977) established the use of normalised eigenvalues to calculate the woodcock parameter q:

$$q = \frac{\ln(\lambda_3/\lambda_2)}{\ln(\lambda_2/\lambda_1)}.$$

The calculated value of the Woodcock parameter enables a classification between unimodal and girdle fabrics:

- unimodal fabric: $q \leq 1 \rightarrow \infty$;
- girdle fabric: $0 \leq q \leq 1$.

### 2.4.3 Secondary processing and data analysis

Data derived by *cAxes* was statistically analysed with *R* (R Core Team, 2014). Several statistical parameters were calculated on different scales, ranging from single grains of one measurement to all measurements from one bag (55 cm). For reasons of clarity and comprehensibility, only results for entire thin sections (9 cm) are displayed and discussed.

Equal area stereo plots have been created on the basis of c-axis distribution data derived by *cAxes*. This data was further used to calculate contours with statistical significance of point concentrations on equal area stereograms, using the fundamentals explained by Kamb (1959).

For 47 samples, the three eigenvectors were calculated and analysed. The chosen samples were taken from representative depths at intervals of 50-100 metres, results were plotted with the programme *Orient*.

Further grain parameter analysis was done by digital-image analysis using *Image-Pro* by Media Cybernetics. A High-pass filter was applied on previously produced grain boundary data from 720 vertical samples to further analyse grain shape parameters. Analyses of perimeter ratio, roundness and several more parameters were conducted, but only perimeter ratio and roundness are presented in this thesis.

The perimeter ratio $P_t$ reports the ratio of the convex perimeter ($p_c$), to the perimeter of the outline ($p$) of each object:

$$P_t = \frac{p_c}{p}.$$

Following Weikusat et al. (2009b), $P_t$ was used as a measure for grain morphology and grain irregularity; $P_t$=1 indicates perfectly regular grains and $P_t$<1 indicates more irregular grains (Figure 2.5). The roundness $R$ reports the roundness of each object, perfectly circular objects have a roundness of R=1, oblong objects have a roundness of R>1. It is determined in the following way:

$$R = \frac{p^2}{4 * \pi * a}$$

with $p$ = perimeter and $a$ = area.

## 2.5 Microstructure images derived by LASM

After successful sublimation, the thick section is placed beneath a *Large Area Scanning Macroscope* (LASM) by Schäfter+Kirchhoff. This device replaces the time-consuming ice core analysis technique of using an optical microscope and a CCD area scan camera. LASM consists of a line scan camera with 8192 pixels and a Gigabit Ethernet interface, an illumination unit and a high resolution lens as displayed in Figure 2.3b. The sample is imaged with a resolution of 5 $\mu$m. The scan speed is up to 36 mm/s, the maximum measuring width is 41 mm and the maximum measuring length is unlimited. The measured samples exceed widths of 41 mm and therefore require two scans, resulting in total measurement times of two to five minutes.

Bright-field illumination is used to capture the microstructure, the basic principle is displayed in Figure 2.6. Surfaces parallel to the sensor reflect directed light from the illumination unit. Light reflected from edges and structured areas is reflected away from the sensor and hence, appears dark. Therefore, gas inclusions appear as dark spots or bubbles and grain boundaries as dark lines (Figure A.11). To obtain high resolution 2D images of the microstructure, the right focus is applied and the object is moved with a defined velocity against the sensor. The complete image is formed by combining all individual line signals (Krischke et al., 2015). For further information on the use and technique of LASM, it is referred to Krischke et al. (2015).

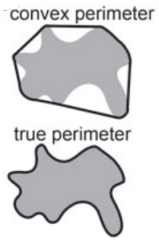


FIGURE 2.5: **Perimeter Ratio**

Perimeter ratio as a measure of grain irregularity, displaying the ratio between the convex and true perimeters (Weikusat et al., 2009b).

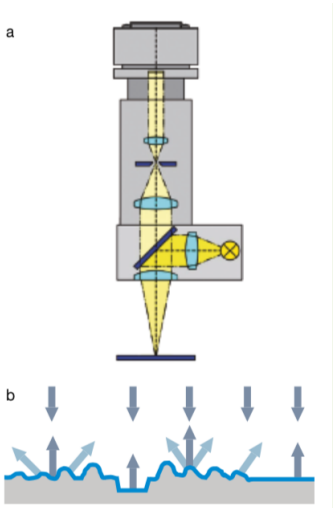


FIGURE 2.6: **Schematic principle of LASM**

(a) Light from the illumination unit is directed towards the sample and reflected signals are captured. (b) The roughness of the surface of the sample controls the amount and direction of reflected light. Surfaces parallel to the sensor reflect the light; structured areas and edges reflect the light away from the sensor, these areas therefore appear dark (Krischke et al., 2015).

## 2.6 Analysis of high-resolution images derived by LASM

High-resolution images derived by LASM were manually analysed regarding unusual features and hints for dynamic recrystallisation, such as grain bulging or island grains. A classification introduced by Weikusat et al. (2009b), was used to distinguish between subgrain-boundary types. For 100 samples, chosen from regular intervals throughout the core, subgrain-boundaries were investigated and classified as one of the three following types:

1. *N* type: Normal to the basal plane. This type displays the classic perception of a grain undergoing polyganisation.

2. *P* type: Parallel to the basal plane and only crosses parts of the grain. Swarms of subgrain-boundaries of this type were regularly observed, being parallel to each other.

3. *Z* type: Irregular, step-like or zig-zag shape. This type is normally rather short and appears in networks, hardly ever crossing the entire grain and becoming weaker towards the centre of the grain.

If it was not possible to classify subgrain-boundaries with confidence (e.g. due to bad sample quality or insufficient sublimation time), they were not classified at all.

A quantitative processing of LASM data is possible, but very time-consuming and would have gone beyond the constraints of this thesis.

# 3 Results

## 3.1 Crystal preferred orientation

### 3.1.1 Eigenvalues

Hereafter, results of calculated eigenvalues are presented, based on measured c-axis distributions of 797 EGRIP samples and displayed in Figure 3.1. Mean eigenvalues calculated over the entire core amount to $\lambda_1$=0.060±0.069, $\lambda_2$=0.354±0.043 and $\lambda_3$=0.585±0.079. The overall development of the three eigenvalues shows the following patterns. $\lambda_1$ decreases constantly until 500 m of depth and stays at very low values henceforth. $\lambda_2$ starts around 0.25, $\lambda_3$ at 0.5 and both eigenvalues intersect around 0.4 at a depth of 250 m. $\lambda_2$ oscillates around 0.35 until a depth of 900m, and stays around 0.4 until 1360 m, followed by a slight decrease. $\lambda_3$ behaves antiparallel to $\lambda_2$ and oscillates around 0.65 until 900 m, is rather constant at 0.6 until 1200 m, and increases slightly towards 1714 m.

The first measurements, starting at a depth of 111 m, reveal similar values for the smallest eigenvalue ($\lambda_1$=0.21) and the intermediate eigenvalue ($\lambda_2$=0.25). With depth, $\lambda_1$ decreases steadily and from 510 m on, $\lambda_1$ hardly changes and plateaus at values of below 0.03 until the final measurement at 1714 m.

$\lambda_2$ increases until a depth of 210 m, where $\lambda_2$ is similar to $\lambda_3$ ($\lambda_2$=0.4, $\lambda_3$= 0.45). Down to a depth of 650 m, $\lambda_2$ remains between 0.28 and 0.42, accompanied by a change in variability. $\lambda_2$ locally peaks at 650 m, then remains rather high and peaks again between 720-730 m. This is followed by a steep decrease of $\lambda_2$ down to a total minimum at 775 m ($\lambda_2$=0.21). Below this depth, $\lambda_2$ develops towards higher values at 850 m and 890 m. After the brittle ice zone gap, $\lambda_2$ increases slightly to roughly 0.4, and varies between values of 0.31 and 0.48 until a depth of 1360 m. The total maximum of 0.48 for $\lambda_2$ is measured in this depth. Below, a decrease of $\lambda_2$ towards 0.3 was observed for the following 140 m, followed by an increase ($\lambda_2$=0.38 at 1500 m). The final 214 m exhibit an oscillating pattern with peaks every 100-115 m (at 1500 m, 1615 m and 1714 m).

The largest eigenvalue $\lambda_3$ is about 0.55 at 111 m of depth, and decreases towards a depth of 200 m. In this depth, $\lambda_3$=0.45, a slightly larger value than observed for $\lambda_2$. Below, $\lambda_3$ increases parallel to the decrease of $\lambda_1$ and $\lambda_2$. At 450 m, $\lambda_3$ begins to plateau in a range of 0.55 and 0.68, showing an antiparallel evolution to $\lambda_2$. Local minima are measured in depths of 550 m, 650 m, 723 m and 900 m. The total maximum of $\lambda_3$ was observed at the depth of 760 m, the depth of the total minimum of $\lambda_2$. $\lambda_3$ is slightly lower, below the brittle ice zone gap, oscillating around 0.55 and

0.6 down to 1250 m. A slight increase was measured for the next 150 m, where $\lambda_3$ reaches values of about 0.66-0.72. A local minimum was measured in 1360 m, the total maximum of the intermediate eigenvalue ($\lambda_2$=0.48). Similar to $\lambda_2$, the last 214 m are characterised by a zig-zagging development, with $\lambda_3$ peaks parallel to $\lambda_2$ troughs and $\lambda_3$ troughs parallel to $\lambda_2$ peaks.

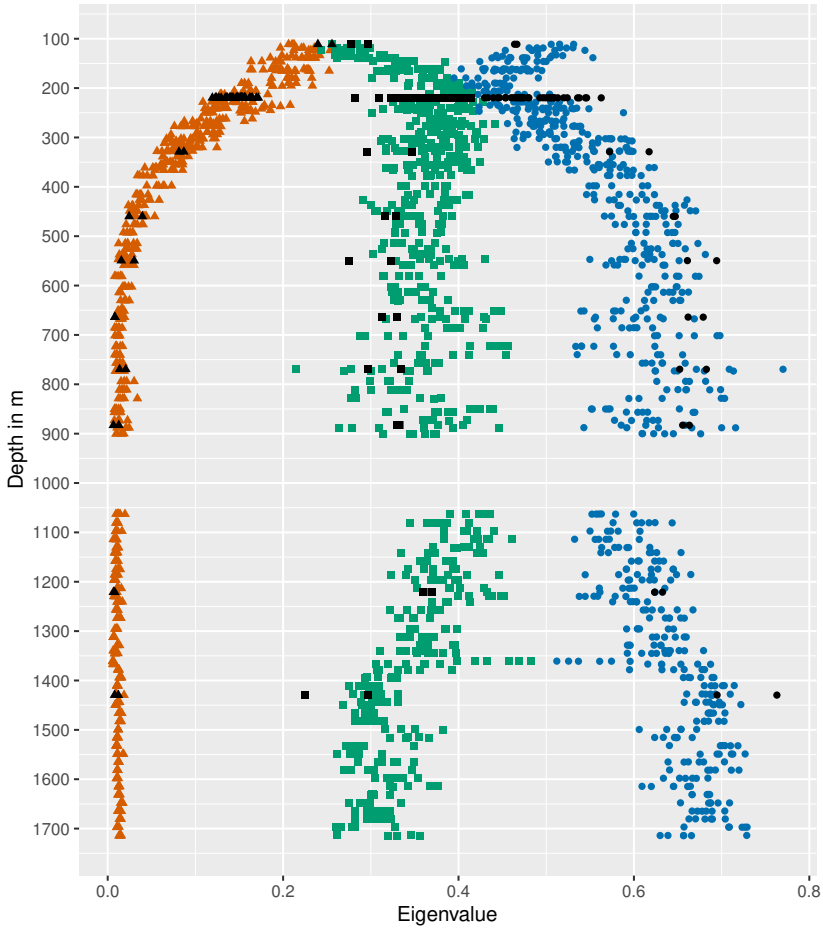


FIGURE 3.1: **Eigenvalues of EGRIP ice core**

Filled red triangles represent $\lambda_1$, filled green squares $\lambda_2$ and solid blue circles $\lambda_3$. Horizontal samples are indicated in black.

### 3.1.2 Detailed view of wavy pattern

A wavy pattern in the eigenvalue development was observed and is displayed in Figure 3.2a and 3.2b. Below 510 m, $\lambda_1$ does not exceed 0.03 and changes only slightly with depth (Figure 3.2a). This is the onset of the development of a wavy pattern, in the form of an antiparallel co-evolution of $\lambda_2$ and $\lambda_3$ with depth. Between 550 and 850 m, the wavelength varies slightly between 80 and 120 m. Between 1060–1360 m, a steadier wavelength of 120 m was observed, interrupted by one measurement at 1180 m as displayed in Figure 3.2b. Between 1360 and 1500 m the wavelength increases to 140 m, and drops to 110–120 m for the last 314 m.


(A) Eigenvalues between 550-850 m (B) Eigenvalues between 1050-1714 m

FIGURE 3.2: **Wavy pattern at 550-850 m and 1050-1714 m**

(A) Eigenvalues show a wavy pattern with a wavelength between 75 and 100 m. (B) Below 1050 m, the wavelength varies stronger and switches from 115 to 140 m. The same annotation as in Figure 3.1 is used.

### 3.1.3 Stereographic projections

Fabric diagrams from all 797 measured thin sections were analysed and an overview is presented in Figure 3.3. All derived stereoplots can be found in Appendix B and a summary is presented in Table 3.1. In total, a development from a broad single maximum CPO towards a crossed girdle CPO was observed in the upper 300 m. This CPO develops into a vertical girdle until 500 m, which develops in strength until a horizontal maxima CPO was observed around 1230 m. This pattern varies in strength until 1714 m.

The c-axis distribution is presented as viewed from above, along the axis of the core. Thus, a vertical c-axis is represented by a point in the centre of the diagram and a horizontal c-axis by a point close to the edge. Data about the azimuth orientation is not available yet, and the true horizontal orientation of the diagram is therefore not reconstructable at the time of this study.

TABLE 3.1: **Observed CPO patterns at EGRIP**

| Depth [m] | Crystal Preferred Orientation |
|---|---|
| 110-196 | Single Maximum |
| 196-294 | Crossed Girdle |
| 295-500 | Crossed Girdle-Girdle Transition |
| 500-1230 | Vertical Girdle |
| 1230-1394 | Vertical Girdle-Horizontal Maxima Transition |
| 1394-1714 | Horizontal Maxima |

Between 110 m and 196 m the samples display a broad single maximum CPO

with a large variety in grain numbers (403-1500) and c-axes orientations. The majority of the c-axes is loosely orientated around the centre of the diagram and only a few axes are located close to the horizontal axis. The amount of horizontally orientated crystals decreases slowly with depth and a crossed-girdle CPO begins to develop at 196 m (Figure 3.3).

Two types of crossed-girdle are observed, which can be named Type I and Type II in analogy to quartz, plus several intermediate transition-types. Overall, type I dominates and is characterised by a girdle connecting both crosses, which is observed regularly. Furthermore, the majority of samples shows one stronger developed leg, varying in extent and distinctness. The strength of this CPO-pattern varies from sample to sample, almost disappearing completely for a few times (e.g. 250 m) and is especially distinct in samples with a small amount of grains (e.g. 240 m). The general trend is a strengthening of the pattern with depth and a peak strength around 289 m. The last distinctive crossed-girdle is observed at a depth of 294 m, setting the onset for a CPO transition into a developing girdle CPO.

With depth, a broad girdle CPO gets more distinct and becomes more manifest. The transition zone between the crossed-girdle CPO and the broad girdle CPO takes place at a depth between 294 and 376 m. A clear broad girdle CPO is observed between 376 and 492 m. From this depth on, the occurring CPOs are classified as fully developed girdle CPOs. The transition to a strong girdle CPO is completed at a depth of 1113 m and this CPO pattern can be seen until 1230 m. In this depth, a CPO with (sub-) horizontal maxima is observed for the first time, varying largely in strength from sample to sample. This transition zone towards a distinct horizontal maxima CPO occurs until 1394 m. This CPO is observed until the final sample at 1714 m.

Classifications of CPO might vary, depending on the used plotting method. Classic schmidt plots enable a good overview, but contour plots are more detailed, hence more usable, for the clear distinction between CPO patterns. My partitioning of the core, regarding CPO, was done on the basis of contour plots. This classification is rather subjective, but is not an issue for this thesis because classification and interpretation were only done by myself.

### 3.1.4 Eigenvector evolution

In the shallowest part of the core, V1 and V2 are horizontally orientated (~5°) and V3=~90° (Figure 3.4). With increasing depth, V3 rotates towards the horizontal and ranges from 0 to 14°, while V2 is vertically orientated.

At the top of the core, the largest eigenvector V3 is vertically aligned (80–90°) and hence equals the vertical axis of the ice core (Figure 3.5). The smallest and the intermediate eigenvector are located in the horizontal axes of the plane. At various depths, V3 rotates a couple degrees away from the vertical axis but always returns to its prior position (e.g. 195.43 m, 205.79 m). At a depth of 212 m, all three eigenvectors experience a major change in position and V3 is orientated towards the horizontal

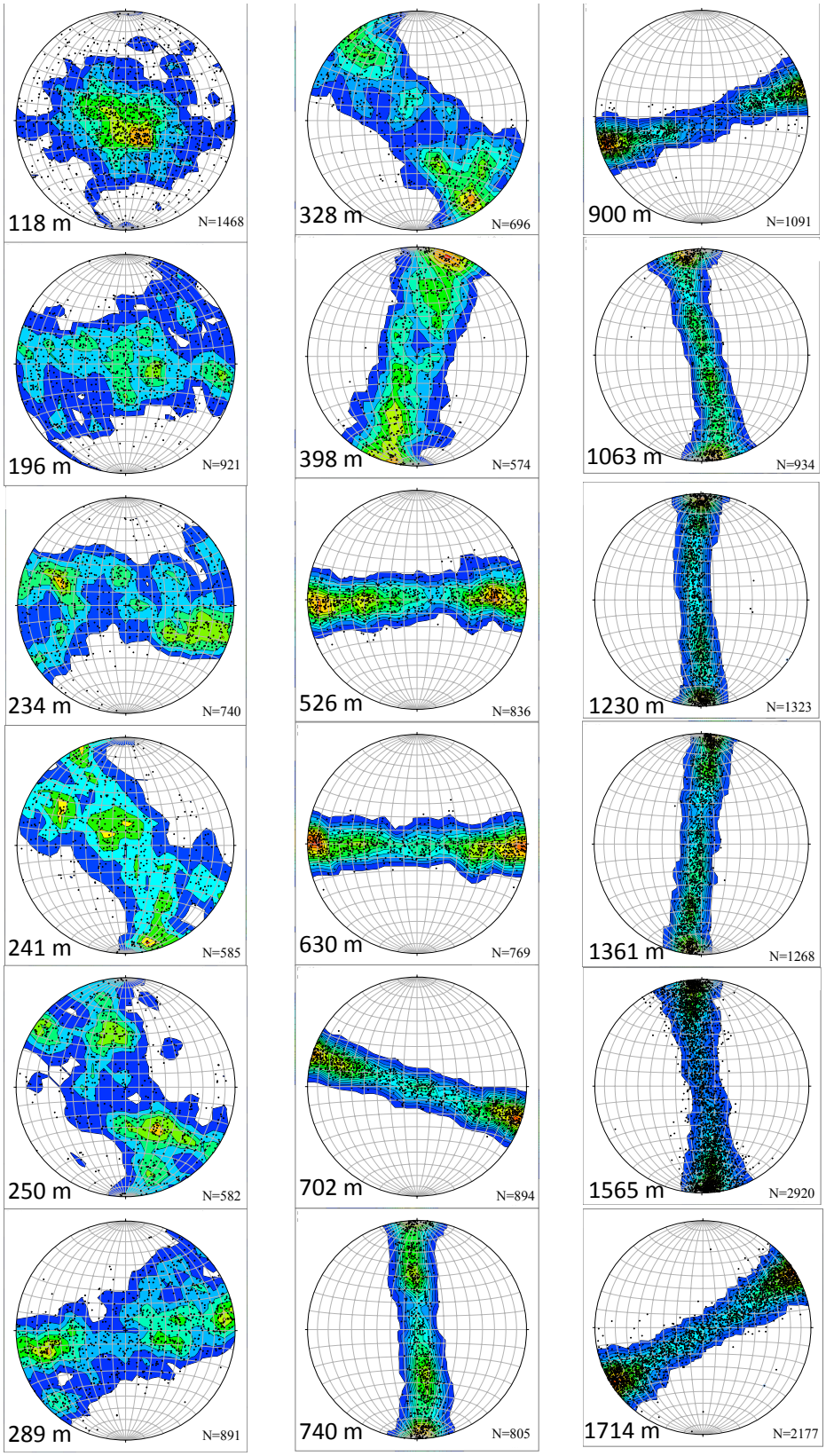


FIGURE 3.3: **CPO patterns throughout the EGRIP ice-core**

Displayed are c-axis distributions as Kamb contours following Kamb (1972) with contour intervals=2.0x$\sigma$. The main CPOs of the ice core are visible, a detailed description is done in Chapter 3.1.3. The depth of the analysed sample and the number of grains in it are indicated for each sample. All samples are presented in an equal area lower hemisphere projection.

for the first time, while V2 is vertically orientated. All eigenvectors rotate in various ways from sample to sample until a hard shift in plunge occurs between 220 and 290 m. At this depth region, V3 varies between 1.4 and 87.9°. At 300 m, V3 rotated completely away from the vertical towards the horizontal and only shows a plunge of 0.1-12° until 900 m. One outlier was observed at 723 m where V3 shifted towards the sub-vertical with a plunge of 73.4°. The final 650 m are characterised by a horizontal V3 with a plunge in a range of 0.7-6.7°.

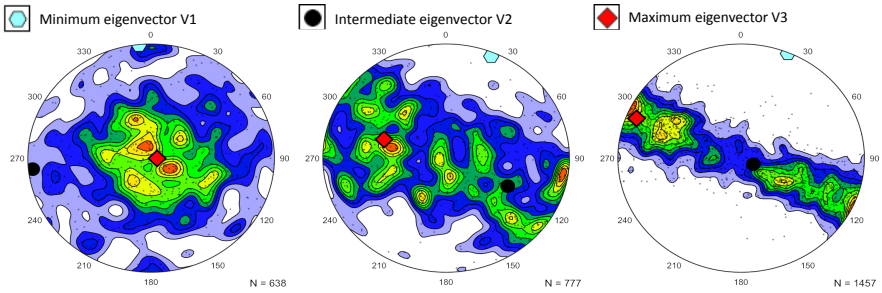


FIGURE 3.4: **Eigenvectors at a depth of 118, 228 and 361 m**

Tilting of eigenvectors with depth. The eigenvector configuration present at 361 m has been observed throughout the rest of the core.

### 3.1.5 Woodcock parameter

The mean Woodcock parameter for all samples is 0.384±1.48. The total range is between 0.013 and 37.415 with a clear trend towards lower values with increasing depth as displayed in Figure 3.6. The upper 100 metres show the largest variability and range from 1.018 (133.3 m) to 37.415 (135.3 m), representing a large spatial variability and major changes of this parameter over only a few metres. A general decrease is observed from the first measurement onwards and below a depth of 179.6 m, measured Woodcock parameters do not exceed 1.0. The values decrease even further and the Woodcock parameter is not observed to be higher than 0.5 below 306.9 m. The large variability, in a range of 0.02-0.49, decreases with depth. At 500 m, most samples show Woodcock parameters between 0.15 and 0.28. Values keep decreasing towards 700 m, followed by a general increase in absolute values and Woodcock parameter-variability. Furthermore, a few unusual high values are observed at 760 m (0.49) and 900 m (0.39). Samples at 1050 m exhibit smaller Woodcock parameters, clustering around 0.1. From this depth on, the Woodcock parameter increases constantly and final values are between 0.18 and 0.33. Samples from a depth of 1360 m show the lowest values of the entire core (0.013).

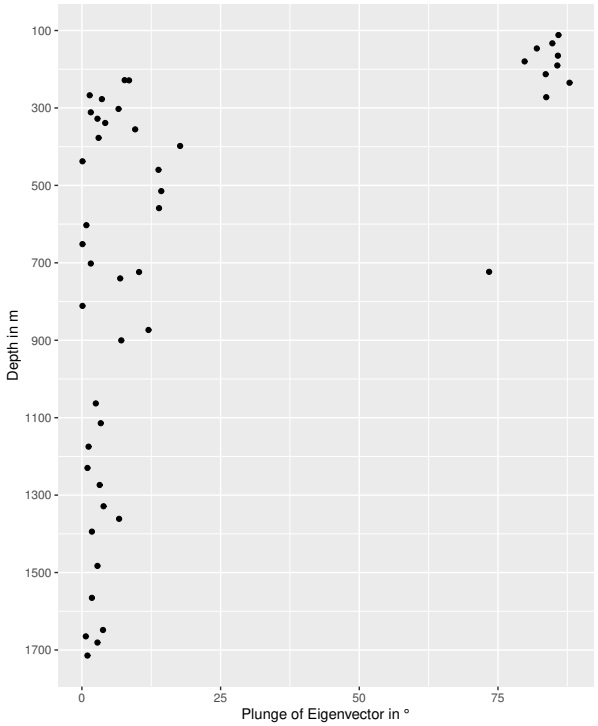


FIGURE 3.5: **Development of the largest eigenvector V3 with depth**

## 3.2 Grain properties and texture

### 3.2.1 Grain size

The mean grain area of the entire core is 4.79±2.33 $mm^2$. Mean grain size values are in the range of 0.85-12.19 $mm^2$ with the largest scatter in the upper part of the core between 300 and 700 m and very low values between 1400 and 1714 m (Figure 3.7).

The first measurements at 111 m show a grain size close to 3 $mm^2$, followed by a steep increase towards maximum values at a depth of 450-550 m. The upper 150 m are also characterised by a small variability in grain size (~1-2 $mm^2$), which increases parallel to the gain in absolute grain size of up to 7-8 $mm^2$. This broad peak is followed by a decline in grain size, accompanied by a slight decrease in the general grain size variability excluding some outliers at 760 and 895 m. After the brittle-zone gap, our results show a strong change in grain size evolution with depth. Between 1050-1140 m, grain size ranges from 4.0 to 6.8 $mm^2$. The following 160 m show a rapid decline in grain size and grain size variability, excluding samples from a depth of 1186 m, and measured values hardly differ from each other. Two local maxima are observed in depths of 1312 and 1360 m, representing a 130 m long part of the core with larger grain sizes compared to neighbouring measurements. Between 1400 and 1540 m, grain size is relatively stable and fluctuates around 1.7 $mm^2$. The final 174 m show a small-scale zig-zag pattern in grain size evolution with absolute values between 0.8 and 2.7 $mm^2$. Especially for the last 350 m of the core, it is observed that samples from the same bag are highly similar in grain size with variations hardly

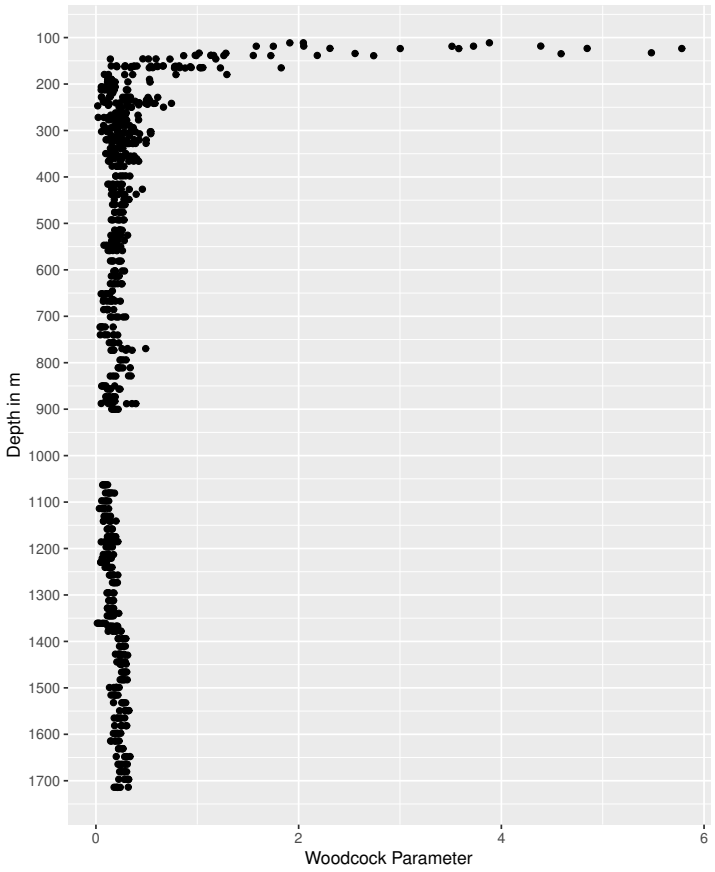


FIGURE 3.6: **Woodcock parameter with depth**

Displayed are mean values for each measured thin section. The largest Woodcock parameter of 37.415 at 135.3 m is not displayed.

exceeding 0.1 $mm^2$ between neighbouring samples.

### 3.2.2 Perimeter ratio

The perimeter ratio was calculated for each grain of each sample, but for reasons of comparability and visibility, mean values for thin sections have been used and are displayed in Figure 3.8.

The measured perimeter ratios have a high variability and range from 0.46 to 0.90 with a mean standard deviation of 0.15. The total mean perimeter ratio is 0.82. The general perimeter ratio evolution with depth exhibits a C-shape, with high values in the upper and lower part of the core, and small values in the middle part of the core.

Perimeter ratio of the upper 700 m is between 0.72 and 0.91 with a large variability from sample to sample. Only a dozen measurements around 275 m have unusual similar values between 0.83-0.86. The variability in perimeter ratio stays rather constant with increasing depth, but absolute values decrease and bottom out at 0.72 around 750 m of depth. There is one outlier with a perimeter ratio of 0.66 at 740 m, and another one at 723 m, representing the smallest measured value of 0.46

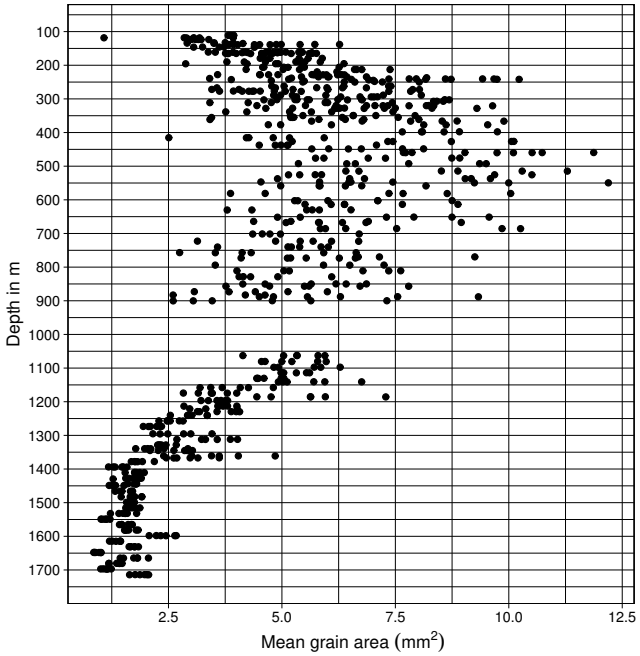


FIGURE 3.7: **Grain size development with depth**

Each dot represents the mean grain size of one analysed thin section.

(Figure A.4). A slight increase in perimeter ratio is observed in the final 180 m before the brittle ice zone gap, with values ranging from 0.73 to 0.83. This trend is also measured from 1060 m downwards to the final measurement at 1714 m. A similar pattern of perimeter ratio variability, compared to the upper part of the core is observed. Variability between samples from similar depths is rather large (~0.1) and exceeds even values of 0.18 a few times (e.g. 1378 and 1482 m). In general, perimeter ratio increases and measurements around 1650 m match values measured in the shallow part of the core at 111 m. The final 60-70 metres show even higher values and are among the highest of the entire core.

### 3.2.3 Roundness

The total mean roundness is 2.98 with an average standard deviation of 0.8. Absolute values (for thin section means) are ranging from 1.93 to 17.64 (Figure 3.8). Between 111 and 300 m, roundness was measured to be mainly between 2.5–3 with some outliers reaching values up to 4.5. The variability at 300 m is comparably small and this depth is the onset of an increase in roundness until a depth of 750 m with a zone of decreasing roundness between 500–630 m. With increasing depth, roundness variability increases and the second highest value of the entire core is measured at 740 m (5.9), dwarfed only by a measurement from 723 m of depth (17.63). A general decrease takes place until 900 m, accompanied by less scattering (roundness between 2.7 and 4.7). This pattern continues with increasing depth and roundness is at the lowest (~2.0) in the deepest part of the core. Parallel to this, variability decreases and measurements from similar depths vary only slightly (~0.5-1) compared to the

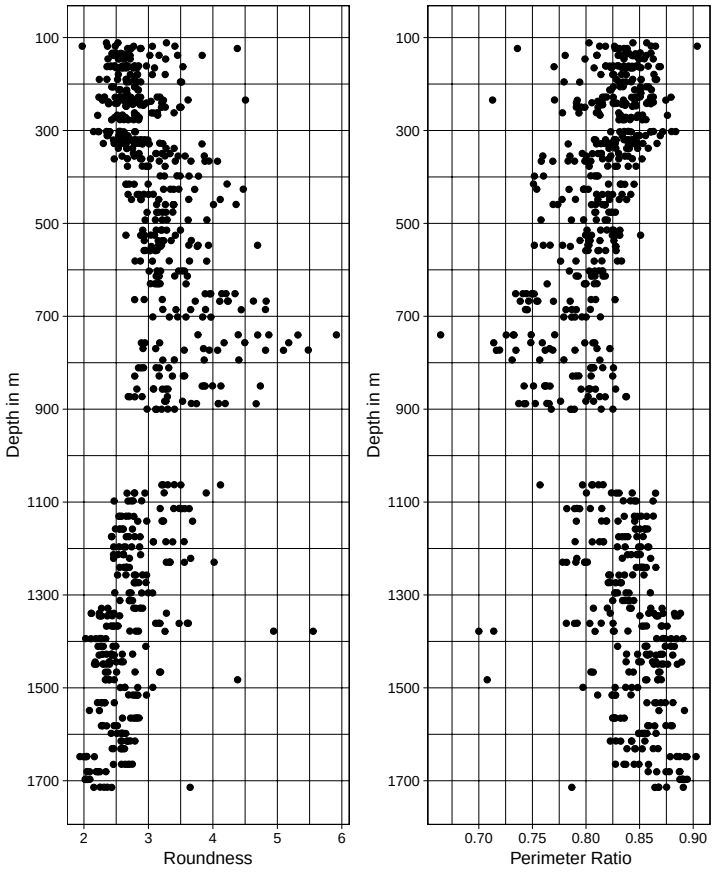


FIGURE 3.8: **Roundness and perimeter ratio**

Values for every sample are presented. Perimeter ratio outliers are not displayed and can be found in Figure A.4.

upper part. Outliers are found at a depth of 1378 m (4.9 and 5.5), 1482 m (4.4) and 1714 m (3.6).

### 3.2.4 Microstructural features in LASM images

For every 100 m of the core, at least five images were manually examined. Areas of high interest were surveyed in a higher resolution and each sample was visually analysed. In total, more than 200 images were manually searched for interesting features regarding hints of deformation history. Emphasis was put on distinct features, such as strong grain size variations, unusual grain shapes and grain- as well as subgrain-boundaries. These observations are objective and are used to support the quantitative results mentioned above, rather than to stand on their own. The following paragraph summarises briefly reoccurring features.

- **Grain clustering**: Several samples contained grains of small grain size, which were clustered around larger grains. Often, these small grains had similar c-axis orientations, while the c-axis of the large grain was orientated differently.

- **Grain shape**: Unusual grain shapes were prominent throughout the entire core and irregular shaped grains were the rule rather the exception (Figure 3.9). Amoeboid grain shapes and extensive protrusions were common as well as sutured grain boundaries.
- **Grain-boundary morphology**: Grain-boundaries are the most visible feature of microstructure in ice. For all analysed samples, they were irregular. Grain protrusion were observed in several samples, accompanied by island grains (Figure 3.9 and 3.10). Dynamic and complex shapes were observed regularly and are quantified, using the perimeter ratio, in Chapter 3.2.2.
- **Subgrain-boundary morphology**: Subgrain-boundaries were regularly observed in all samples and several types can be distinguished. Following the method of Weikusat et al. (2009b), subgrain-boundary shape and arrangement, with respect to the basal plane, was used to classify between the types N, P and Z. Some samples showed connected N- and Z-type subgrain-boundaries, which made a clear distinction difficult. The occurrence of one subgrain-boundary type was frequently accompanied by one or even both other types (3.9).

  100 distinguishable subgrain-boundaries from various depths along the entire core were classified. 51 were N-, 25 Z- and 24 P-type subgrain boundaries. The number of analysed subgrain-boundaries is too low to have statistical importance on its own and should be seen as qualitative support for the other results presented in this thesis. Further examples can be found in the Appendix (Figure A.6-A.23).

## 3.3 Detailed case study at 1360.8–1367.3 m

This depth regime is characterised by a major change regarding $\lambda_2$ and $\lambda_3$. Furthermore, some other parameters display unusual features compared to neighbouring samples below and above. This depth regime was therefore analysed in more detail.

$\lambda_1$ is constantly close to 0, $\lambda_2$ reaches its overall highest value of 0.48 and $\lambda_3$ shows a local minimum of 0.51 at 1360.8 m. $\lambda_2$ decreases slowly over the next decimetres, still remaining comparably high. At a depth of 1366.8 m $\lambda_2$ decreases towards values between 0.32 and 0.37. During this stage, $\lambda_3$ develops antiparallel to $\lambda_2$ and shows unusual low values, which start to increase again until they level out at values about 0.62-0.68 3.2b. In addition, a flip of the maximum eigenvector V3 was observed between 1360.84 and 1361.02 m (Figure 3.11).

Comparable high mean grain sizes were observed in the entire regime, ranging from 2.4 to 4.9 $mm^2$ (Figure 3.7). Measurements only contain between 950 and 1900 grains, less than found above and below. Horizontal layers of small grains are frequently observed to disrupt the relatively large grains, with layer thicknesses ranging from a few millimetres to several centimetres. These developments are accompanied by a change in mean perimeter ratio (Figure A.4). Comparably low values

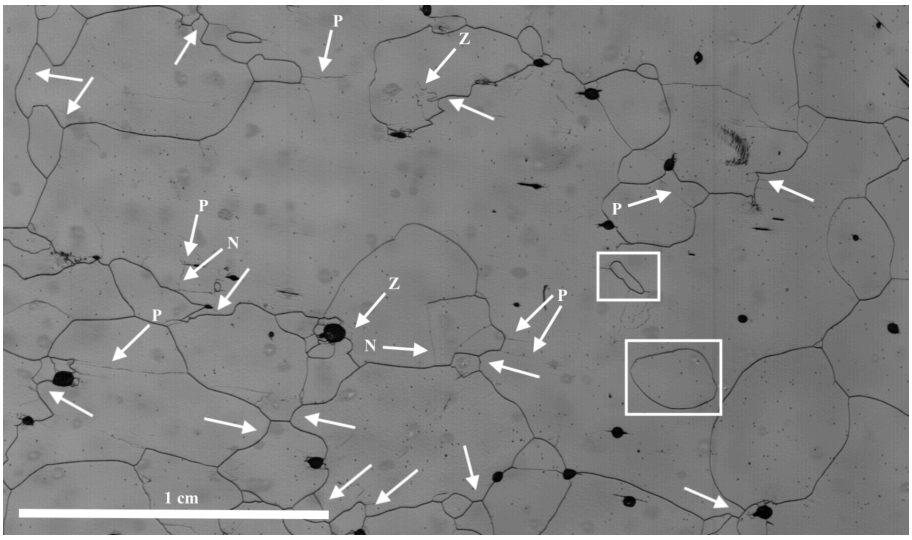


FIGURE 3.9: **High-resolution image from a depth of 426 m.**

Grain protrusions into neighbouring grains are marked by white arrows. White squares indicate island grains, small grains inside larger grains. Subgrain-boundaries are classified following Weikusat et al. (2009b): P = parallel to basal plane, N = normal to basal plane and Z = zig-zag.

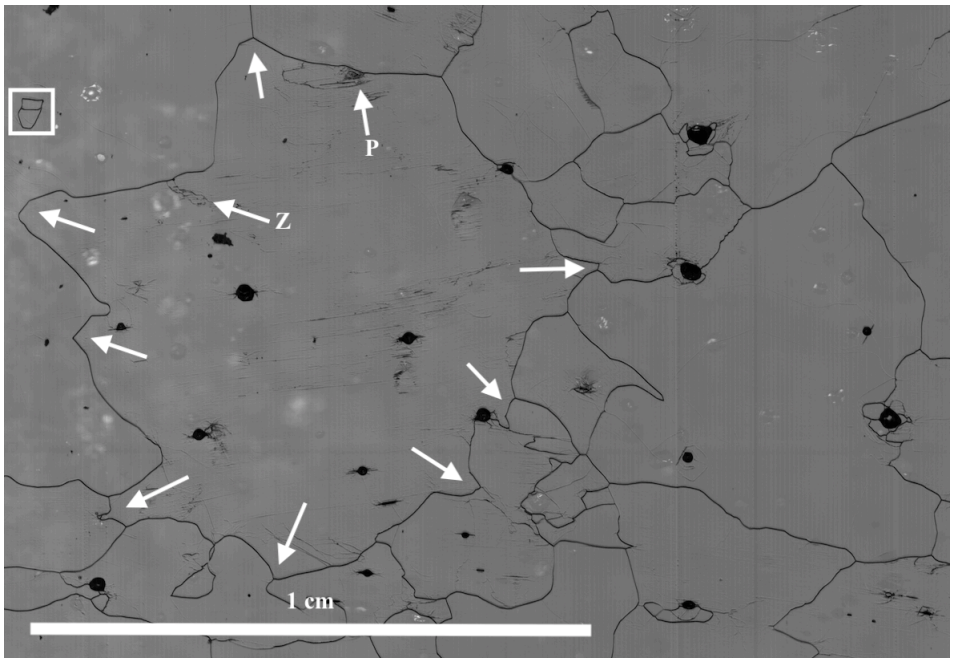


FIGURE 3.10: **High-resolution image from a depth of 723 m.**

Protruding grain boundaries are visible, an island grain was observed in the upper left corner. The same annotation as in Figure 3.9 is used.

dominate between 1360-1361 m (0.78-0.83), followed by an increase of up to 0.88 for measurements between 1366-1367 m.

The general CPO pattern is a vertical girdle, but its strength varies strongly on the cm-scale (Figure 3.12). There is a clear horizontal maximum at 1360.75 m which transitions over the next 55 cm into a rather evenly distributed vertical girdle without a significant horizontal maximum. The next bag starts at 1366.8 m and displays an even stronger girdle. For the following 27 cm, the evenly distributed girdle weakens and the horizontal maximum becomes more distinct. The pattern switches again into an evenly distributed girdle from 1367.07 m towards the end of the bag at 1367.25 m.

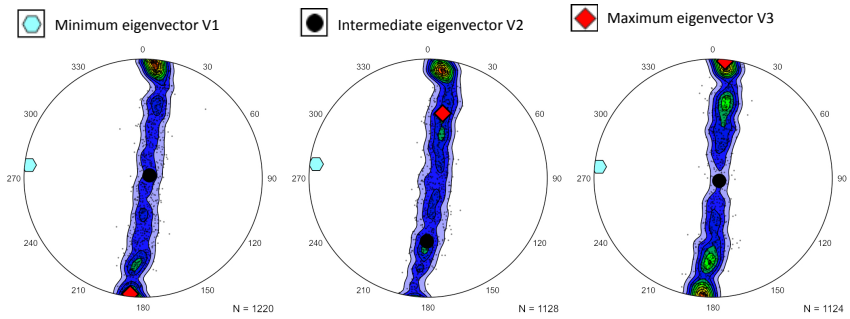


FIGURE 3.11: **Eigenvector development around 1360 m**

From left to right: 1360.84, 1360.93 and 1361.02 m. The change in plunge of V3 at 1360.93 m is clearly visible.

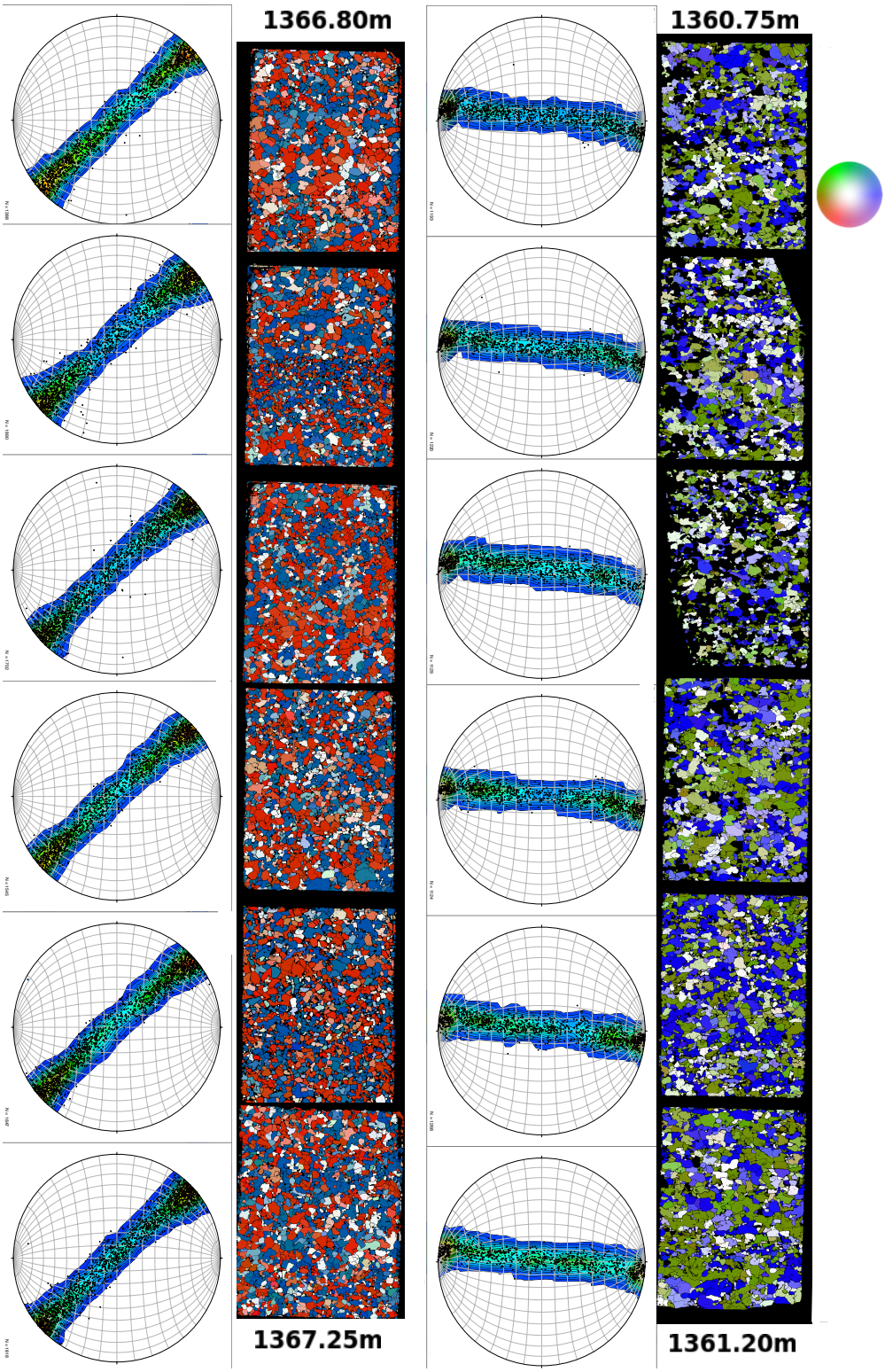


FIGURE 3.12: **Small-scale changes between 1360.75-1367.25m**

Displayed are crystal-preferred orientations and the related fabric, both from thin sections with dimensions of roughly 96 x 70 x 0.3 mm. Colours represent c-axes orientations and are displayed by the colour wheel.

# 4 Discussion

Analysing the physical properties of a deep ice core is a time-consuming process and it takes years to combine results from different approaches. The analysis of microstructure and fabric is already conducted during the drilling process and first results can be derived relatively quickly, allowing a first glimpse into the ice core from a physical perspective. To achieve this was the overall goal of this thesis.

Fabricating thin sections to analyse c-axis distribution and microstructure has been completed for the upper 1714 m of the EGRIP ice core. When interpreting these information, potential errors and uncertainties have to be considered.

## 4.1 Fabric of the EGRIP ice core

The evolution of eigenvalues with depth of the EGRIP ice core is characterised by a fast decrease of $\lambda_1$, reaching values smaller than 0.03 at around 500 m. $\lambda_2$ and $\lambda_3$ show comparable values in the upper hundred meters and encounter almost the same value at around 250 m. From this depth on, anisotropy steadily increases and $\lambda_2$ and $\lambda_3$ separate from each other until a strong anisotropy is reached at 1714 m. Noticeable features are the occurrence of a wavy pattern between 550-850 m and from 1100 m on downwards. At 1360 m, a highly interesting outlier was observed, deviating strongly from neighbouring measurements.

Systematic offsets of the eigenvalues between vertical and horizontal sections can be explained by the ambiguity of measurement of c-axes lying close to the observation plane.

The presented eigenvalues show a rapid evolution of anisotropy with depth, compared to results from other deep ice cores. Figure 4.1 displays the results from this thesis and compares them to measurements from Dronning Maud Land, Antarctica (EDML), and Central and North Greenland (GRIP and NEEM). Contrary to these ice cores, a very prominent feature of EGRIP is the development of the smallest eigenvalue $\lambda_1$ (Figure 4.2). It decreases from the first measurement onwards, and plateaus in roughly 500 m of depth ($\lambda_1 < 0.03$). $\lambda_1$ of EDML and NEEM reach a comparably low value at 1400 m, at a depth almost three times deeper compared to EGRIP (Weikusat et al., 2017; Eichler, 2013; Montagnat et al., 2014). A study by Thorsteinsson et al. (1997) reports a similar low value of $\lambda_1$ in an even deeper depth of 2200 m. Also, the encounter of $\lambda_2$ and $\lambda_3$ at 240 m is another unique feature of the presented EGRIP data. The compared cores show relatively consistent eigenvalue developments with depth and eigenvalues do not intersect. At EGRIP, values of $\lambda_2$

and $\lambda_3$ stay relatively close to each other, throughout the entire analysed depth. Contrary to this pattern, $\lambda_2$ and $\lambda_3$ of GRIP and NEEM display large differences already from the first measurements on. Interestingly, $\lambda_1$ of EDML develops similar to $\lambda_3$ of NEEM, while $\lambda_2$ and $\lambda_3$ are more similar to EGRIP, especially in the regime between 1050 and 1714 m.

The significant differences between the EGRIP core and the compared older cores, can be explained by the more dynamic location of EGRIP. EDML, GRIP and NEEM were drilled on ice divides or domes, to guarantee successful drilling operations and undisturbed climate records. Hence, it was expected to find major differences in the EGRIP core, e.g. indicators for different deformation regimes or deformation-related processes. This goes hand in hand with the observation that deformation and dynamic recrystallisation seem to start in a much shallower depth at EGRIP, resulting in a different eigenvalue development. This interpretation is supported by further microstructure features such as perimeter ratio, roundness and CPO.

The detailed case study around the depth of 1360 m shows a significant difference in eigenvalues compared to measured samples above and below. This is accompanied by a flip of the maximum eigenvector V3 (Figure 3.11), which might indicate a sudden small-scale change in deformation mode. This depth regime is highly interesting and a similar "jump" in eigenvalues was observed at a depth of 2360 m at EDML by Jansen et al. (2017). The authors of this study suggested this depth to be a shadow zone impacted by strain partitioning. A layer hardly affected by simple shear is supposed to be sandwiched between a layer with moderate shear above, and a layer with moderate shear below (Jansen et al., 2017). This hypothesis is supported by a layer of larger grains, probably due to less deformation. The same conditions were also observed in EGRIP and strain partitioning is therefore assumed to be present at the depth around 1360 m. This assumption is furthermore supported by the occurrence of a wavy eigenvalue pattern.

The wavy pattern of $\lambda_2$ and $\lambda_3$, observed at 550-850 m and below 1100 m, might be another indicator for strain partitioning. According to Richard and Tanner (1995) and Carreras et al. (2013), this deformation process is characterised by a heterogeneous distribution of the total strain on a body, regarding strain type (e.g. simple shear or pure shear) and strain intensity. The distribution of strain is influenced by boundary conditions, stress orientation, rheology and anisotropy. These factors operate individually or in combination with each other. The fluctuating strength of anisotropy observed in my samples, can be interpreted as an indicator for strain partitioning. Furthermore, strain partitioning has been observed in plastic and brittle regimes and on a wide range of scales: from the size of crystals to dimensions of tectonic plates (Richard and Tanner, 1995; Carreras et al., 2013). Ramsay and Huber (1984) showed, that strain partitioning enables the decomposition of the total strain into individual deformation modes on the crystal-scale, allowing accommodation of strain. The changing wavelength of the observed eigenvalue waves at EGRIP indicates different spatial scales of strain partitioning, ranging from centimetres (e.g.

1360 m) to 100 metres (550-850 m). Strain partitioning is common in regions, where compressive and extensive pure shear occur, and are additionally combined with a component of simple shear (Teyssier et al., 1995; Fossen et al., 1994; Fossen, 2010). This results in strain partitioning across the deforming region by the formation of a shear zone or a strike slip fault (Teyssier et al., 1995; Fossen et al., 1994). CPO analysis indicates a dominant extension deformation mode below 500 m, and will be further discussed in Chapter 4.3. To support these preliminary statements, results from different methods (e.g. Visual Stratigraphy and Radar measurements) have to be analysed, and eventually combined with microstructure data. To rely on the presented microstructure data only, is not sufficient.

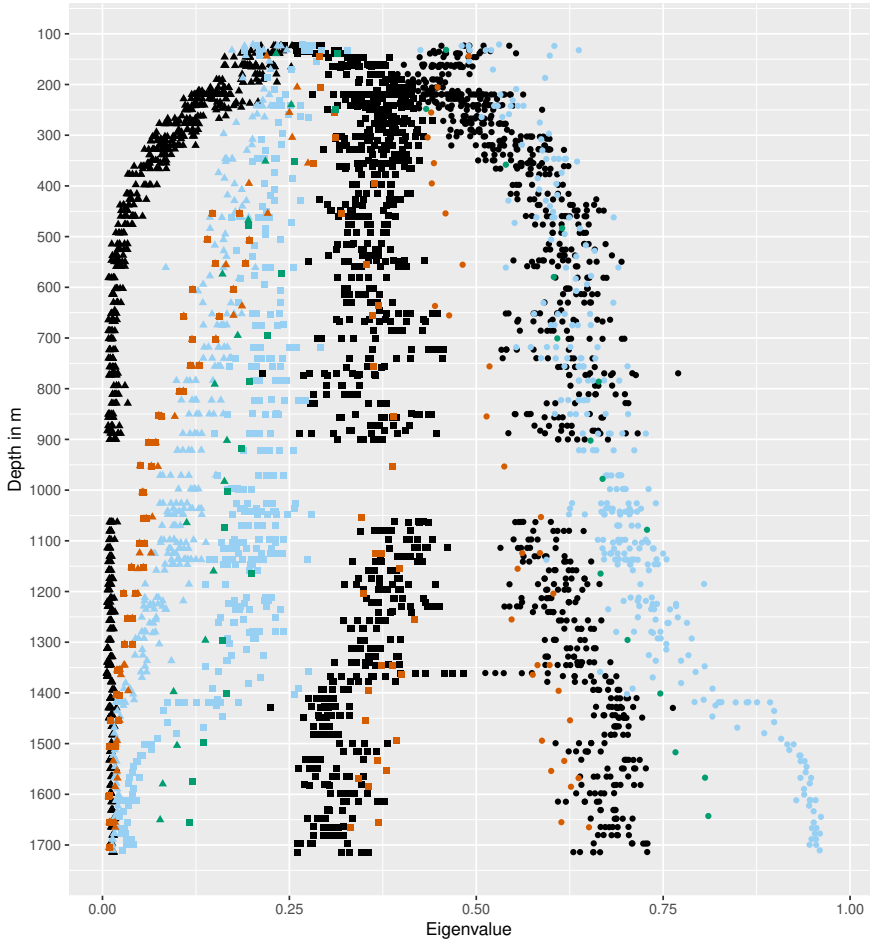


FIGURE 4.1: **Comparison of EGRIP with EDML, GRIP and NEEM**

EGRIP is shown in black, EDML in red, GRIP in green and NEEM in blue. Filled triangles represent $\lambda_1$, filled squares $\lambda_2$ and solid circles $\lambda_3$. Data from Weikusat et al. (2017) for EDML, Thorsteinsson et al. (1997) for GRIP, and Eichler (2013) and Montagnat et al. (2014) for NEEM.

A preliminary age model of S. O. Rasmussen and S. Mojtabavi (personal communication, 16 January 2019), based on the combination of data from *Electrical conductivity method* (ECM) and *Dielectric profiling* (DEP), was linearly interpolated to examine if distinct eigenvalue features might be linked to specific events in history, such as the *Roman Warm Period* or the *Glacial-Holocene* transition (Figure 4.3). It must

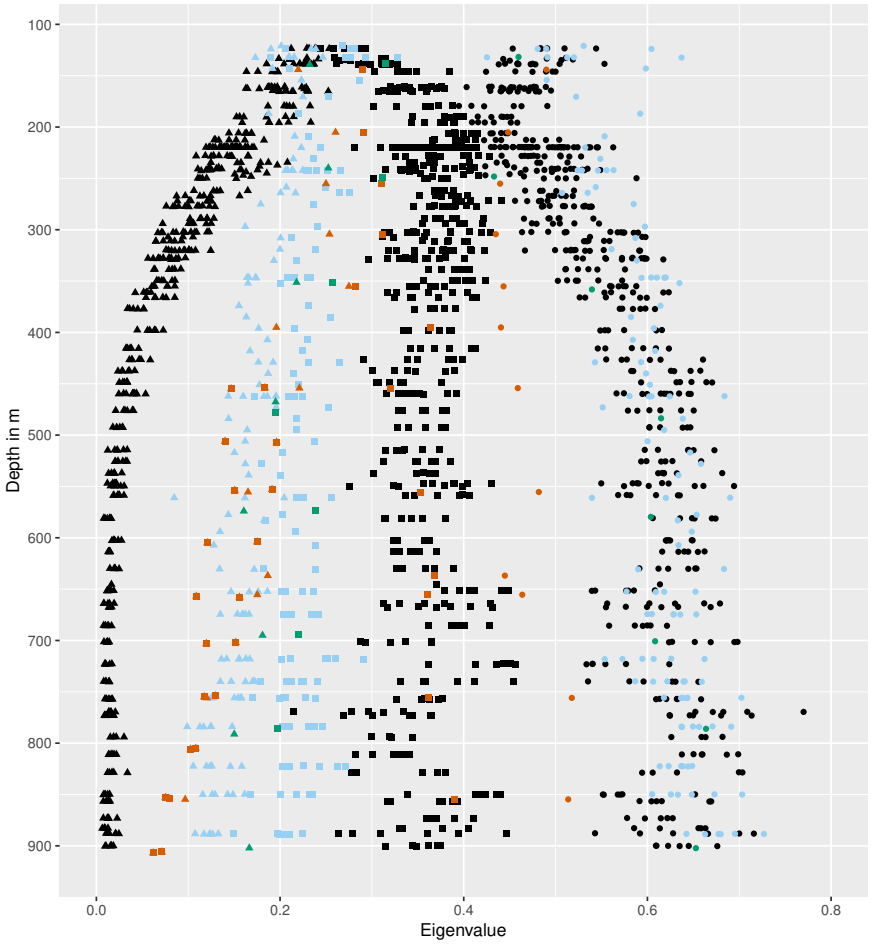


FIGURE 4.2: **The upper 900 m of EGRIP, EDML, GRIP and NEEM**

The same annotations as in Figure 4.1 are used.

be mentioned that the provided age model is preliminary and does not cover depths below 900 m; all values below were interpolated linearly for this study and are based on measurements from the upper 900 m. Another dating approach, valid for the entire core, is based on *Radio Echo Sounding* (RES) data and is in good agreement with the age model by Rasmussen and my interpolated values (D. Dahl-Jensen, personal communication, 18 November 2018). This RES data set indicates that the age-depth relationship is rather linear, and a non-linear relationship is expected to be present with the occurrence of the *Last Glacial* at a depth of ~1350 m. This linearity in age-depth relationship is probably caused by the compensation of upstream accumulation by flow velocity and strain rate of NEGIS (S. O. Rasmussen, personal communication, 18 November 2018). The strong increase in grain size around 1360 m, followed by decreasing grain size, and preliminary results from Visual Stratigraphy measurements also support the proposed depth of the *Glacial-Holocene* transition (J. Westhoff, personal communication, 30 January 2019). Therefore, the presented data in Figure 4.3 should be trustworthy, but should nevertheless be treated with caution until a complete age model has been established and verified.

The *Roman Warm Period* is represented in the ice core by the regime where the

crossed girdle CPO was observed and $\lambda_2$ and $\lambda_3$ have similar values. Beginning and ending of this period define the depth regime where both eigenvalues are ~0.4. The depth of 457-593 m represents one *Holocene Climate Optimum* and coincidences with the final decrease of $\lambda_1$ and the end of the increase of $\lambda_3$. The wide spread in eigenvalues between 700 and 900 m matches with the time of another *Holocene Climate Optimum*. Another striking feature is the exact alignment of the end of the *Last Glacial* and the prominent high and low values of $\lambda_2$ and $\lambda_3$, respectively. This observed consistency is not climatically driven, but most likely by the change of material and trace element content, combined with a feedback loop of deformation and recrystallisation as proposed by Eichler (2013) and Eichler et al. (2017).

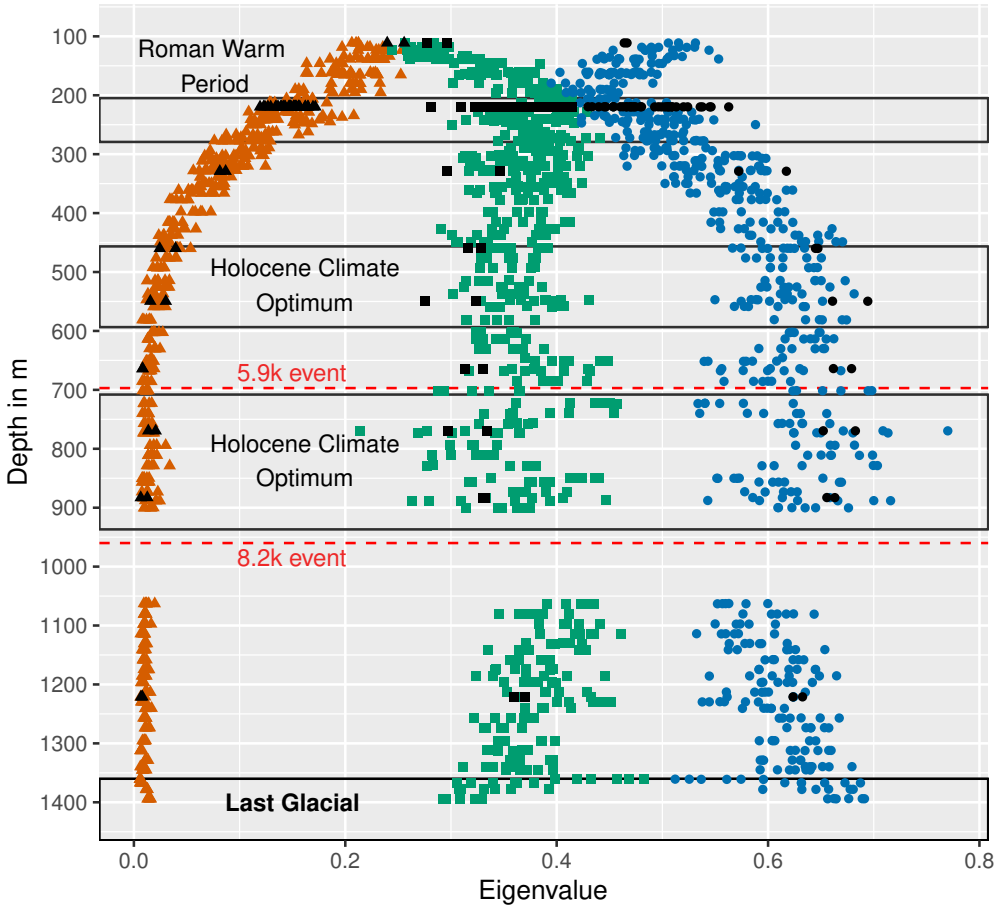


FIGURE 4.3: **Eigenvalue development linked to age**

Eigenvalue results linked to a preliminary age model by S. O. Rasmussen (personal communication, 16 January 2019). The same annotations as in Figure 3.1 is used.

## 4.2 Microstructure and grain properties

Figure 4.4 presents grain sizes of EDML, NEEM and EGRIP. In total all ice cores show similar absolute grain sizes. The grain size development with depth is similar for EGRIP and NEEM while EDML measurements display an increase in grain size

between 950 and 1650 m, which goes hand in hand with the beginning of the *Last Glacial* at 900 m for EDML. Grains from EGRIP have a higher variability and are up to 5 $mm^2$ larger between 111 and 600 m. This impression is probably influenced by the large difference in the number of measured samples in this depth regime. At NEEM, 557 samples were measured in total, contrarily to EGRIP, where almost 800 samples were measured in the upper 1714 m. Especially the upper 350 m were measured with a very high spatial resolution (5-10 m) and with up to six samples per depth. Below 600 m, grain sizes from NEEM increase to up to 12 $mm^2$ (750 m) while EGRIP results show lower grain sizes of 3-8 $mm^2$. After the brittle ice zone, grains from the EGRIP ice core show hardly any variability in size and decrease from 5 $mm^2$ to 2 $mm^2$. Results from NEEM display larger grain sizes until a depth of 1500 m, where both cores show the same mean grain size of ~2 $mm^2$. The data set for EDML is comparably small and only 57 samples were analysed regarding grain size. Due to this low amount, grain size seems to be less variable and the absolute values agree well with the other two ice cores, until a depth of 1050 m. This depth is reported to be the depth of the *Last Glacial* and below this depth, grain size increases steadily and values of up to 10.1 $mm^2$ (1550 m) were measured. This variation can be explained by the spatial difference between these cores, and therefore the difference in age and trace element content. EDML was drilled in the interior of *Dronning Maud Land*, East Antarctica, with the purpose to obtain a high-resolution palaeoclimate record to couple glacial climate variability in Greenland and Antarctica (Barbante et al., 2006). This study shows that EDML dates back to 150 000 years and that the *Last Glacial* starts around 900 m, while it starts at 1350 m at EGRIP and around 1400 m at NEEM (Ruth et al., 2007). According to Ruth et al. (2007), NEEM only dates to 130 000 years, supporting the fact that similar depths represent different times, and therefore different climatic conditions and trace element contents. Thus, it was expected that grain size data from EDML differs from EGRIP and NEEM.

The quantitative results regarding microstructure and especially grain shape, agree well with the manual analysis of high-resolution LASM images. In general, my perimeter ratio results range from 0.46 to 0.90 and are consequently lower than comparable measurements from EDML as presented by Weikusat et al. (2009b) and displayed in Figure 2.5. Standard deviations of EGRIP samples (Figure A.5) are up to twice as high as for EDML samples. High values for roundness were calculated for samples throughout the entire ice core and range from 1.93 to 17.64. These results indicate highly irregular grain shapes throughout the entire core, qualitatively supported by the analysis of more than 200 high-resolution LASM images, showing bulging and protruding grain boundaries in all analysed depths (Figure 3.9, 3.10 and A.6-A.23). This leads to the conclusion that grains of the EGRIP ice core are significantly more irregular shaped. Amoeboid grain shapes, sutured grain-boundaries and protruding grains were regularly found in LASM-images and are common for grains undergoing grain boundary migration (Passchier and Trouw, 2005). Furthermore, the observed clustering of small grains around larger grains is known as a *core*

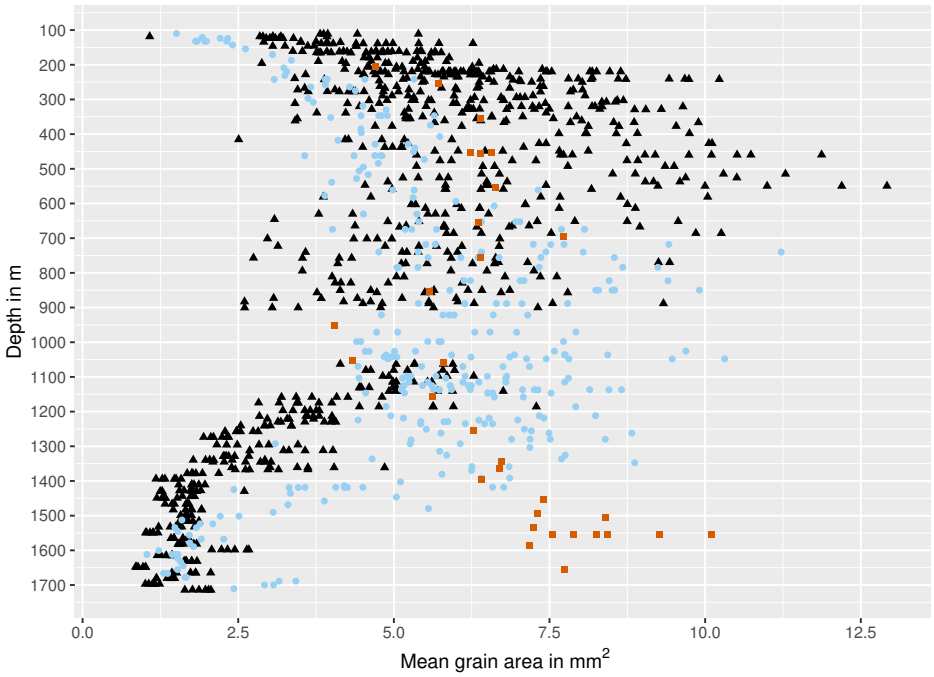


FIGURE 4.4: **Grain size in EGRIP, EDML and NEEM**

The same colours as in Figure 4.1 were used; filled triangles represent EGRIP, filled squares EDML, and solid circles NEEM. Displayed values represent the mean grain size of one entire sample. EDML data from Weikusat et al. (2009a), NEEM data from Eichler (2013) and Montagnat et al. (2014).

*and mantle structure* in structural geology and is interpreted as an indicator for recrystallisation (Passchier and Trouw, 2005). Urai et al. (1986) name all these features as characteristics of dynamic recrystallisation driven by deformation. Furthermore, all mentioned subgrain-boundary types by Weikusat et al. (2009b) occurred frequently in the analysed samples, accompanied by island grains, triple junctions and sutured grain-boundaries. These observations are indicators for a large amount of strain working on the grains, most likely caused by continuous deformation, which can be expected in a fast flowing ice stream.

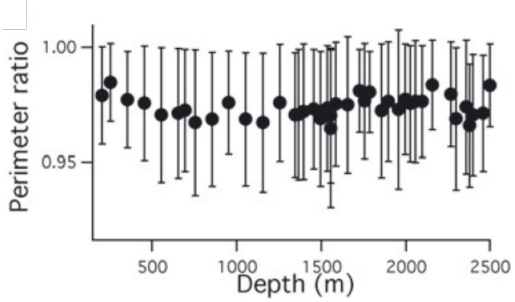


FIGURE 4.5: **Perimeter ratio in EDML**

Perimeter ratios for EDML from Weikusat et al. (2009b). Values are significantly higher than my presented values, indicating more irregular grains in the EGRIP ice core.

To summarise, my results regarding the microstructure of EGRIP, strongly indicate the occurrence of dynamic recrystallisation throughout the entire ice core as displayed in Figure 4.6. Compared to ice cores from lower dynamic sites (e.g. NEEM and EDML), this would mean that the onset of dynamic recrystallisation occurs in much shallower depth at EGRIP. Thus, NEGIS and its flow behaviour, are probably much more influenced by this mode and dynamic recrystallisation. There are small-scale numerical simulations which implement dynamic recrystallisation (Staroszczyk, 2011; Llorens et al., 2016; Steinbach et al., 2017), but this is not possible yet for models simulating ice dynamics on the scale of hundreds of kilometres or even more. The flow of ice furthermore depends on properties of individual ice crystals, such as crystal-preferred orientation and grain size. It is therefore essential to better understand the processes controlling the micro-dynamics of ice, eventually leading to the development of a physically based macroscopic ice flow law. To do this is very challenging, but it would be a big achievement to implement such a flow law into large-scale ice sheet models, enabling a better prediction of solid ice discharge by ice streams.

The presented data is derived by analysing thin sections, which are two-dimensional spot measurements. In reality, ice grains are highly-complex, three-dimensional bodies shaped by numerous processes during accumulation and densification (Cuffey and Paterson, 2010). Therefore, grain properties like grain size and perimeter ratio can be strongly biased by this two-dimensional point of view. Precautions were taken (e.g. only grains above a certain size threshold, i.e. 500 pixel, were analysed) but the restriction of this method should be kept in mind. It was tried to minimise the bias by incorporating data from horizontal thin sections, which showed that the derived values hardly differ from values derived from vertical sections. This positive outcome strengthens the trust in the confidence of the presented data.

## 4.3 Observed CPO patterns of the EGRIP ice core

The orientations of the c-axes of crystals in one sample are called fabric, or crystal preferred orientation. If strain acts on e.g. ice, the fabric normally changes and its shape depends on the dominating deformation mode. The two main processes changing the fabric pattern are:

- Rotation of c-axes due to applied stress;
- Recrystallisation leading to the formation of new grains with different orientations, compared to the host grain.

Information on deformational history, and rheological properties, can therefore be derived from the fabric of a sample (Kamb, 1972; Alley, 1988; Law, 1986; Thorsteinsson et al., 1997; Wang et al., 2002; Eichler, 2013; Montagnat et al., 2014; Weikusat et al., 2017).

Four different CPO patterns were observed in the upper 1714 m of the EGRIP ice core and proposed deformation modes are displayed in Figure 4.6. In the uppermost part, a broad single maximum was observed, followed by a Type I and II crossed girdle, which develops into a girdle of varying strength. In the deepest part, a CPO with horizontal maxima was observed for the very first time in polar ice.

In the upper part of the core, between 111 and 196 m, a broad single maximum CPO was observed, in which most c-axes are loosely vertical orientated and only a few are horizontally aligned (Figure 4.6). This pattern can be explained as the result of vertical compression from overlying layers (Dahl-Jensen et al., 1997; Thorsteinsson et al., 1997; Gusmeroli et al., 2012; Faria et al., 2014b) and is displayed in Figure 4.6. If crystals would not be constrained by their neighbours, their basal planes could easily glide over each other without changing their orientation. This is not the case, and basal planes have to rotate to enable compression, as shown by laboratory deformation experiments (Azuma and Higashi, 1985). Thus, the c-axes rotate towards the axis of compression, which is presumed to coincide with the core axis.

At 196 m, this CPO begins to transform into a crossed girdle CPO, which varies in type and shape (Figure 4.6). Crossed girdles of Type I and Type II were observed, with symmetric and asymmetric shapes. This CPO increases in distinctness and is clearly pronounced at 250 m. Crossed girdles have been observed in several studies, most commonly in quartz-containing rocks such as quartzites or shists (Lister, 1974; Lister et al., 1978; Lister and Williams, 1979; Lister and Hobbs, 1980; Behrmann and Platt, 1982; Carreras and Garcia Celma, 1982; Law et al., 1986; Law, 1986; Schmid and Casey, 1986). Similar CPO patterns in ice were only observed during laboratory deformation tests conducted by Kamb (1972), and later discussed by Alley (1992). These studies explain the occurrence of such a CPO pattern by the influence of dynamic recrystallisation and stress character. Studies by Wilson (1981), Wilson (1983), and Wilson et al. (2014) established the use of ice as an analogue for, especially quartz-rich, rocks. This is based on similarities regarding their crystal structure, ice is hexagonal and quartz often pseudo-hexagonal. It can therefore be assumed that quartz and ice crystals behave similar during deformation, resulting in resembling CPO patterns. This assumption is used to propose a hypothesis for the occurrence of the crossed girdle in the shallower part of the EGRIP ice core, and is discussed in detail in Chapter 4.4.

Below 294 m, the transition from a crossed girdle to a vertical girdle CPO commences and is displayed in Figure 4.6. In the following 80 metres, the distinction between both patterns is difficult and a distinct vertical girdle was observed for the first time at a depth of 376 m. Below 500 m, a vertical girdle is the only observed CPO and the alignment of c-axes along the vertical plane gets stronger throughout the next 700 m, caused by an increased influence of extensional deformation along flow direction. If the dominating stress regime is axial extension, crystals start to rotate and basal planes shift towards the direction of extension (Thorsteinsson et al., 1997; Wang et al., 2002). Hence, c-axes rotate away from the direction of extension

and girdle CPOs are produced (Thorsteinsson et al., 1997; Wang et al., 2002). Depending on the strength of extension, patterns are classified as *developing*, *developed* or *strong* girdle. The stronger a girdle, the more c-axes are orientated and the thinner appears the girdle (Paterson, 1994).

Below 1230 m, CPOs with (sub-) horizontal maxima were observed in varying strength, and are completely dominant between 1394 m and 1714 m (Figure 4.6). This pattern has not been observed in ice before, and formulating a well-elaborated hypothesis is outside of the scope of this thesis. Lister and Dornsiepen (1982) simulated similar CPO patterns for quartzite for constricted field conditions. It is likely that extensional deformation is accompanied by simple shear and basal slip (Passchier and Trouw, 2005). This preliminary hypothesis should be treated with caution and more research has to be conducted on this topic.

The calculated results of the Woodcock parameter agree with the impression derived by the CPO-analysis. The upper 100 m are characterised by very large values, indicating random c-axis orientations and isotropic material behaviour. Below a depth of 180 m, no measurements show Woodcock parameter values exceeding 1, representing the development towards a girdle fabric, as stated by Woodcock (1977), and displayed by the CPO development observed in the EGRIP ice core.

In rocks, the closing stage of the deformation history has an impact on the fabric, because it develops continuously on the grain scale, depending on the surrounding kinematic framework as shown by Lister and Hobbs (1980), Wilson (1981), and Wilson et al. (2014). This results in CPOs, which are influenced by modifications occurring at the closing stage of deformation, and might therefore, not represent the entire deformation history correctly. If dynamic recrystallisation is present, information about older deformation stages, stored in the CPO, might get erased by the formation of new grains with new c-axis orientations (Lister and Hobbs, 1980). This is important to mention, but is unlikely for samples analysed in this thesis. The examined samples are from a highly dynamic site, and the scientific focus is on deformation regimes which are caused by this particular setting. Thus, information about the deformation regimes at the onset of NEGIS are not the primary topic of interest.

CPO and grain size observed in the EGRIP ice core vary with depth as displayed in Figure 4.4 and 4.6. It can be expected that this microstructural difference leads also to a difference in viscosity (Cuffey and Paterson, 2010). This holds especially true for depth regimes with different ages, deformation historys and impurity contents, such as e.g. between Holocene and Glacial ice (Jones and Glen, 1969; Hammer, 1977; De Angelis et al., 1983; Barnes and Wolff, 2004). Ice dynamics are heavily influenced by the viscosity of the material, especially in the region close to bedrock, where ice is at temperatures just below the melting point (Paterson, 1994; Greve, 2005). As already mentioned by Weikusat et al. (2017) for EDML, first results from EGRIP challenge the "step-flow model" presented by Dansgaard and Johnsen (1969). They assume for ice divides, that in the upper two-thirds of an ice column, a constant vertical

strain rate occurs, decreasing linearly until there is no more vertical deformation at the bedrock. The lower third is dominated by shear deformation. This might hold true for areas of low flow velocity, but not for ice streams. The presented results are therefore a first step towards a more realistic representation of physical properties in ice. The implication of these factors into a flow law, which describes ice flow better than at the present state, is a highly complicated but uttermost important challenge in times of global warming and sea-level rise (IPCC, 2014).

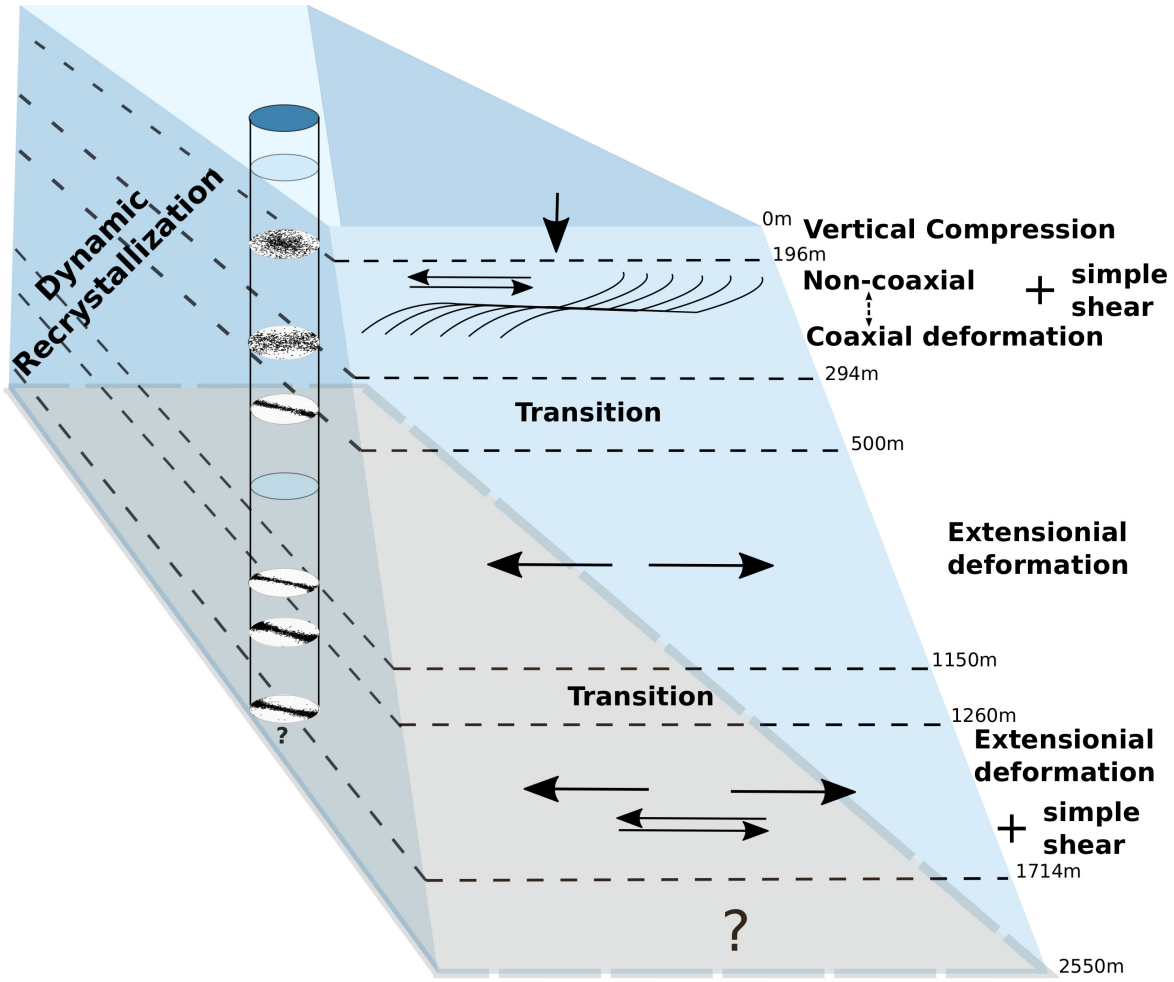


FIGURE 4.6: **Proposed deformation modes at EGRIP**

The observed CPO patterns in the EGRIP ice core (on the left) and the proposed deformation modes and transition zones. Deformation modes are simplified and the depth scale is not continuous. CPO patterns have been manually rotated and do not represent the direction of deformation.

## 4.4 The crossed girdle CPO in the EGRIP ice core

The combined results from analyses of microstructure and fabric, show a CPO evolution from a broad single maximum (118 m) towards symmetric and asymmetric crossed girdles of Type I and II (195-294 m). Below an intermediate transition depth, a great-circle single girdle starts to develop and reaches full strength at a depth of

500 m. Therefore, the occurrence of dynamically changing deformation modes in the upper 500 m of NEGIS is proposed, accompanied by an early onset of syntectonic dynamic recrystallisation, as already stated for quartz (Schmid and Casey, 1986; Passchier and Trouw, 2005).

The properties of a material undergoing deformation, depend on the previous strain path as well as on the current total strain (Hsu, 1966). This study stated the occurrence of two major types of strain path. If the principal axes of strain remain fixed with respect to the material, it is called coaxial deformation. If the principal axes of strain rotate, non-coaxial deformation takes place (Hsu, 1966). Figure 4.7 illustrates the effect of the type of strain on the geometry of the CPO patterns of coaxially deformed quartz, valid for low to intermediate grade metamorphic conditions. A theoretical model, based on the Taylor-Bishop-Hill analysis, was used to predict the CPO patterns in this figure (Lister et al., 1978; Lister and Hobbs, 1980). Experimental studies by Kamb (1972), Tullis et al. (1973), and Tullis and Yund (1977), and the analysis of naturally deformed quartzites by Schmid and Casey (1986), support these theoretical CPOs. For uniaxial compression, small circle girdle distributions are expected. These are connected by a central girdle in plain strain, producing crossed girdles of Type I. In the constrictive field, crossed girdles of Type II develop.

Schmid and Casey (1986) further proposed that a change in CPO, as displayed in Figure 4.8, might occur in a transition zone between pure shear and simple shear progressive deformation. The results presented in this thesis indicate that this transition zone is located roughly between 196 m and 500 m, and ends with a change in dominant deformation mode towards extensional deformation and thus, the occurrence of a clear vertical girdle as explained in Chapter 4.3 (Figure 4.6).

Variations in the exact CPO pattern can be accomplished by changes in the dominant slip system as explained by Passchier and Trouw (2005). They state that slip on the basal plane contributes mainly to c-axes located in the periphery of the CPO diagram, slip on rhomb planes to those in-between periphery and centre, and slip on prism planes to those in the centre. If prism slip is dominated by rhomb slip, Type II crossed girdles are more likely to develop (Bouchez, 1978; Schmid and Casey, 1986). The asymmetry observed in Type I and Type II crossed girdles can be explained by a fluctuation of deformation modes between non-coaxial and coaxial progressive deformation (Figure 4.6). This results in the stronger development of one of the parts of the c-axis pattern (Passchier and Trouw, 2005).

Carreras and Garcia Celma (1982), Schmid and Casey (1986), and Herwegh et al. (1997) observed symmetric and asymmetric c-axis girdles, formed in simple shear and with an intermediate stage showing asymmetric crossed girdles. For the analysed rocks, mostly quartz-rich types like quartzites, it was proposed that dynamic recrystallisation, by increasing strain, has an increasing effect on the CPO patterns. Recrystallisation enables the selective removal of grains in unfavourable orientations (for slip), resulting in the observed change of fabric, which was observed in naturally

deformed quartzites (Schmid and Casey, 1986) and theoretically modelled for trigonal or hexagonal material, such as quartz or ice (Jessell, 1988a; Jessell, 1988b). In these modelling studies, as well as in Jessell and Lister (1990), the Taylor-Bishop-Hill model for dislocation glide was modified by incorporating grain boundary migration and the nucleation of new grains. Results from these studies indicate that fabrics evolve continuously with deformation, producing (among others) crossed girdle CPOs for constant deformation conditions and a single deformation geometry. Contrary to results by Lister et al. (1978), modelling results by Jessell (1988b) indicate that a coupling of dislocation slip with dynamic recrystallisation produces a larger variation in CPOs than a model only considering glide as cause for lattice rotations.

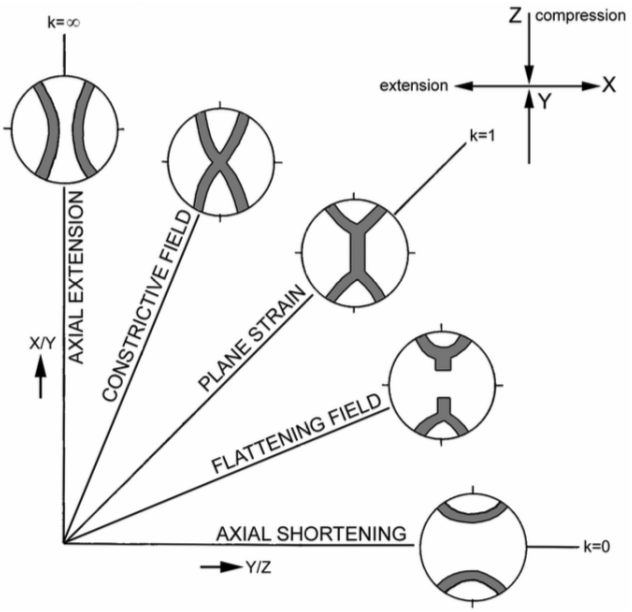


FIGURE 4.7: **Relation between CPO pattern of quartz and strain symmetry at coaxial progressive deformation**

Flinn diagram of the theoretical relationship between quartz CPO and strain under coaxial deformation. After Schmid and Casey (1986) and Lister and Hobbs (1980), displayed by Vernooji (2005). The strain shape k describes the slope between the abscissa axis and the line joining the ellipsoid and the origin of the diagram.

This indicates for the EGRIP ice core, that at a depth regime of roughly 100 m (between 196 and 294 m), the dominant deformation mode switches back and forth between coaxial deformation (basal slip dominant) and progressive simple shear (Figure 4.6). This shift might be caused by an increased rotational component of strain path or increased strain in simple shear. These processes are proposed to be accompanied by 1) the elimination of locked up grains by grain boundary migration and 2) the occurrence of partially reoriented grains due to selective recrystallisation (Behrmann and Platt, 1982; Law et al., 1986). This assumption is based on the observations explained in Chapter 4.1 and 4.2. The proposed modes presumably lead to the observed crossed girdle CPOs, which were found for the first time in natural ice. Below the strong occurrence of crossed girdle CPOs, a transition zone is proposed to

exist between 294 m and 500 m (Figure 4.6). In this zone, the crossed girdle pattern weakens and a classic girdle CPO develops as displayed in Figure 4.8.

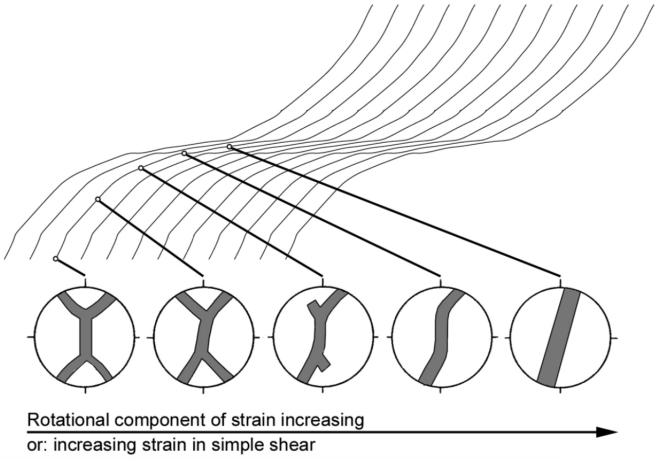


FIGURE 4.8: **Change of quartz CPO pattern in a ductile shear zone under plane strain**

From left to right: the observed CPO patterns change from a Type I crossed girdle to a weak, asymmetric crossed girdle, which develops into a weak, and finally, fully developed vertical girdle. After Schmid and Casey (1986), displayed by Vernooji (2005).

## 4.5 Classification of EGRIP depth regimes

Based on the presented results regarding eigenvalue, grain size and perimeter ratio, the EGRIP ice core is divided into six depth regimes, as displayed in Table 4.1.

1. 111-250 m: High perimeter ratio and small grain size. Rapid decrease of $\lambda_1$ and intersecting of $\lambda_2$ and $\lambda_3$.

2. 250-550 m: Decrease in perimeter ratio and slight increase in grain size, accompanied by a large grain size variability. Further decrease of $\lambda_1$ and separation of $\lambda_2$ and $\lambda_3$.

3. 550-760 m: Further decrease in perimeter ratio towards absolute minimum and decrease in grain size and grain size variability. Small $\lambda_1$ and wavy pattern of $\lambda_2$ and $\lambda_3$.

4. 760-900 m: Increase in perimeter ratio and constant grain size. Small $\lambda_1$, increase of $\lambda_2$ and decrease of $\lambda_3$.

5. 1062-1360 m: Increase in perimeter ratio and maximum variability at 1360 m, rapid decrease in grain size and grain size variability. Constantly small $\lambda_1$ and slight diverging trend between $\lambda_2$ and $\lambda_3$.

6. 1360-1714 m: Maximum perimeter ratio and minimum grain size. $\lambda_1$ very small and further separation of $\lambda_2$ and $\lambda_3$.

Each of these sections has specific characteristics and all three mentioned parameters display certain features and developments at similar depths. These features include absolute values, the variability of these values and the occurrence of large changes on small spatial scales.

Supported by fabric and CPO results, it can be suggested that various dominant deformation modes occur throughout the core, accompanied by continuous dynamic recrystallisation. The influence of these modes seems to vary for each depth regime, but a general classification is proposed in 4.3 and displayed in Figure 4.6.

To the best of current knowledge, this classification is proposed in addition to the observed deformation regimes explained in Chapter 4.3 and 4.4. Additional data from the field and laboratory will augment and better constrain these preliminary results. Especially the lack of data in the brittle ice zone led to the separation of regime 4 and 5. This data should be available after the next drilling season and these two regimes might be merged. It is also possible that the entire ice core, once all microstructure and fabric data is available, is divided only into three or four larger regimes. Furthermore, the linking of the presented data to results from visual stratigraphy and large-scale radar measurements might change the applied classification.

TABLE 4.1: **EGRIP depth regimes**

| **Depth [m]** | **Grain Size** $[mm^2]$ | **Perimeter Ratio** | $\lambda_1$ | $\lambda_2$ | $\lambda_3$ |
|---|---|---|---|---|---|
| 111-250 | 4.3±1.6 | 0.83±0.15 | 0.18±0.039 | 0.35±0.043 | 0.47±0.035 |
| 250-550 | 6.6±1.9 | 0.82±0.16 | 0.07±0.035 | 0.37±0.030 | 0.57±0.052 |
| 550-760 | 6.0±1.7 | 0.78±0.17 | 0.02±0.005 | 0.37±0.039 | 0.61±0.039 |
| 760-900 | 5.5±1.5 | 0.79±0.17 | 0.01±0.005 | 0.35±0.049 | 0.64±0.047 |
| 1062-1360 | 3.8±1.2 | 0.84±0.15 | 0.01±0.002 | 0.39±0.034 | 0.60±0.034 |
| 1360-1714 | 1.6±0.4 | 0.86±0.14 | 0.01±0.002 | 0.31±0.027 | 0.68±0.027 |

# 5 Conclusion and Outlook

The aim of this thesis was to display and discuss the microstructural and fabric properties of the EGRIP ice core, obtained during the field seasons 2017 and 2018. This information allows a detailed glimpse into the physical processes affecting the ice of a fast flowing ice stream, a possibility that occurred for the very first time. Besides the examination of established geological parameters regarding the microstructure (such as grain size, grain shape and grain boundaries), the main focus of this thesis was put on the c-axis distribution and the CPO development.

The unique location of the EGRIP ice core, derived from a fast flowing ice stream, has the potential to be another big step towards a more detailed understanding of the rheology of ice. Accomplishing this, is without doubt a challenging task, and the presented thesis hopefully aids in the attempt to tackle it.

Almost 800 thin sections, from the upper 1714 m of the EGIP ice core, were analysed regarding microstructural and fabric properties. 275 measurements were conducted in the field season of 2017; the remaining 522 measurements were conducted in 2018, partly by myself. C-axis distribution data was obtained by an automated Fabric Analyser and used to derive information about CPO-, eigenvalue- and eigenvector-development. My results show a more rapid evolution of anisotropy with depth, compared to lower dynamic sites such as EDML, GRIP or NEEM. Especially the smallest eigenvalue $\lambda_1$ decreases quickly with depth. $\lambda_2$ and $\lambda_3$ intersect in shallow depth and diverge from there on in a wavy-pattern form. The eigenvectors of 47 samples have been calculated, and a tilting of the largest eigenvector from the vertical axis to the horizontal axis has been observed. A preliminary age model was interpolated until a depth of 1360 m, and it was examined if it was possible to link climatic events to the rapid development of anisotropy observed in the EGRIP ice core. The depth regime around 1360 m, probably the Glacial-Holocene transition, was examined in detail due to the occurrence of several interesting features in fabric and microstructure.

Grain shape-related parameters, such as grain size, perimeter ratio and roundness, were analysed and partly compared to data from EDML and NEEM. EGRIP samples showed much more irregular grain shapes than grains from EDML. Mean grain sizes and grain size developments with depth were similar to results from NEEM and EDML, even though results from EDML differed significantly in the lower part of the core due to the different age of the corresponding depth regimes. These measurements were supported by a qualitative analysis of more than 200 high-resolution images, derived by a LASM. Indicators of dynamic recrystallisation

were observed in every examined depth, e.g. island grains, amoeboid grain shapes, protruding grains and the frequent occurrence of three different types of subgrain-boundaries.

To formulate a preliminary deformation regime record, crystal-preferred orientations of the c-axis were analysed and discussed. My findings indicate vertical compression down to a depth of 196 m, represented by a broad single maximum CPO. Between 196-294 m, a novel CPO for natural ice was observed: the crossed girdle of Type I and II. Its occurrence has been explained by an early onset of dynamic recrystallisation accompanied by the activation of multiple slip-systems. Most likely, this is caused by a small scale change in the dominating deformation mode, switching between pure shear and simple shear progressive deformation. Changes in the dominant slip-system result in variations of the pattern, and a fluctuation between non-coaxial and coaxial progressive deformation explains the occurrence of symmetric and asymmetric crossed girdles. Below the crossed girdle pattern, a vertical girdle develops due to extensional deformation, and can be found between 500 and 1150 m. From this depth on, a vertical girdle with horizontal maxima was observed for the first time in natural ice. This CPO might be caused by extensional deformation accompanied by simple shear, but more work has to be conducted to support this preliminary hypothesis. Based on the presented results, the EGRIP ice core was divided into different depth regimes. One classification was based on grain properties, while a second one was based on the dominating deformation modes. Both classifications are important to understand the flow behaviour of an ice stream better, because deformation and grain properties are essential for flow on the micro-scale, and therefore also on larger scales.

The presented major findings of this thesis, the early onset and permanent occurrence of dynamic recrystallisation and several dynamically changing deformation regimes inside NEGIS, have to be taken into account when setting up realistic boundary conditions for ice-sheet models. The anisotropy of the ice develops more rapid than in ice from low dynamic sites and internal shear zones seem to be present, resulting in a different material behaviour of ice, which is not implemented in these models yet. Having this information is important to correctly calculate the flow behaviour of NEGIS and probably ice streams in general, improving our understanding of future ice mass loss and therefore sea-level rise.

This thesis is one small step on the long way towards a better understanding of NEGIS, and therefore ice stream dynamics. The next step is to successfully finish drilling at the EGRIP drilling site in 2019, or 2020. Data from the last ~800 m is eagerly anticipated, (1) to fill the brittle ice zone gap and (2) to give a first glimpse into the oldest parts of the ice. The EGRIP drill team expects the deepest part of the ice core to be the most challenging one (T. Popp, 16 November 2018). It is therefore questionable if bedrock can be reached in 2019. If so, a completely processed fabric and CPO data set might be available by the end of 2019. The already derived volume

samples should be analysed in more detail and further volume cuts should be measured in the upcoming months. A reliable new method, to fully produce and analyse a three-dimensional data set is still being developed and different approaches have to be tested. Even though time consuming, this approach has the potential to deliver a more realistic insight into three-dimensional ice crystals and their physical properties, than two-dimensional spot measurements. Especially parameters like grain size or perimeter ratio can be strongly biased by this two-dimensional point of view, but so far, no more accurate method has been established.

The crossed girdle and the briefly introduced findings of horizontal maxima CPOs, starting at ~1150 m, should be analysed in more detail in future studies. The occurrence of these CPO pattern is an indicator for modes and/or deformation regimes, which have not been observed before in natural ice. Further high-resolution case studies should be conducted and it would be interesting to derive information about the possible involvement of different slip-systems by analysing some samples with e.g. EBSD or X-ray Laue diffraction. These devices enable measurements of the a-axes distribution and will support or contest my interpretations. Two depth regions of the EGRIP ice core will be measured with EBSD at the University of Utrecht, Netherlands, to become more certain about the general deformation history of the core. If these measurements turn out to be successful, there might be the possibility to start a broader EBSD measuring campaign, or at least to increase the available data set by some more measurements in certain areas of interest.

Already decades ago, theoretical models predicted the possibility of the occurrence of crossed girdle CPOs in ice. The major progress in available computer power might be used to extend established models or to set up new ones, further investigating the rheology of ice and the influence of recrystallisation during deformation. Similar experiments were already conducted in recent studies by e.g Llorens et al. (2016), Steinbach et al. (2017), and Bons et al. (2018), but the new findings from EGRIP would certainly improve these approaches.

It is a time-consuming work to fully process, and quantitatively analyse, high-resolution images derived by LASM. Image processing of this data has extensively high computing costs and the AWI supercomputer *Ollie* has to be used to do so. Thus, only data from 2017 has been fully processed so far and more, qualified manpower is needed to do derive more infromation about the microstructure of the EGRIP ice core.

Besides the mentioned projects, related work is currently done at several research institutes, involving different approaches with different spatial and temporal scales. Airborne-radar-, visual stratigraphy- and dielectric profiling measurements will all have to be put in context to understand the big picture. A very recent study by Eichler et al. (2019, accepted) combines EDML microstructure data with impurity and isotope data, examining in detail links between the rheology of ice and its composition. This approach might be adapted to Greenland, and dynamic ice streams by using the applied method on measurements from EGRIP.

Another interesting approach is the use of polarimetric measurements with a phase-sensitive radio echo sounder (pRES), which allows to derive information about ice anisotropy from the surface, in a nondestructive way and without the need to drill a deep ice core. First polarimetric pRES results from the upper 1000 m agree well with my results, also indicating a rapid evolution of anisotropy in the upper hundred metres, followed by a stable anisotropic layer down to 1000m (O. Zeising, personal communication 17 January 2019). Further measurements with this method are planned for the upcoming EGRIP season to investigate the change in anisotropy along NEGIS. This additional data might help to better understand the deformation modes at EGRIP and the general flow pattern of NEGIS, allowing further insights into the ice up- and/or downstream of EGRIP.

The Greenland Ice Sheet loses vast amounts of ice each year, and even though it is less prominent, a similar trend has been observed in Antarctica over the last years. Greenland and Antarctica differ in several ways, and it is therefore necessary to conduct a drilling project similar to EGRIP on an Antarctic ice stream, e.g. on one of the *Siple Coast Ice Streams*. This work would help to verify results from EGRIP, and enables a broader applicability of the results presented here.

# Bibliography


Alley, R. B., D. D. Blankenship, C. R. Bentley, and S. T. Rooney (1986). "Deformation of till beneath ice stream B, West Antarctica". In: *Nature* 322, p. 57. URL: https://doi.org/10.1038/322057a0http://10.0.4.14/322057a0.

Alley, Richard B. (1988). "Fabrics in polar ice sheets: Development and prediction". In: *Science* 240.4851, pp. 493–495. ISSN: 00368075. DOI: 10.1126/science.240.4851.493.

— (1992). "Flow-law hypotheses for ice-sheet modeling". In: *Journal of Glaciology* 38.129.

Aschwanden, Andy, Mark A. Fahnestock, and Martin Truffer (2016). "Complex Greenland outlet glacier flow captured". In: *Nature Communications* 7.May 2015, pp. 1–8. ISSN: 20411723. DOI: 10.1038/ncomms10524. URL: http://dx.doi.org/10.1038/ncomms10524.

Ashby, M. F. and Paul Duval (1985). "The Creep of Polycrystalline Ice". In: *Cold Regions Science and Technology* 11, pp. 285–300.

Azuma, N. and A. Higashi (1985). "Formation processes of ice fabric pattern in ice sheets". In: *Annals of Glaciology* 6.120, pp. 130–134. ISSN: 02603055. DOI: 10.1145/3209219.3209221.

Bamber, Jonathan L., David G. Vaughan, and Ian Joughin (2000). "Widespread complex flow in the interior of the antarctic ice sheet". In: *Science* 287.5456, pp. 1248–1250. ISSN: 00368075. DOI: 10.1126/science.287.5456.1248.

Barbante, C. et al. (2006). "One-to-one coupling of glacial climate variability in Greenland and Antarctica". In: *Nature* 444.7116, pp. 195–198. ISSN: 14764687. DOI: 10.1038/nature05301.

Barnes, Piers R.F. and Eric W. Wolff (2004). "Distribution of soluble impurities in cold glacial ice". In: *Journal of Glaciology* 50.170, pp. 311–324. ISSN: 00221430. DOI: 10.3189/172756504781829918.

Behrmann, J. H. and J. P. Platt (1982). "Sense of nappe emplacement from quartz c-axis fabrics; an example from the Betic Cordilleras (Spain)". In: *Earth and Planetary Science Letters* 59.1, pp. 208–215. ISSN: 0012821X. DOI: 10.1016/0012-821X(82)90126-1.

Benn, Douglas I. and David J. A. Evans (2010). "Snow, Ice and Climate". In: *Glaciers and Glaciation*.

Bennett, Matthew R. (2003). "Ice streams as the arteries of an ice sheet: Their mechanics, stability and significance". In: *Earth-Science Reviews* 61.3-4, pp. 309–339. ISSN: 00128252. DOI: 10.1016/S0012-8252(02)00130-7.

Bentley, Charles R. (1987). "Antarctic Ice Streams: A Review". In: *Journal of Geophysical Research* 92.B9, pp. 8843–8858.

Bons, P. D., T. Kleiner, M. G. Llorens, D. J. Prior, T. Sachau, I. Weikusat, and D. Jansen (2018). "Greenland Ice Sheet: Higher Nonlinearity of Ice Flow Significantly Reduces Estimated Basal Motion". In: *Geophysical Research Letters* 45.13, pp. 6542–6548. ISSN: 19448007. DOI: 10.1029/2018GL078356.

Borradaile, Graham (2003). *Statistics of Earth Science Data*. 1st ed. Berlin, Heidelberg: Springer Berlin Heidelberg, p. 351. ISBN: 978-3-642-07815-6. DOI: 10.1007/978-3-662-05223-5. URL: http://link.springer.com/10.1007/978-3-662-05223-5.

Bouchez, Jean-Luc (1978). "Preferred orientations of quartz <a> axes in some tectonites: kinematic inferences". In: *Tectonophysics* 49, pp. 25–30.

Broeke, M. van den, J. Bamber, J. Ettema, E. Rignot, E. Schrama, W. J. van de Berg, E. van Meijgaard, I. Velicogna, and B. Wouters (2009). "Partitioning Recent Greenland Mass Loss". In: *Science* 326.5955, pp. 984–986. ISSN: 0036-8075. DOI: 10.1126/science.1178176. URL: http://www.sciencemag.org/cgi/doi/10.1126/science.1178176.

Carreras, J. and A. Garcia Celma (1982). "Quartz of C-Axis fabric variation at the margins of a shear zone developed in schists from Cap de Creus (Spain)". In: *Acta Geologica Hispanica* 17.3, pp. 137–149. ISSN: 0012-1622.

Carreras, Jordi, John W. Cosgrove, and Elena Druguet (2013). "Strain partitioning in banded and/or anisotropic rocks: Implications for inferring tectonic regimes". In: *Journal of Structural Geology* 50, pp. 7–21. ISSN: 01918141. DOI: 10.1016/j.jsg.2012.12.003. URL: https://linkinghub.elsevier.com/retrieve/pii/S019181411200274X.

Conway, H., G. Catania, C. F. Raymond, A. M. Gades, T. A. Scambos, and H. Engelhardt (2002). "Switch of flow direction in an antarctic ice stream". In: *Nature* 419.6906, pp. 465–467. ISSN: 00280836. DOI: 10.1038/nature01081.

Cuffey, K. M. and W. S. B. Paterson (2010). *The Physics of Glaciers*. Elsevier Science. ISBN: 9780080919126. URL: https://books.google.de/books?id=Jca2v1u1EKEC.

Dahl-Jensen, D., T. Thorsteinsson, R. Alley, and H. Shoji (1997). "Flow properties of the ice from the Greenland Ice Core Project ice core: The reason for folds?" In: *Journal of Geophysical Research: Oceans* 102.C12, pp. 26831–26840. ISSN: 21699291. DOI: 10.1029/97JC01266.

Dansgaard, W. and S. J. Johnsen (1969). "A Flow Model and a Time Scale for the Ice Core from Camp Century, Greenland". In: *Journal of Glaciology* 8.53, pp. 215–223. ISSN: 0022-1430. DOI: 10.3189/S0022143000031208. URL: https://www.cambridge.org/core/product/identifier/S0022143000031208/type/journal_article.

Dansgaard, Willi (1952). "Use of stable isotopes in biological research". In: *Ugeskrift for laeger* 114.36, 1209—1213. ISSN: 0041-5782. URL: http://europepmc.org/abstract/MED/13029191.

De Angelis, M., M. Legrand, J. R. Petit, N. I. Barkov, Ye S. Korotkevitch, and V. M. Kotlyakov (1983). "Soluble and insoluble impurities along the 950 m deep Vostok ice core (Antarctica) - Climatic implications". In: *Journal of Atmospheric Chemistry* 1.3, pp. 215–239. ISSN: 01677764. DOI: 10.1007/BF00058730.

Drury, Martyn R. and J. L. Urai (1990). "Deformation-related recrystalization processes". In: *Tectonophysics* 172, pp. 235–253.

Duval, P., M. F. Ashby, and I. Anderman (1983). "Rate-controlling processes in the creep of polycrystalline ice". In: *The Journal of Physical Chemistry* 87.21, pp. 4066–4074. ISSN: 0022-3654. DOI: 10.1021/j100244a014. URL: http://pubs.acs.org/doi/abs/10.1021/j100244a014.

Eichler, Jan (2013). "C-axis analysis of the NEEM ice core: an approach based on digital image processing". PhD thesis. Freie Universität Berlin, p. 73.

Eichler, Jan, Ina Kleitz, Maddalena Bayer-Giraldi, Daniela Jansen, Sepp Kipfstuhl, Wataru Shigeyama, Christian Weikusat, and Ilka Weikusat (2017). "Location and distribution of micro-inclusions in the EDML and NEEM ice cores using optical microscopy and in situ Raman spectroscopy". In: *Cryosphere* 11.3, pp. 1075–1090. ISSN: 19940424. DOI: 10.5194/tc-11-1075-2017.

Fahnestock, Mark, Robert Bindschadler, Ron Kwok, and Ken Jezek (1993). "Greenland Ice Sheet Surface Properties and Ice Dynamics from ERS-1 SAR Imagery". In: *Science* 262.5139, 1530 LP –1534. DOI: 10.1126/science.262.5139.1530. URL: http://science.sciencemag.org/content/262/5139/1530.abstract.

Fahnestock, Mark, Waleed Abdalati, Ian Joughin, John Brozena, and Prasad Gogineni (2001). "High Geothermal Heat Flow, Basal Melt, and the Origin of Rapid Ice Flow in Central Greenland". In: *Science* 294.5550, 2338 LP –2342. DOI: 10.1126/science.1065370. URL: http://science.sciencemag.org/content/294/5550/2338.abstract.

Faria, Sérgio H., Ilka Weikusat, and Nobuhiko Azuma (2014a). "The microstructure of polar ice. Part I: Highlights from ice core research". In: *Journal of Structural Geology* 61, pp. 2–21. ISSN: 01918141. DOI: 10.1016/j.jsg.2013.09.010. URL: http://dx.doi.org/10.1016/j.jsg.2013.09.010https://linkinghub.elsevier.com/retrieve/pii/S0191814113001740.

Faria, Sérgio H, Ilka Weikusat, and Nobuhiko Azuma (2014b). "The microstructure of polar ice. Part II: State of the Art". In: *Journal of Structural Geology* 61, pp. 21–49. DOI: 10.1016/j.jsg.2013.09.010. URL: http://dx.doi.org/10.1016/j.jsg.2013.11.003%5Cnpapers2://publication/doi/10.1016/j.jsg.2013.11.003https://linkinghub.elsevier.com/retrieve/pii/S0191814113001740.

Fossen, Haakon (2010). *Structural Geology*. Cambridge: Cambridge University Press. ISBN: 9780511777806. DOI: 10.1017/CBO9780511777806. URL: http://ebooks.cambridge.org/ref/id/CBO9780511777806.

Fossen, Haakon, Basil Tikoff, and Christian Teyssier (1994). "Strain modeling of transpressional and transtensional deformation". In: *Norsk Geologisk Tidsskrift1* 74, pp. 134–145.

Glen, J. W. (1952). "Experiments on the Deformation of Ice". In: *Journal of Glaciology* 2.12, pp. 111–114. ISSN: 0022-1430. DOI: 10.3189/S0022143000034067. URL: https://www.cambridge.org/core/product/identifier/S0022143000034067/type/journal_article.

Gow, Anthony J. (1974). "Time — temperature dependence of sintering in perennial isothermal snowpacks When a mass of metal or ceramic particles is heated the individual particles become bonded together and the aggregate densifies . Extensive grain growth may also occur and the en". In: *Snow Mechanics Symposium*.

— (1994). "Post-drilling recrystallization of the Byrd Station deep ice core and its relevance to current and future deep-core drilling on polar ice sheets". In: *Annals of Glaciology* 20, pp. 231–236. ISSN: 0260-3055. DOI: 10.3189/172756494794587005. URL: https://www.cambridge.org/core/product/identifier/S0260305500016505/type/journal_article.

Gow, Anthony J. and Terrence Williamson (1976). "Rheological implications of the internal structure and crystal fabrics of the West Antarctic ice sheet as revealed by deep core drilling at Byrd Station". In: *GSA Bulletin* 87.12, pp. 1665–1677. ISSN: 0016-7606. DOI: 10.1130/0016-7606(1976)87<1665:RIOTIS>2.0.CO;2. URL: https://dx.doi.org/10.1130/0016-7606(1976)87%3C1665:RIOTIS%3E2.0.COhttp://0.0.0.2.

Greve, Ralf (2005). *Dynamics of ice sheets and glaciers*. ISBN: 978-3-642-03414-5. DOI: 10.3189/002214311798043717.

Gusmeroli, Alessio, Erin C. Pettit, Joseph H. Kennedy, and Catherine Ritz (2012). "The crystal fabric of ice from full-waveform borehole sonic logging". In: *Journal of Geophysical Research: Earth Surface* 117.3, pp. 1–13. ISSN: 21699011. DOI: 10.1029/2012JF002343.

Hammer, C. U. (1977). "Past volcanism revealed by Greenland Ice Sheet impurities". In: *Nature* 270.5637, pp. 482–486. ISSN: 00280836. DOI: 10.1038/270482a0.

Henri, Bader (1962). *Scope, Problems, and Potential Value of deep ice Core Drilling in Ice Sheets.* Tech. rep. Miami: Miami University, College of Engineering.

Herron, Susan, Hoar, and Chester C. Langway (1979). "The Debris-Laden Ice at the Bottom of the Greenland Ice Sheet". In: *Journal of Glaciology* 23.89, pp. 193–207. ISSN: 0022-1430. DOI: 10.1017/S002214300002983X. URL: https://www.cambridge.org/core/product/identifier/S002214300002983X/type/journal_article.

Herron, Susan L. and Chester C. Langway (1982). "A Comparison of Ice Fabrics and Textures at Camp Century, Greenland and Byrd Station, Antarctica". In: *Annals of Glaciology* 3, pp. 118–124. ISSN: 0260-3055. DOI: 10.3189/S0260305500002639. URL: https://www.cambridge.org/core/product/identifier/S0260305500002639/type/journal_article.

Herwegh, Marco, Mark R. Handy, and Renée Heilbronner (1997). "Temperature- and strain-rate-dependent microfabric evolution in monomineralic mylonite: Evidence from in situ deformation of norcamphor". In: *Tectonophysics* 280.1-2, pp. 83–106. ISSN: 00401951. DOI: 10.1016/S0040-1951(97)00139-X.

Hobbs, P. (1974). *Ice Physics*. Ed. by P. Hobbs. 1st ed. Oxford: Oxford University Press, p. 837. DOI: 10.1002/ejoc.201200111.

Hondoh, T. (2000). "Nature and behavior of dislocations in ice". In: *Physics of Ice Core Records*, pp. 3–24.

Hsu, T C (1966). "The characteristics of coaxial and non-coaxial strain paths". In: *Journal of Strain Analysis* 1.3, pp. 216–222. ISSN: 0022-4758. DOI: 10.1243/03093247V013216. URL: https://doi.org/10.1243/03093247V013216.

IPCC (2013). "IPCC 13 Observations: Cryosphere". In: *Climate Change 2013: The Physical Sci- ence Basis. Contribution of Working Group I to the Fifth Assessment Report of the Intergovernmental Panel on Climate Change*, pp. 317–382. ISSN: ISBN 978-1-107-66182-0. DOI: 10.1017/CBO9781107415324.012.

— (2014). *Climate change 2014. Synthesis report. Versión inglés*, pp. 2–26. ISBN: 9789291691432. DOI: 10.1017/CBO9781107415324.

Jackson, A. G. (1991). "Slip Systems". In: *Handbook of Crystallography: For Electron Microscopists and Others*. New York, NY: Springer New York, pp. 83–88. ISBN: 978-1-4612-3052-6. DOI: 10.1007/978-1-4612-3052-6{_}7. URL: https://doi.org/10.1007/978-1-4612-3052-6_7.

Jansen, Daniela, Ilka Weikusat, Thomas Kleiner, Frank Wilhelms, Dorthe Dahl-jensen, Sepp Kipfstuhl, and Heinrich Miller (2017). "In situ-measurement of ice deformation from repeated borehole logging of". In: *Geophysical Research Abstracts* 19.EGU General Assembly 2017. URL: https://meetingorganizer.copernicus.org/EGU2017/EGU2017-16368.pdf.

Jessell, M. W. and G. S. Lister (1990). "A simulation of the temperature dependence of quartz fabrics". In: *Geological Society, London, Special Publications* 54.1, 353 LP – 362. DOI: 10.1144/GSL.SP.1990.054.01.31. URL: http://sp.lyellcollection.org/content/54/1/353.abstract.

Jessell, M.W. (1988a). "Simulation of fabric development in recrystallizing aggregates—I. Description of the model". In: *Journal of Structural Geology* 10.8, pp. 771–778. ISSN: 0191-8141. DOI: 10.1016/0191-8141(88)90093-4. URL: https://www.sciencedirect.com/science/article/pii/0191814188900934.

— (1988b). "Simulation of fabric development in recrystallizing aggregates—II. Example model runs". In: *Journal of Structural Geology* 10.8, pp. 779–793. ISSN: 0191-8141. DOI: 10.1016/0191-8141(88)90094-6. URL: https://www.sciencedirect.com/science/article/pii/0191814188900946.

Jones, S. J. and J. W. Glen (1969). "The effect of dissolved impurities on the mechanical properties of ice crystals". In: *Philosophical Magazine* 19.157, pp. 13–24. ISSN: 00318086. DOI: 10.1080/14786436908217758.

Joughin, Ian, Laurence Gray, Robert Bindschadler, Stephen Price, David Morse, Christina Hulbe, Karim Mattar, and Charles Werner (1999). "Tributaries of West Antarctic Ice Streams Revealed by RADARSAT Interferometry". In: *Science* 286.5438, 283 LP –286. DOI: 10.1126/science.286.5438.283. URL: http://science.sciencemag.org/content/286/5438/283.abstract.

Joughin, Ian, Eric Rignot, Christine E. Rosanova, Baerbel K. Lucchitta, and Jennifer Bohlander (2003). "Timing of recent accelerations of Pine Island Glacier, Antarctica". In: *Geophysical Research Letters* 30.13, pp. 28–31. ISSN: 00948276. DOI: 10.1029/2003GL017609.

Joughin, Ian, Ben E. Smith, Ian M. Howat, Ted Scambos, and Twila Moon (2010). "Greenland flow variability from ice-sheet-wide velocity mapping". In: *Journal of Glaciology* 56.197, pp. 415–430. ISSN: 0022-1430. DOI: 10.3189/002214310792447734. URL: https://www.cambridge.org/core/product/identifier/S0022143000207065/type/journal_article.

Joughin, Ian, Ben E. Smith, and Ian M. Howat (2017). "A complete map of Greenland ice velocity derived from satellite data collected over 20 years". In: *Journal of Glaciology* 64.243, pp. 1–11. ISSN: 00221430. DOI: 10.1017/jog.2017.73.

Kamb, Barclay (1959). "Ice petrofabric observations from Blue Glacier, Washington, in relation to theory and experiment". In: *Journal of Geophysical Research* 64.11, pp. 1891–1909. DOI: 10.1029/JZ064i011p01891. URL: https://agupubs.onlinelibrary.wiley.com/doi/abs/10.1029/JZ064i011p01891.

— (1972). "Experimental Recrystallization of Ice Under Stress". In: *Flow and Fracture of Rocks, American Geophysical Union Geophysical Monograph* 16, pp. 211–241. DOI: 10.1029/GM016p0211.

Krischke, Anja, Ulrich Oechsner, and Sepp Kipfstuhl (2015). "Rapid Microstructure Analysis of Polar Ice Cores". In: *Optik & Photonik* 10.2, pp. 32–35. ISSN: 18631460. DOI: 10.1002/opph.201500016. URL: http://doi.wiley.com/10.1002/opph.201500016.

Langway, C. C., H. Oeschger, W. Dansgaard, and American Geophysical Union (1985). "Greenland Ice Core: Geophysics, Geochemistry, and the Environment". In: Geophysical monograph Bd. 33. Washington DC.: American Geophysical Union, pp. 22–31. ISBN: 9780875900575. URL: https://books.google.de/books?id=4QJ2HkvFxIUC.

Law, R. D. (1986). "Relationships between strain and quartz crystallographic fabrics in the Roche Maurice quartzites of Plougastel, western Brittany". In: *Journal of Structural Geology* 8.5, pp. 493–515.

Law, R. D., M. Casey, and R. J. Knipe (1986). "Kinematic and tectonic significance of microstructures and crystallographic fabrics within quartz mylonites from the Assynt and Eriboll regions of the Moine thrust zone, NW Scotland". In: *Transactions of the Royal Society of Edinburgh: Earth Sciences* 77.2, pp. 99–125. ISSN: 14737116. DOI: 10.1017/S0263593300010774.

Lister, G. S. (1974). "The theory of deformation fabrics". PhD thesis. Australian National University.

Lister, G. S. and U. F. Dornsiepen (1982). "Fabric transitions in the Saxony granulite terrain". In: *Journal of Structural Geology* 4.1, pp. 81–92. ISSN: 01918141. DOI: 10.1016/0191-8141(82)90009-8.

Lister, G. S. and B. E. Hobbs (1980). "The simulation of fabric development during plastic deformation and its application to quartzite : the influence of detormation history". In: *Journal of Structural Geology* 2.3, pp. 355–370.

Lister, G. S. and P. F. Williams (1979). "Fabric development in shear zones: theoretical controls and observed phenomena". In: *Journal of Structural Geology* 1.4, pp. 283–297. ISSN: 01918141. DOI: 10.1016/0191-8141(79)90003-8.

Lister, G. S., M. S. Paterson, and B. E. Hobbs (1978). "The simulation of fabric development in plastic deformation and its application to quartzite: the model". In: *Tectonophysics* 45, pp. 107–158.

Llorens, Maria Gema, Albert Griera, Florian Steinbach, Paul D. Bons, Enrique Gomez-Rivas, Daniela Jansen, Jens Roessiger, Ricardo A. Lebensohn, and Ilka Weikusat (2016). "Dynamic recrystallization during deformation of polycrystalline ice: Insights from numerical simulations". In: *Philosophical Transactions of the Royal Society A: Mathematical, Physical and Engineering Sciences* 375.2086. ISSN: 1364503X. DOI: 10.1098/rsta.2015.0346.

Margold, Martin, Chris R. Stokes, and Chris D. Clark (2015). "Ice streams in the Laurentide Ice Sheet: Identification, characteristics and comparison to modern ice sheets". In: *Earth-Science Reviews* 143, pp. 117–146. ISSN: 00128252. DOI: 10.1016/j.earscirev.2015.01.011. URL: http://dx.doi.org/10.1016/j.earscirev.2015.01.011.

Monroe, James S. (2009). *The Changing Earth Exploring Geology and Evolution*. ISBN: 9780495554806. DOI: 10.1017/CBO9781107415324.004.

Montagnat, M., N. Azuma, D. Dahl-Jensen, J. Eichler, S. Fujita, F. Gillet-Chaulet, S. Kipfstuhl, D. Samyn, A. Svensson, and I. Weikusat (2014). "Fabric along the NEEM ice core, Greenland, and its comparison with GRIP and NGRIP ice cores". In: *Cryosphere* 8.4, pp. 1129–1138. ISSN: 19940424. DOI: 10.5194/tc-8-1129-2014.

Neff, Peter D. (2014). "A review of the brittle ice zone in polar ice cores". In: *Annals of Glaciology* 55.68, pp. 72–82. ISSN: 02603055. DOI: 10.3189/2014AoG68A023.

Nick, Faezeh M., Andreas Vieli, Morten Langer Andersen, Ian Joughin, Antony Payne, Tamsin L. Edwards, Frank Pattyn, and Roderik S.W. Van De Wal (2013). "Future sea-level rise from Greenland's main outlet glaciers in a warming climate". In: *Nature* 497.7448, pp. 235–238. ISSN: 00280836. DOI: 10.1038/nature12068. URL: http://dx.doi.org/10.1038/nature12068.

Nye, J. F. (1953). "The Flow Law of Ice from Measurements in Glacier Tunnels, Laboratory Experiments and the Jungfraufirn Borehole Experiment". In: *Proceedings of the Royal Society of London. Series A, Mathematical and Physical Sciences* 219.1139, pp. 477–489. ISSN: 00804630. URL: http://www.jstor.org/stable/99248.

Passchier, Cees W. and Rudolph A. J. Trouw (2005). *Microtectonics*. 2nd ed. Berlin/Heidelberg: Springer-Verlag. ISBN: 3-540-64003-7. DOI: 10.1007/3-540-29359-0. URL: http://link.springer.com/10.1007/3-540-29359-0.

Paterson, W. S. B. (1994). *The physics of glaciers*. Pergamon, p. 480. ISBN: 0080379451.

Payne, Antony (1999). "A thermomechanical model of ice flow in West Antarctica". In: *Climate Dynamics* 15.2, pp. 115–125. DOI: https://doi.org/10.1007/s003820050.

Perutz, M. F. and G. Seligman (1939). "A crystallographic investigation of glacier structure and the mechanism of glacier flow". In: *Proceedings of ntheRoyal Society of London. Series A, Mathematical and Physical Sciences* 172.1, pp. 335–369. ISSN: 1364-5021. DOI: 10.1098/rspa.1939.0108. URL: http://www.jstor.org/stable/10.2307/97323.

Petersen, Sandra (2016). *EastGrip - The East Greenland Ice-core Project*. URL: https://eastgrip.org/.

Petrenko, Victor F. and Robert W. Whitworth (1999). *Physics of ice*. London: Clarendon Press. ISBN: 9780198518952.

R Core Team (2014). *R: A Language and Environment for Statistical Computing*. Vienna, Austria.

Ramsay, John G. and Martin I. Huber (1984). *The techniques of modern structural geology. Volume 1, Strain analysis*. London: Academic Press. ISBN: 0125769016.

Richard, Jones and P.W. Geoff Tanner (1995). "Strain partitioning in transpression zones". In: *Journal of Structural Geology* 17.6, pp. 793–802. ISSN: 0191-8141. DOI: 10.1016/0191-8141(94)00102-6. URL: https://www.sciencedirect.com/science/article/pii/0191814194001026?via%3Dihub.

Rignot, E., J. Mouginot, and B. Scheuchl (2011). "Ice Flow of the Antarctic Ice Sheet". In: *Science* 333.6048, 1427 LP –1430. DOI: 10.1126/science.1208336. URL: http://science.sciencemag.org/content/333/6048/1427.abstract.

Ruth, U. et al. (2007). ""EDML1": A chronology for the EPICA deep ice core from Dronning Maud Land, Antarctica, over the last 150 000 years". In: *Climate of the Past* 3.3, pp. 475–484. ISSN: 18149332. DOI: 10.5194/cp-3-475-2007.

Schmid, Stefan and M Casey (1986). *Complete fabric analysis of some commonly observed quartz C-axis patterns*. 36, pp. 263–286. ISBN: 0875900623. DOI: 10.1029/GM036p0263. URL: http://www.agu.org/books/gm/v036/GM036p0263/GM036p0263.shtml.

Schulson, Erland M. and Paul Duval (2009). *Creep and fracture of ice*. ISBN: 9780511581397. DOI: 10.1017/CBO9780511581397.

Seligman, Gerald (1941). "The Structure of a Temperate Glacier". In: *The Geographical Journal* 97.5, pp. 295–315.

Staroszczyk, Ryszard (2011). "A uniform stress, multi-grain model for migration recrystallization in polar ice". In: *Acta Geophysica* 59.5, pp. 833–857. ISSN: 18956572. DOI: 10.2478/s11600-011-0026-0.

Steinbach, Florian, Ernst-Jan N. Kuiper, Jan Eichler, Paul D. Bons, Martyn R. Drury, Albert Griera, Gill M. Pennock, and Ilka Weikusat (2017). "The Relevance of Grain Dissection for Grain Size Reduction in Polar Ice: Insights from Numerical Models and Ice Core Microstructure Analysis". In: *Frontiers in Earth Science* 5.September. ISSN: 2296-6463. DOI: 10.3389/feart.2017.00066. URL: http://journal.frontiersin.org/article/10.3389/feart.2017.00066/full.

Stokes, C. R., M. Margold, C. D. Clark, and L. Tarasov (2016). "Ice stream activity scaled to ice sheet volume during Laurentide Ice Sheet deglaciation". In: *Nature* 530.7590, pp. 322–326. ISSN: 14764687. DOI: 10.1038/nature16947. URL: http://dx.doi.org/10.1038/nature16947.

Teyssier, Christian, Basil Tikoff, and Michelle Markley (1995). "Oblique plate motion and continental tectonics". In: *Geology* 23.5, pp. 447–450. ISSN: 0091-7613. URL: http://dx.doi.org/10.1130/0091-7613(1995)023%3C0447:OPMACT%3E2.3.COhttp://0.0.0.2.

Thorsteinsson, Thorsteinn (1996). "Textures and fabrics in the GRIP ice core, in relation to climate history and ice deformation". In: 205.1 996, p. 150.

Thorsteinsson, Thorsteinn, Josef Kipfstuhl, and Heinz Miller (1997). "Textures and fabrics in the GRIP ice core". In: *Journal of Geophysical Research: Oceans* 102.C12, pp. 26583–26599. ISSN: 21699291. DOI: 10.1029/97JC00161.

Tullis, Jan and Richard A Yund (1977). "Experimental deformation of dry westerly granite". In: *Journal of Geophysical Research* 82.36, pp. 5705–5718. DOI: 10.1029/JB082i036p05705. URL: https://agupubs.onlinelibrary.wiley.com/doi/abs/10.1029/JB082i036p05705.

Tullis, Jan, John M. Christie, and David T. Griggs (1973). "Microstructures and Preferred Orientations of Experimentally Deformed Quartzites". In: *GSA Bulletin* 84.1, pp. 297–314. ISSN: 0016-7606. URL: http://dx.doi.org/10.1130/0016-7606(1973)84%3C297:MAPOOE%3E2.0.COhttp://0.0.0.2.

Urai, J. L., W. D. Means, and G. S. Lister (1986). "Dynamic recrystallization of minerals". In: January, pp. 161–199. ISSN: 1118664353. DOI: 10.1029/GM036p0161. URL: http://www.agu.org/books/gm/v036/GM036p0161/GM036p0161.shtml.

Vallelonga, P. et al. (2014). "Initial results from geophysical surveys and shallow coring of the Northeast Greenland Ice Stream (NEGIS)". In: *Cryosphere* 8.4, pp. 1275–1287. ISSN: 19940424. DOI: 10.5194/tc-8-1275-2014.

Vernooji, Martine G.C. (2005). "Dynamic Recrystallisation and Microfrabric Development in Single Crystals of Quartz during Experimental Deformation". PhD thesis. Utrecht, p. 3.

Wallbrecher, Eckard (1986). *Tektonische und gefügeanalytische Arbeitsweisen: graphische, rechnerische und statistische Verfahren.* Stuttgart: Enke, 244 pp.

Wang, Yun, Thorsteinn Thorsteinsson, Josef Kipfstuhl, Heinz Miller, Dorthe Dahl-Jensen, and Hitoshi Shoji (2002). "A vertical girdle fabric in the NorthGRIP deep ice core, North Greenland". In: *Annals of Glaciology* 35, pp. 515–520. ISSN: 02603055. DOI: 10.3189/172756402781817301.

Weertman, Johannes and Julia R. Weertman (1992). *Elementary Dislocation Theory*. Oxford: Oxford University Press, p. 228. ISBN: 9780195069006.

Weikusat, Ilka, Sepp Kipfstuhl, Sérgio H Faria, Nobuhiko Azuma, and Atsushi Miyamoto (2009a). *Mean grain size of ice core EDML*. DOI: 10.1594/PANGAEA.807132. URL: https://doi.org/10.1594/PANGAEA.807132.

Weikusat, Ilka, Sepp Kipfstuhl, Sérgio H. Faria, Nobuhiko Azuma, and Atsushi Miyamoto (2009b). "Subgrain boundaries and related microstructural features in EDML (Antarctica) deep ice core". In: *Journal of Glaciology* 55.191, pp. 461–472. ISSN: 00221430. DOI: 10.3189/002214309788816614.

Weikusat, Ilka et al. (2017). "Physical analysis of an Antarctic ice core—towards an integration of micro- and macrodynamics of polar ice". In: *Philosophical Transactions of the Royal Society A: Mathematical, Physical and Engineering Sciences* 375.2086, p. 20150347. ISSN: 1364-503X. DOI: 10.1098/rsta.2015.0347. URL: http://rsta.royalsocietypublishing.org/lookup/doi/10.1098/rsta.2015.0347.

Wilson, C. J. L. (1981). "Experimental folding and fabric development in multilayered ice". In: *Tectonophysics* 78, pp. 139–159. ISSN: 00401951. DOI: 10.1016/0040-1951(81)90011-1.

— (1983). "Foliation and strain development in ice-mica models". In: *Tectonophysics* 92, pp. 93–122. ISSN: 00401951. DOI: 10.1016/0040-1951(83)90086-0.

Wilson, Christopher, Mark Peternell, S Piazolo, and Vladimir Luzin (2014). "Microstructure and fabric development in ice: Lessons learned from in situ experiments and implications for understanding rock evolution". In: *Journal of Structural Geology* 61, 50–77. DOI: 10.1016/j.jsg.2013.05.006.

Wilson, Christopher J.L., David S. Russell-Head, and Hadi M. Sim (2003). "The application of an automated fabric analyzer system to the textural evolution of folded ice layers in shear zones". In: *Annals of Glaciology* 37.1996, pp. 7–17. ISSN: 02603055. DOI: 10.3189/172756403781815401.

Woodcock, N. H. (1977). "Specification of fabric shapes using an eigenvalue method". In: *Geological Society of America Bulletin* 88, pp. 1231–1236.

# A Appendix

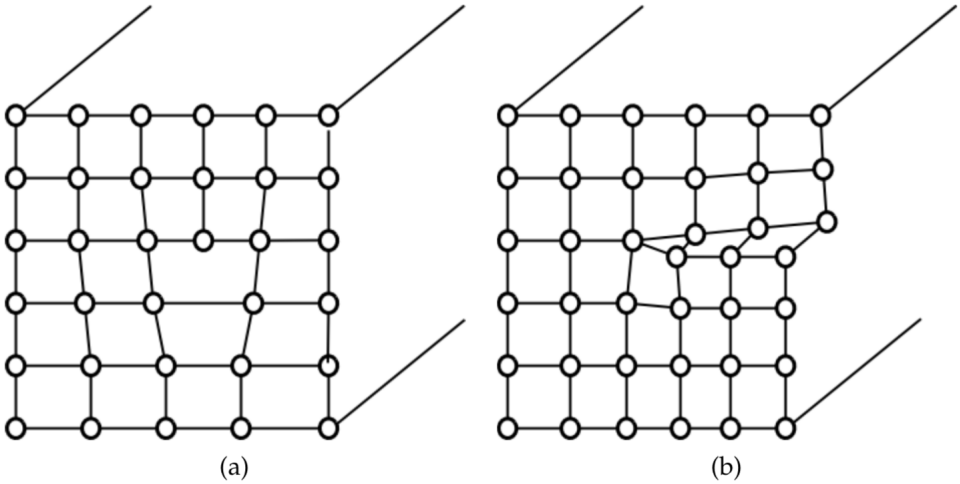


FIGURE A.1: a) Edge and b) screw dislocation. From Eichler (2013).

FIGURE A.2: Partly processed thick and thin sections

The thin section on the left will be polished and then analysed by the Fabric Analyser. On the right, thick sections with already polished surfaces were glued to the glass plates.

FIGURE A.3: Core buffer in the science trench

Freshly drilled ice cores are stored here. Photo by S. H. Faria.

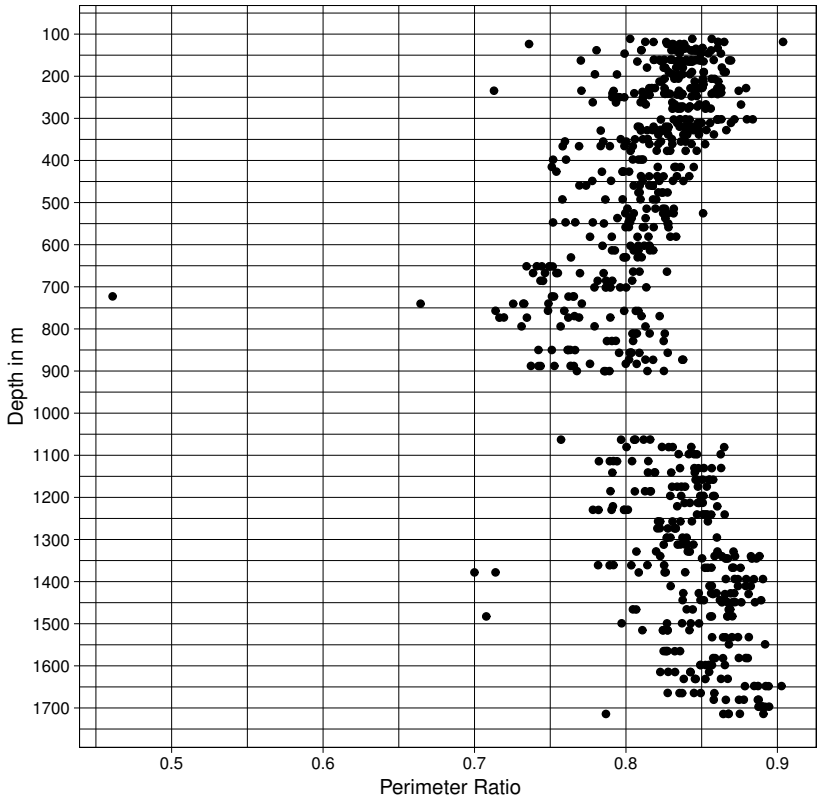


FIGURE A.4: Perimeter ratio with outlier

The smallest perimeter ratio was measured at a depth of 720 m.

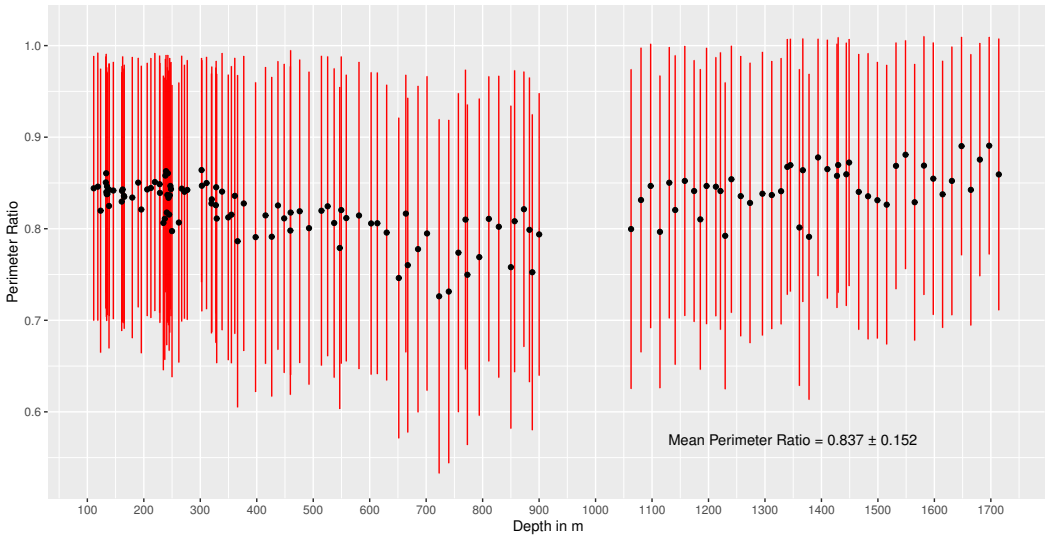


FIGURE A.5: Perimeter ratio with standard deviation at EGRIP, displayed are mean values for entire bags (=6 samples).

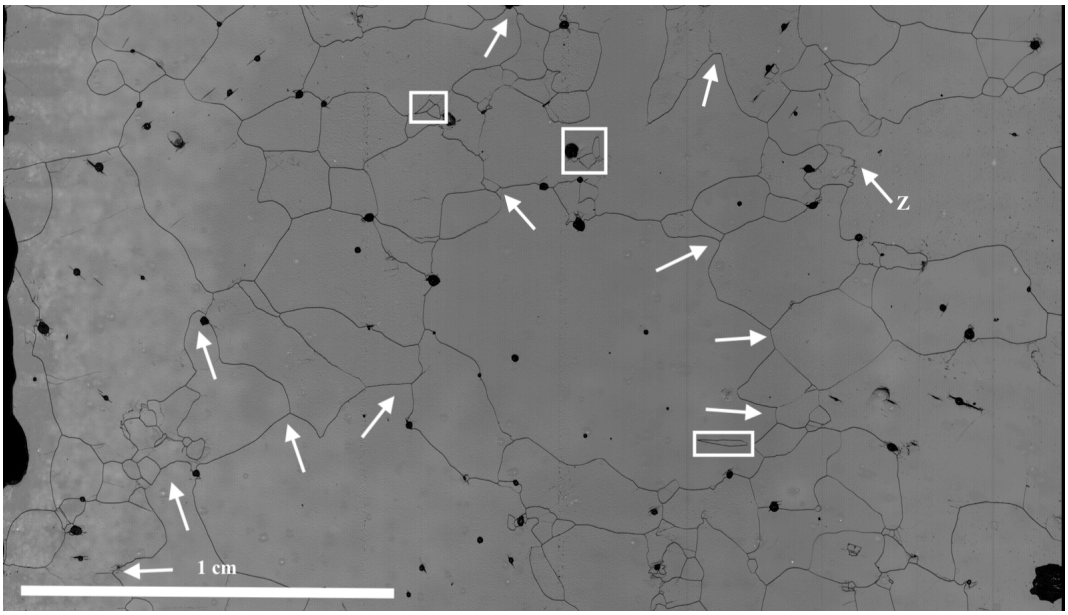


FIGURE A.6: LASM high-resolution image at a depth of 426.75 m, the same annotation as in Figure 3.10 is used.

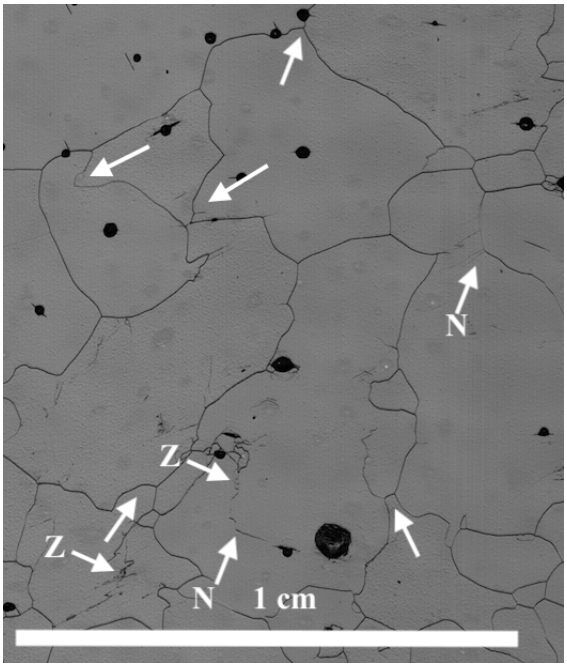


FIGURE A.7: LASM high-resolution image at a depth of 426.75 m, the same annotation as in Figure 3.10 is used.

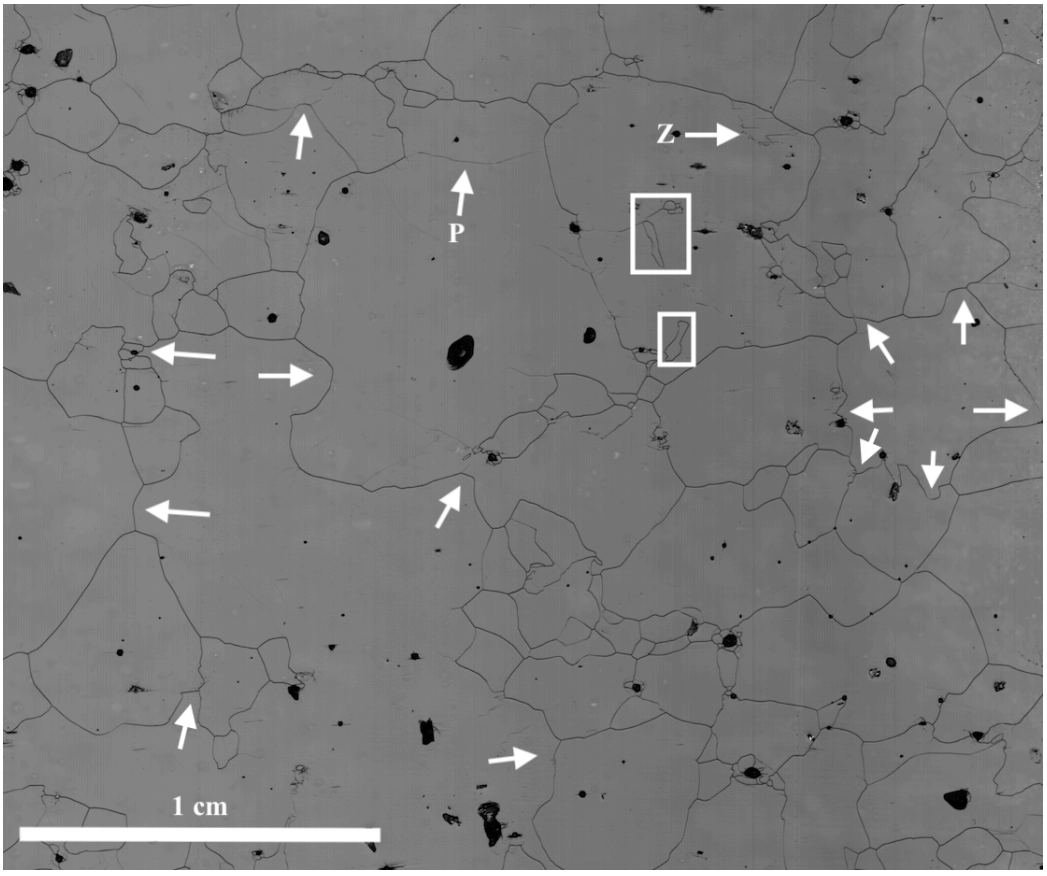


FIGURE A.8: LASM high-resolution image at a depth of 722.75 m, the same annotation as in Figure 3.10 is used.

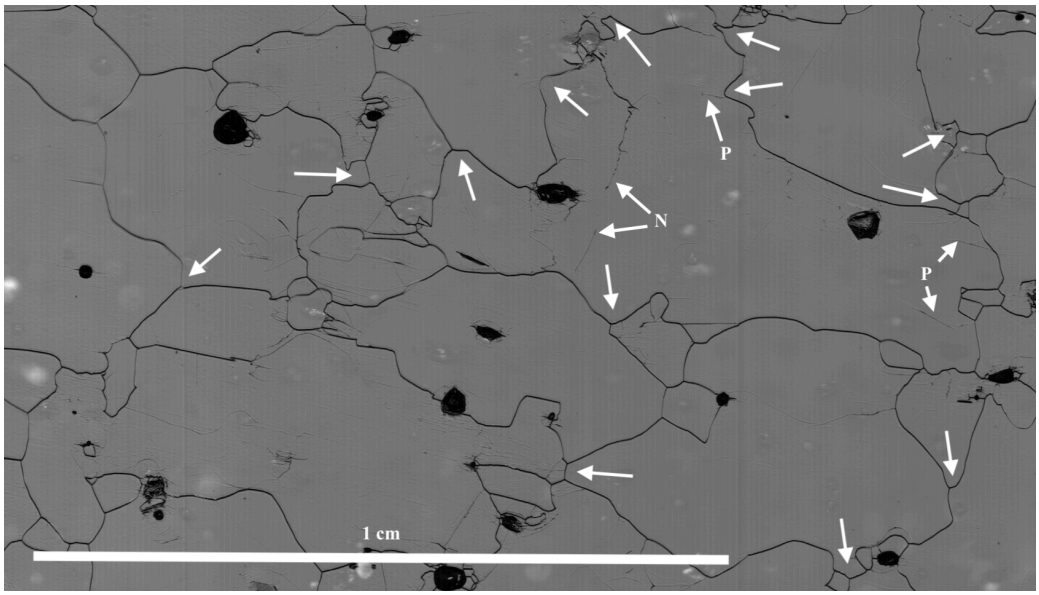


FIGURE A.9: LASM high-resolution image at a depth of 722.84 m, the same annotation as in Figure 3.10 is used.

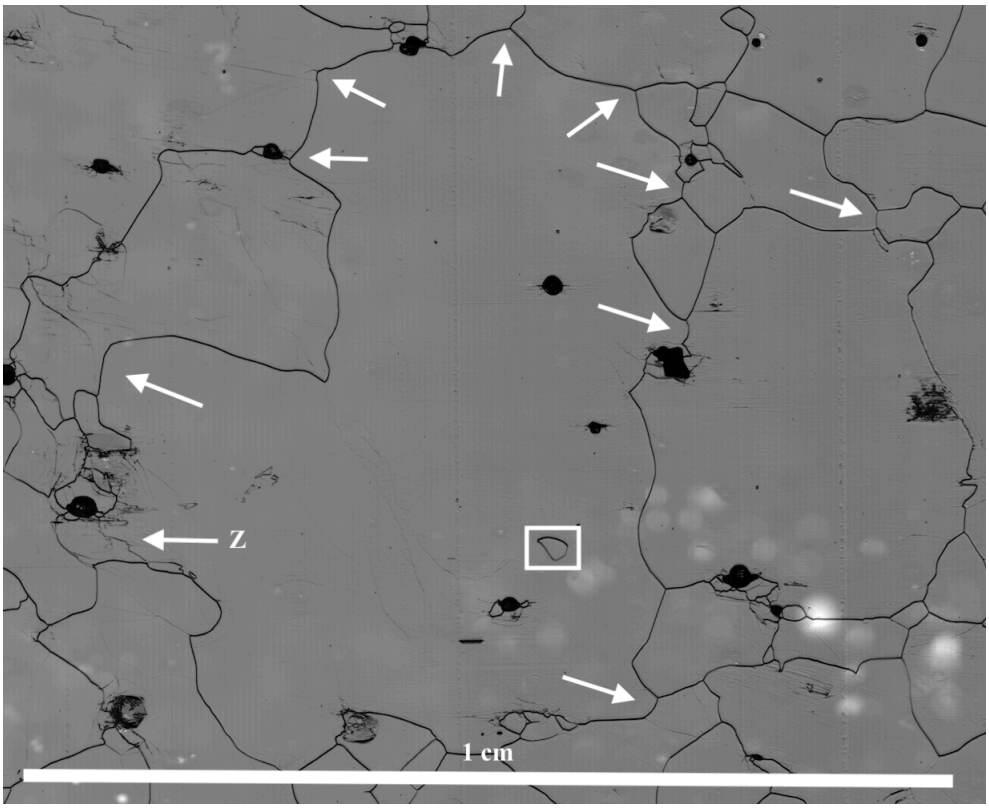


FIGURE A.10: LASM high-resolution image at a depth of 722.93 m, the same annotation as in Figure 3.10 is used.

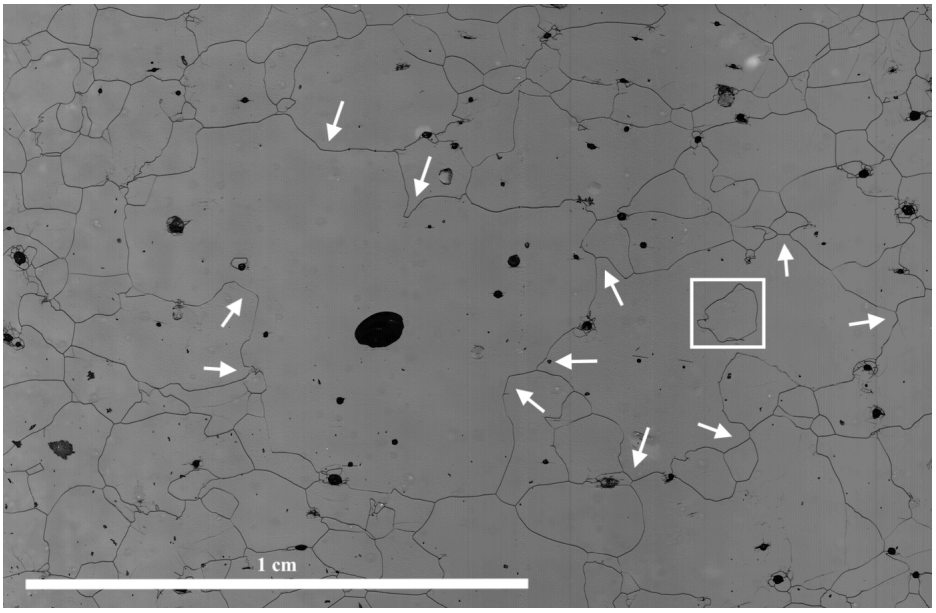


FIGURE A.11: LASM high-resolution image at a depth of 740.07 m, the same annotation as in Figure 3.10 is used.

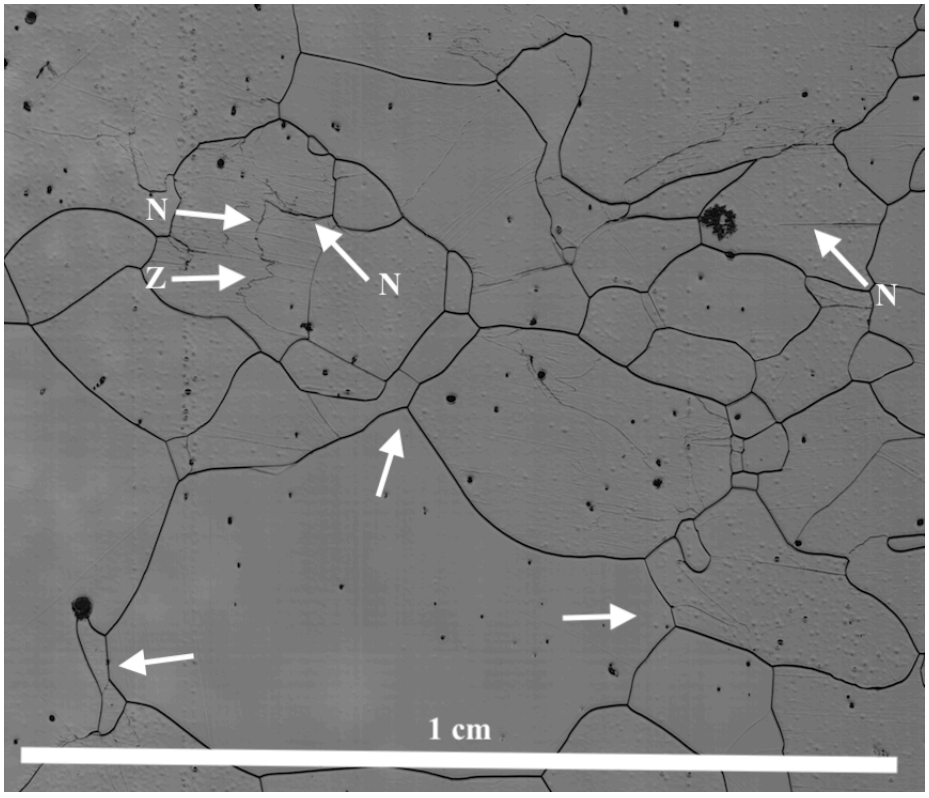


FIGURE A.12: LASM high-resolution image at a depth of 1113.89 m, the same annotation as in Figure 3.10 is used.

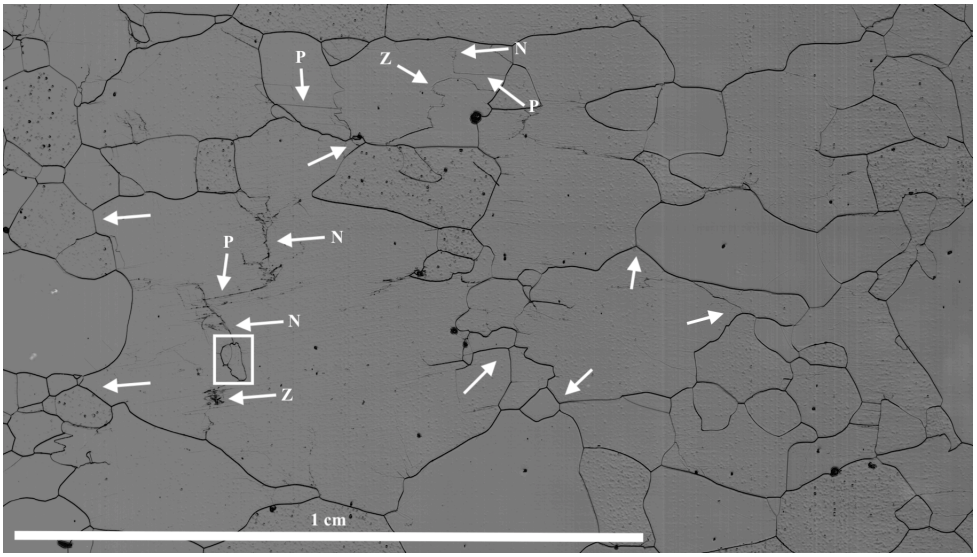


FIGURE A.13: LASM high-resolution image at a depth of 1113.89 m, the same annotation as in Figure 3.10 is used.

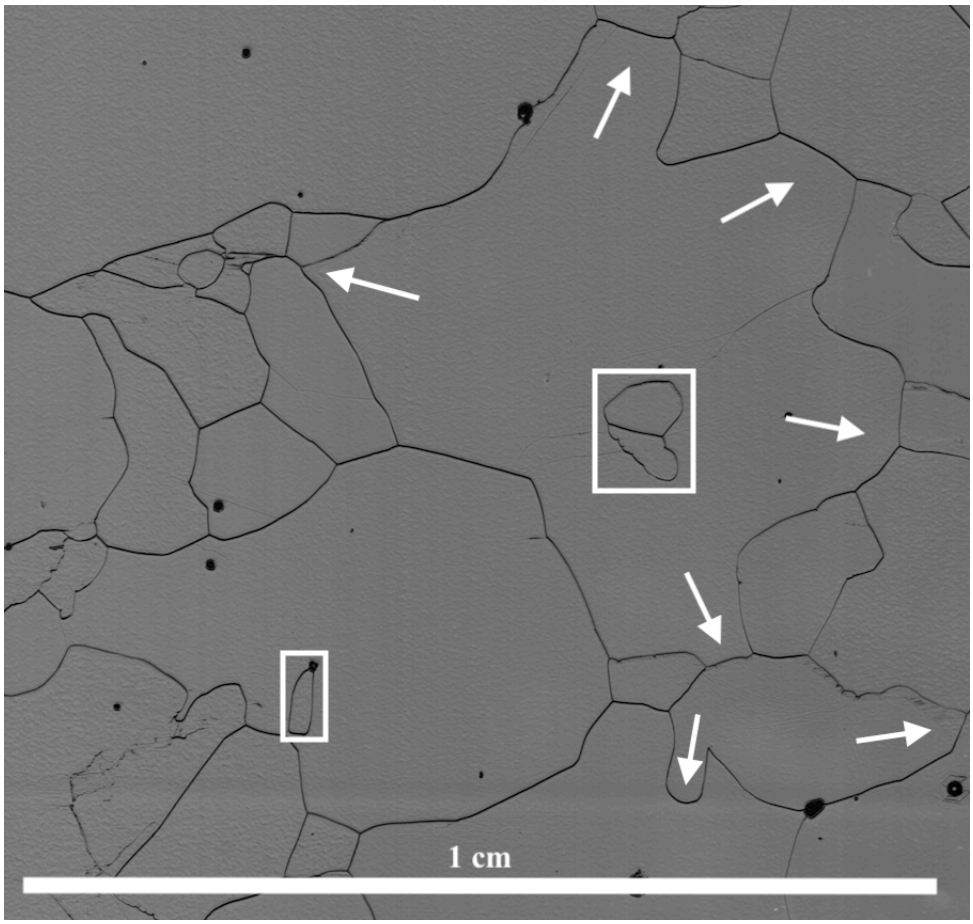


FIGURE A.14: LASM high-resolution image at a depth of 1114.07 m, the same annotation as in Figure 3.10 is used.

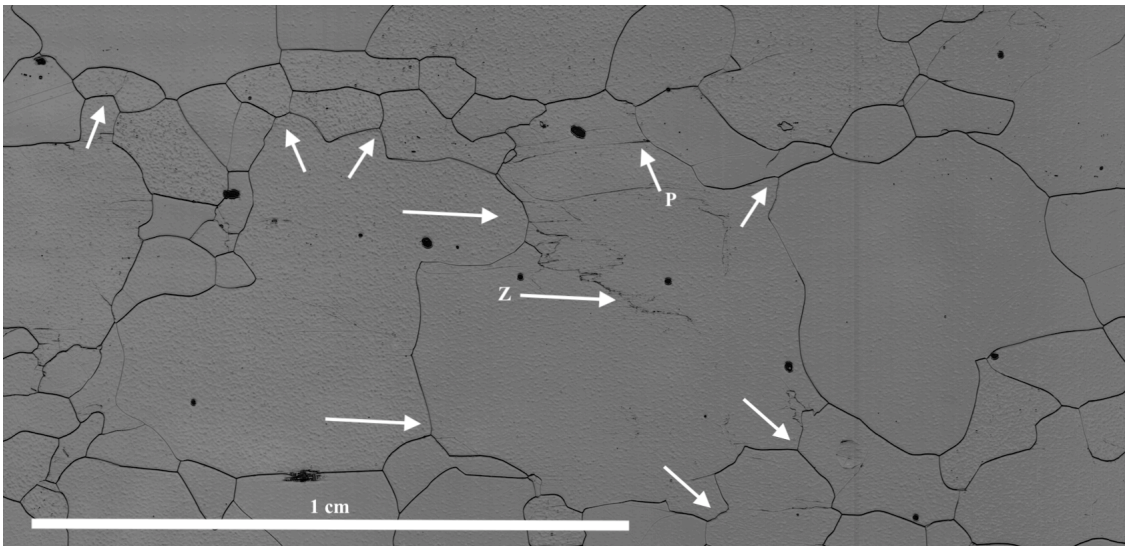


FIGURE A.15: LASM high-resolution image at a depth of 1114.25 m, the same annotation as in Figure 3.10 is used.

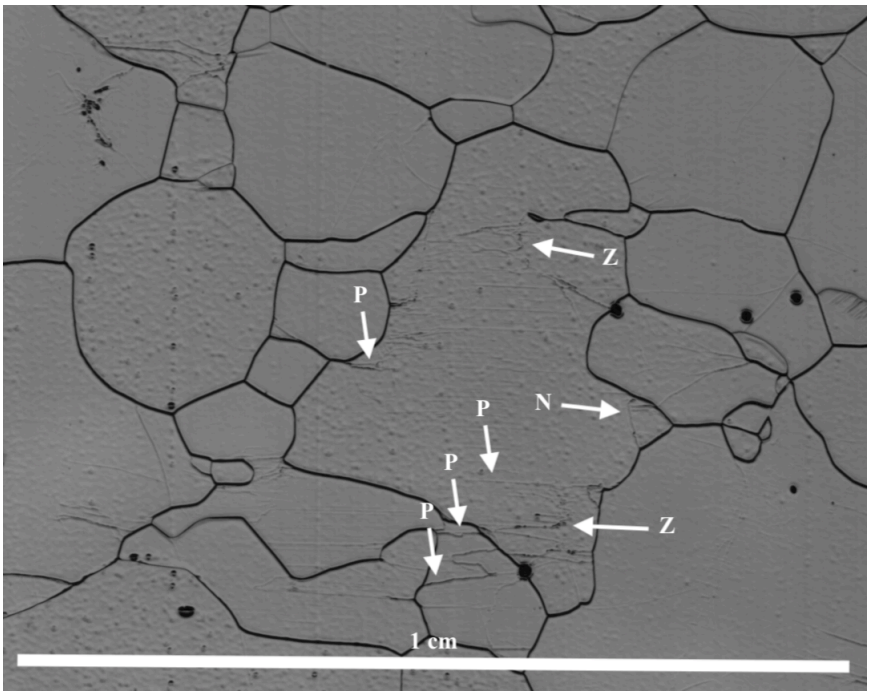


FIGURE A.16: LASM high-resolution image at a depth of 1360.84 m, the same annotation as in Figure 3.10 is used.

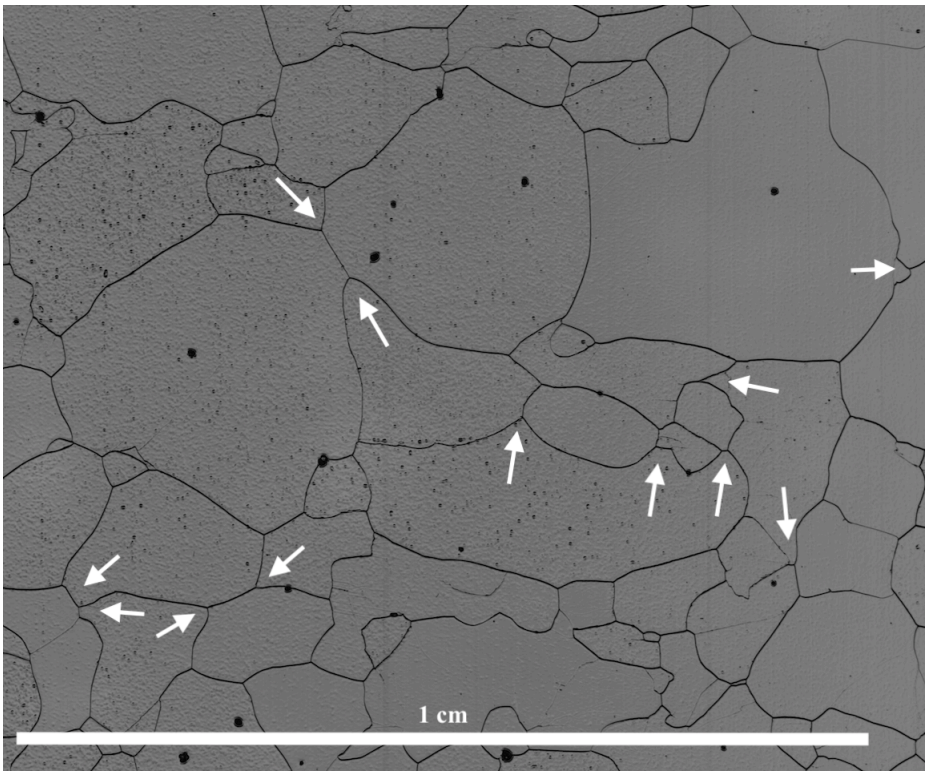


FIGURE A.17: LASM high-resolution image at a depth of 1361.02 m, the same annotation as in Figure 3.10 is used.

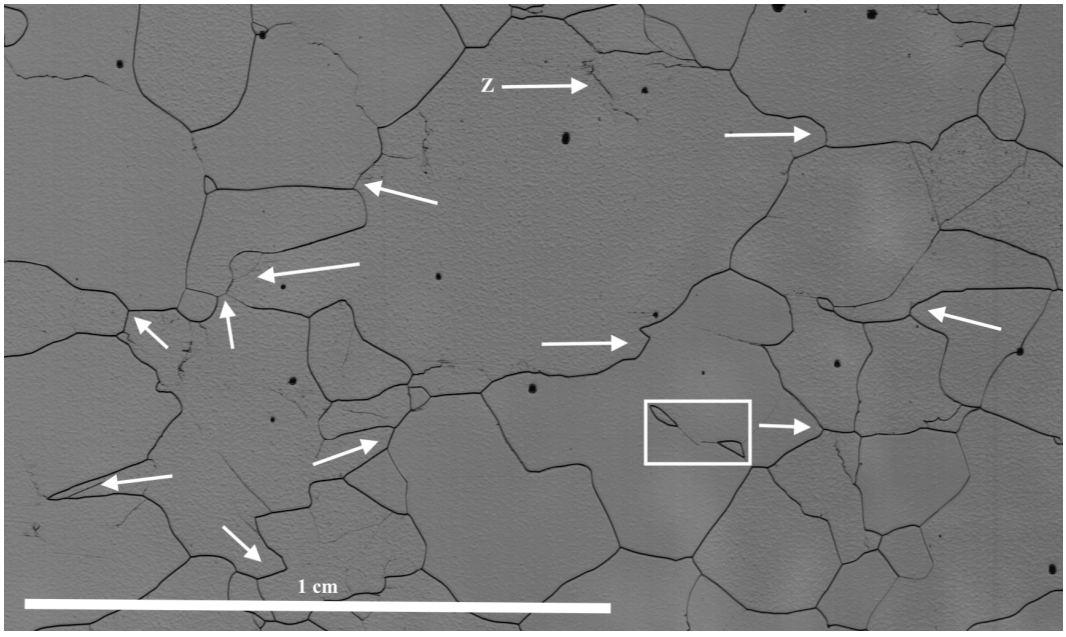


FIGURE A.18: LASM high-resolution image at a depth of 1361.02 m, the same annotation as in Figure 3.10 is used.

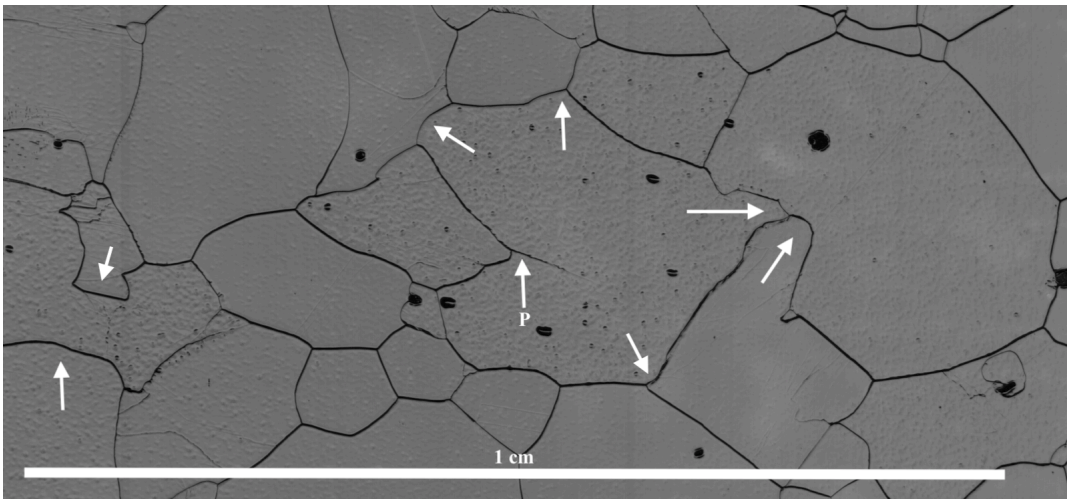


FIGURE A.19: LASM high-resolution image at a depth of 1377.80 m, the same annotation as in Figure 3.10 is used.

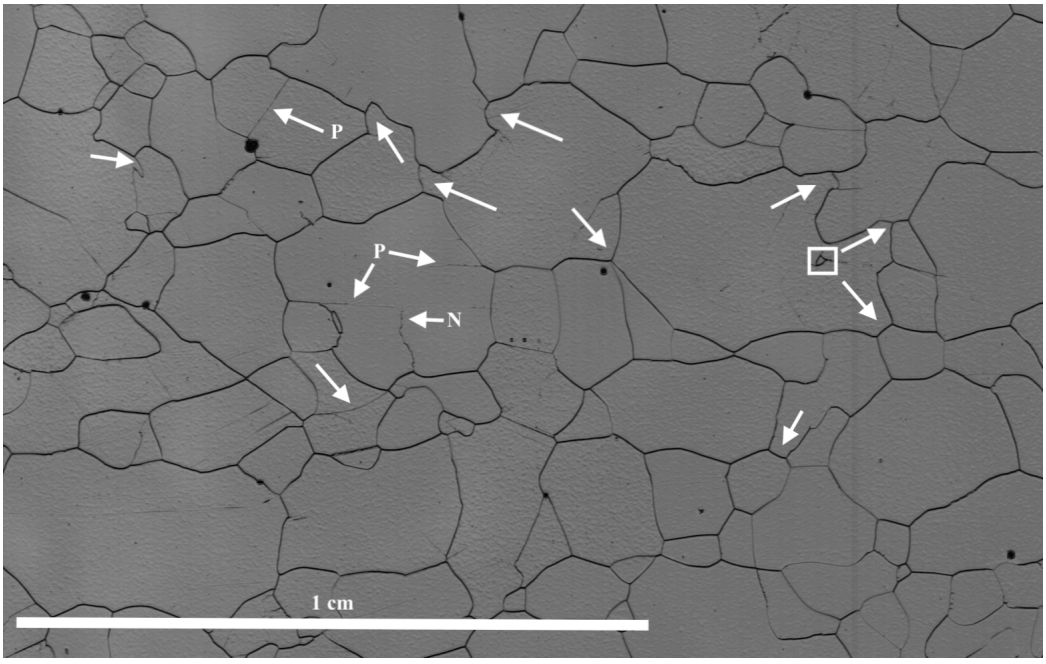


FIGURE A.20: LASM high-resolution image at a depth of 1378.16 m, the same annotation as in Figure 3.10 is used.

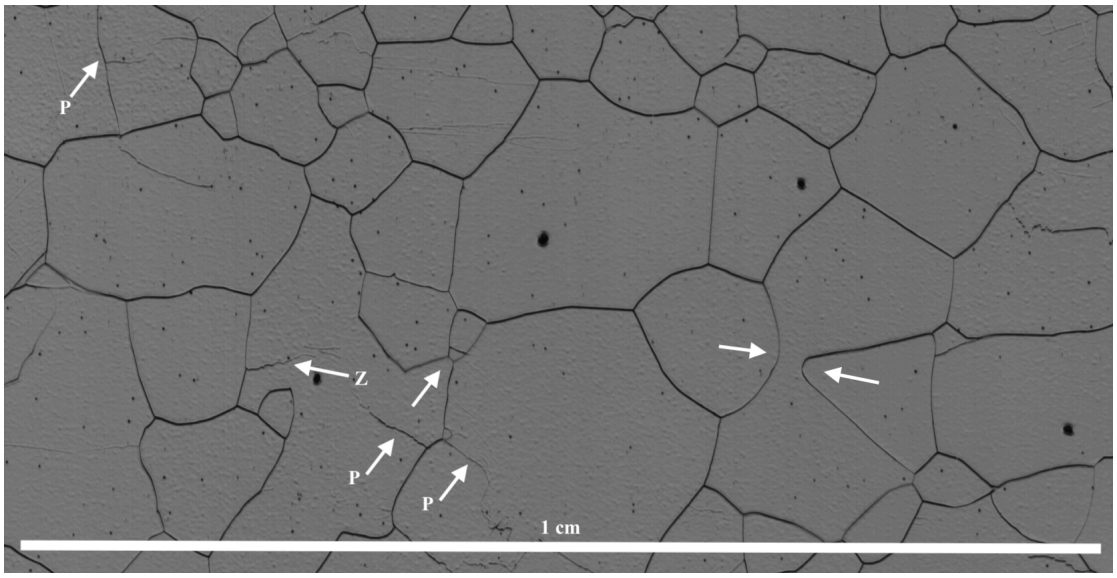


FIGURE A.21: LASM high-resolution image at a depth of 1648.03 m, the same annotation as in Figure 3.10 is used.

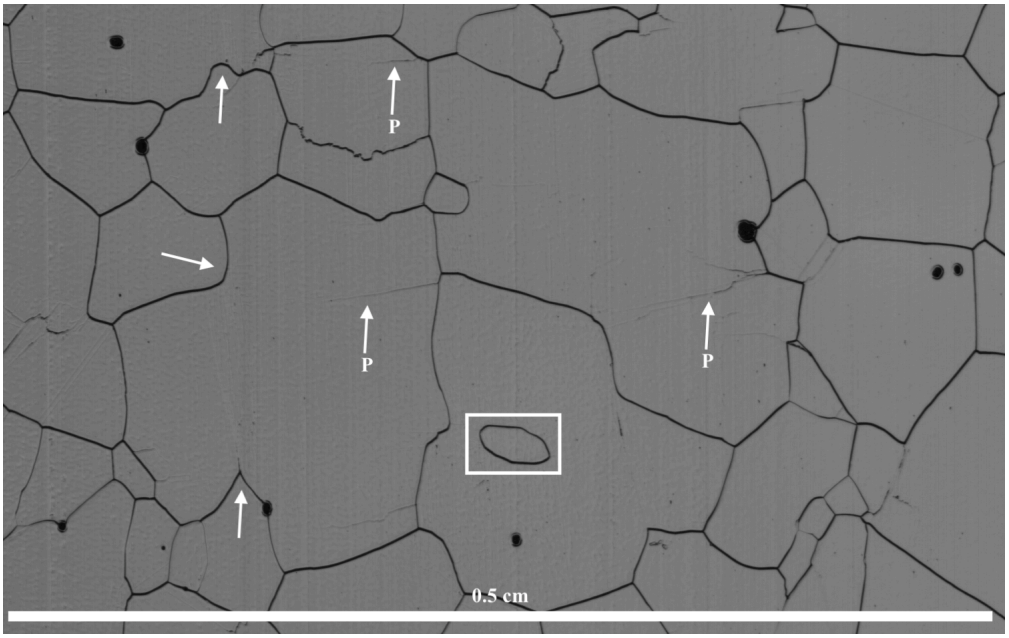


FIGURE A.22: LASM high-resolution image at a depth of 1648.30 m, the same annotation as in Figure 3.10 is used.

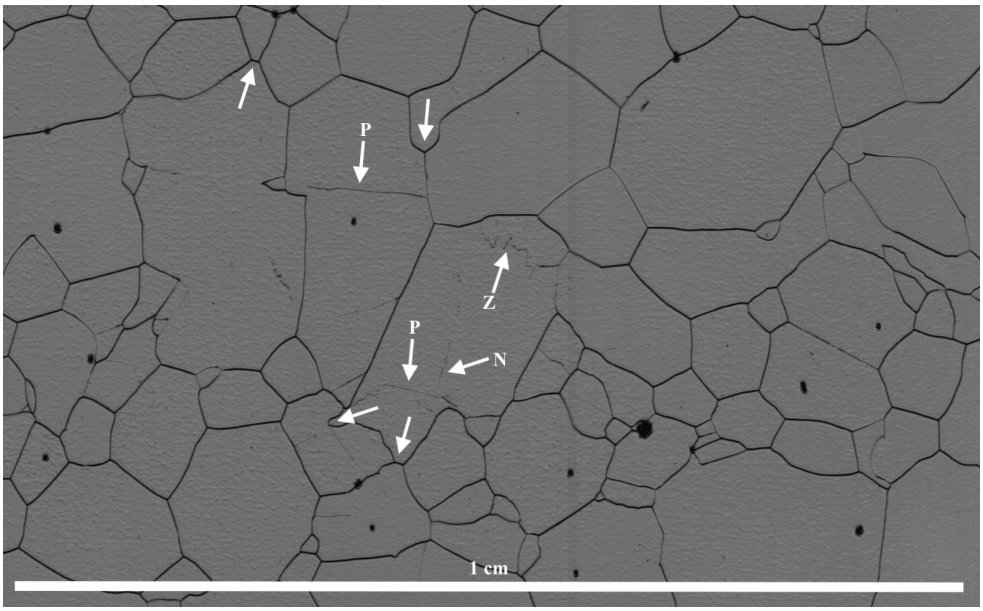


FIGURE A.23: LASM high-resolution image at a depth of 1696.89 m, the same annotation as in Figure 3.10 is used.

# B Appendix

The following pages include stereographic equal-area hemispherical projection of all analysed thin sections. The sample number and depth are displayed, as well as the number of grains per sample. For the lower part of the core, dummy plots were inserted to compensate for incomplete bags, not consisting of six samples.

0203_1
111.19m

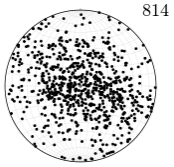


0203_2
111.28m

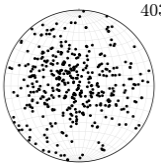


0203_3
111.38m

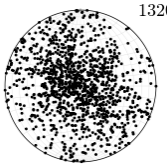


0216_1
118.34m

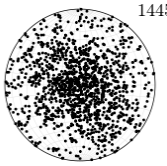


0216_2
118.43m

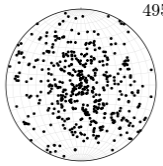


0216_3
118.53m

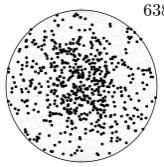


0216_4
118.62m

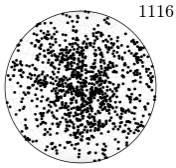


0216_5
118.71m

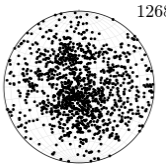


0216_6
118.8m

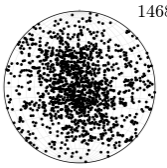


0225_1
123.29m

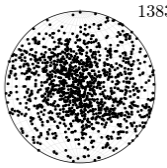


0225_2
123.38m

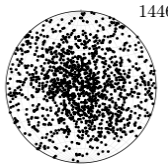


0225_3
123.48m


0225_4
123.57m

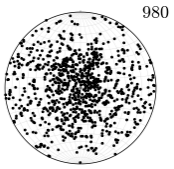


0225_5
123.66m

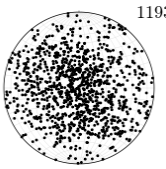


0225_6
123.75m

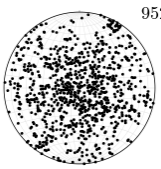


0242_2
132.73m


0243_3
133.38m

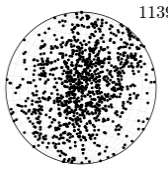


0244_1
133.74m


0245_1
134.29m

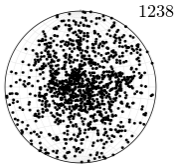


0246_1
134.84m

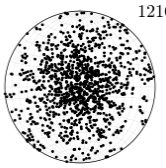


0247_1
135.39m

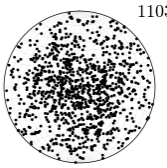


0252_1
138.14m

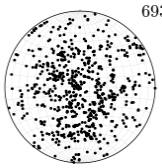


0252_2
138.23m

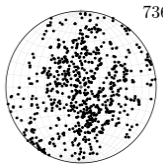


0252_3
138.33m

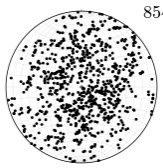


0252_4
138.42m

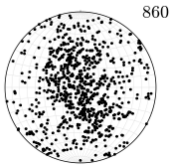


0252_5
138.51m

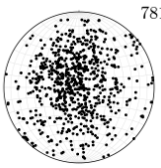


0252_6
138.6m

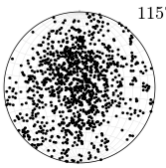


0253_1
138.69m

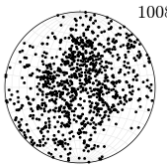


0253_2
138.78m

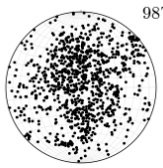


0253_3
138.88m

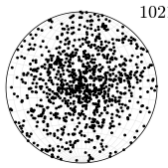

0253_4
138.97m

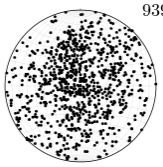


0253_5
139.06m

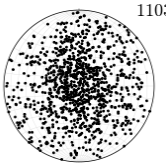


0266_1
145.84m

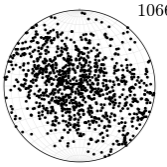


0266_2
145.93m

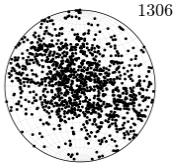


0266_3
146.03m

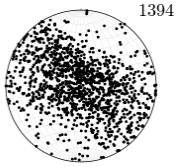


0266_4
146.12m

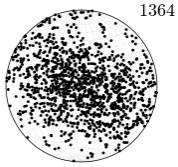


0266_5
146.21m


0266_6
146.3m

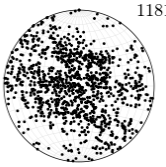


0293_1
160.69m

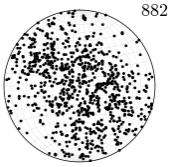


0293_2
160.78m

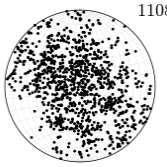


0293_3
160.88m

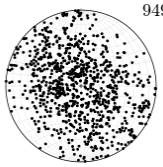


0293_4
160.97m

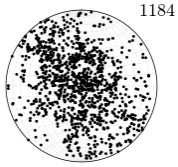


0293_5
161.06m

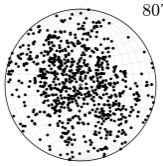


0293_6
161.15m

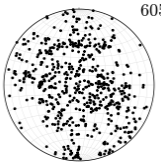


0294_1
161.24m


0294_2
161.33m

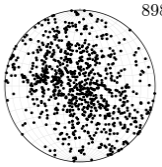


0294_3
161.43m

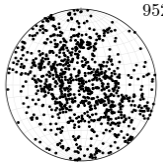


0294_4
161.52m

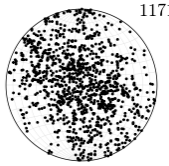


0294_5
161.61m

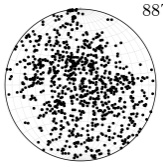


0294_6
161.7m

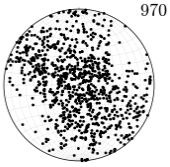


0296_1
162.34m

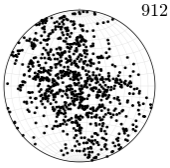


0296_2
162.43m

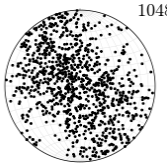


0296_3
162.53m

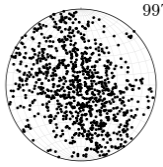


0296_4
162.62m

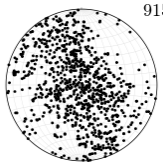


0296_5
162.71m

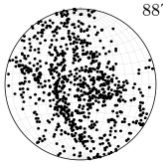


0296_6
162.8m

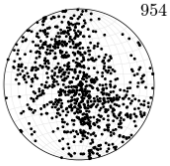


0300_1
164.54m

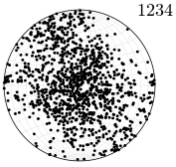


0300_2
164.63m

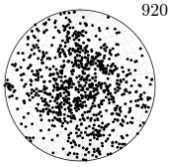


0300_3
164.73m

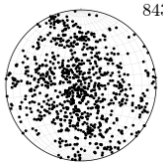


0300_4
164.82m

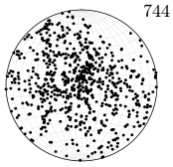

0300_5
164.91m

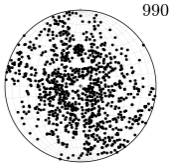


0300_6
165m

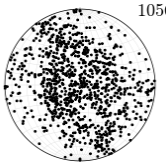


0301_1
165.09m

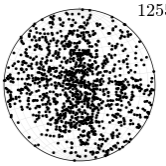


0301_2
165.18m

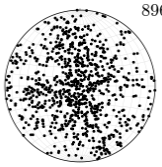


0301_3
165.28m

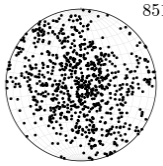


0301_4
165.37m

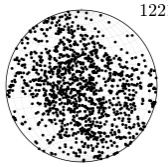


0301_5
165.46m

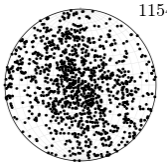


0301_6
165.55m

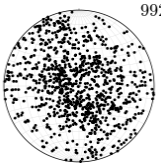


0327_1
179.39m

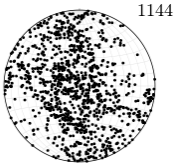


0327_2
179.48m

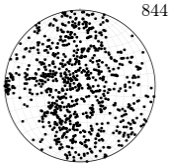


0327_3
179.58m

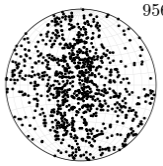


0327_4
179.67m

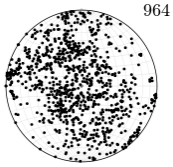


0327_5
179.76m

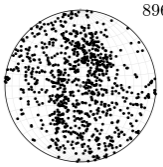


0327_6
179.85m

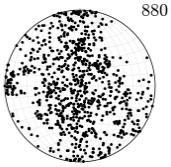


0346_1
189.84m

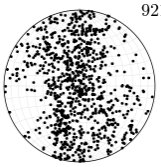


0346_2
189.93m

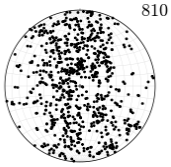


0346_3
190.03m

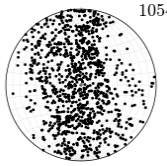


0346_4
190.12m

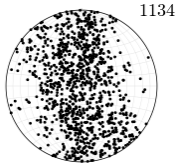


0346_5
190.21m

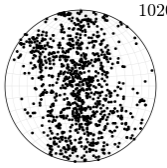


0346_6
190.3m

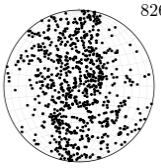


0356_1
195.34m

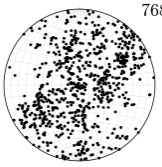


0356_2
195.43m

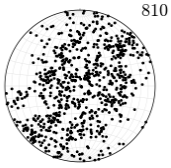


0356_3
195.53m

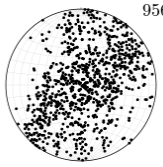


0356_4
195.62m

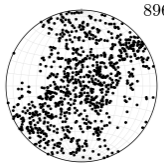


0356_5
195.71m

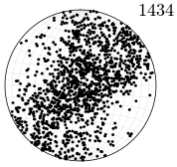


0356_6
195.8m

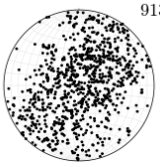


0375_1
205.79m

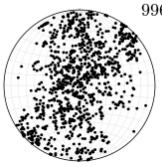


0375_2
205.88m

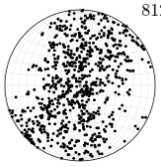


0375_3
205.98m

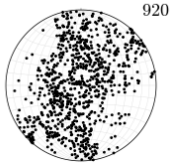


0375_4
206.07m

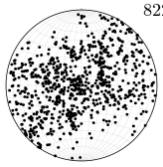

0375_5
206.16m

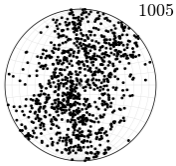


0375_6
206.25m

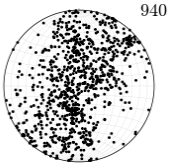


0387_1
212.39m

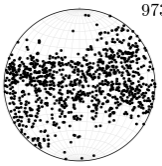


0387_2
212.48m

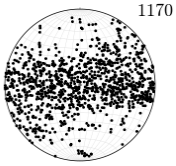


0387_3
212.58m

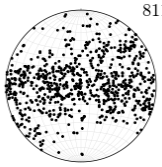


0387_4
212.67m

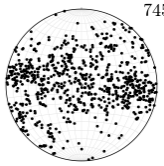


0387_5
212.76m

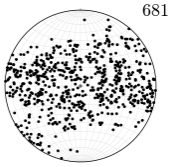


0387_6
212.85m

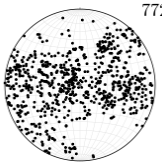


0400_1
219.54m

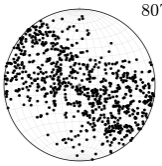


0400_2
219.63m

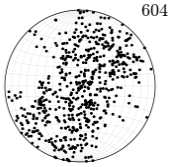


0400_3
219.73m

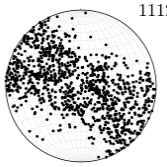


0415_1
227.79m

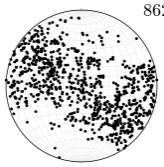


0415_2
227.88m

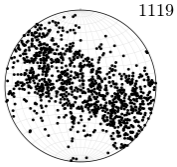


0415_3
227.98m


0415_4
228.07m

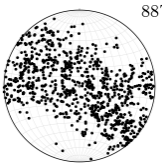


0415_5
228.16m

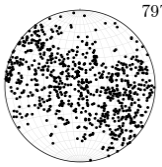


0415_6
228.25m

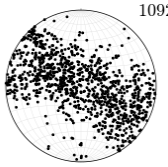


0416_1
228.34m

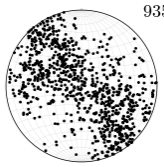


0416_2
228.43m

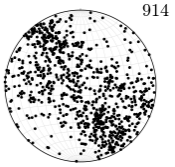


0416_3
228.53m

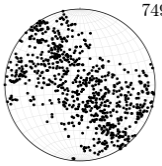


0416_4
228.62m

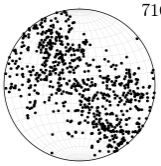


0416_5
228.71m

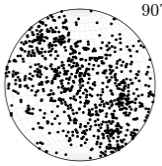


0416_6
228.8m

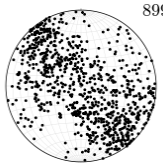


0427_1
234.39m

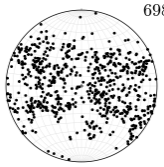


0427_2
234.48m

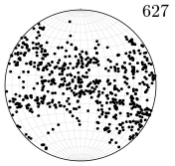


0427_3
234.58m

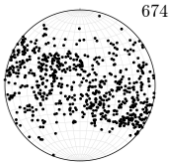


0427_4
234.67m

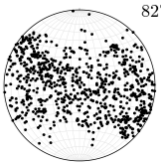


0427_5
234.76m

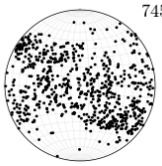


0427_6
234.85m

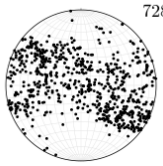


0432_1
237.14m

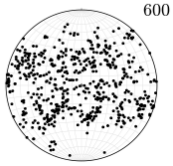

0434_1
238.24m

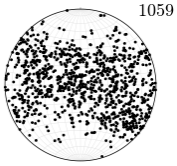


0436_1
239.34m

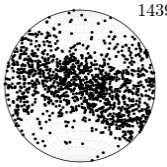


0438_1
240.44m

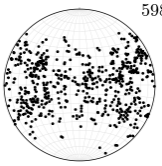


0438_2
240.53m

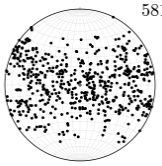


0438_3
240.63m

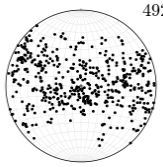


0438_4
240.72m

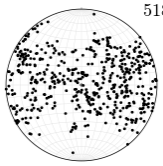


0438_5
240.81m

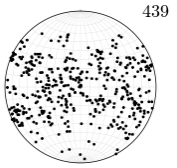


0438_6
240.9m

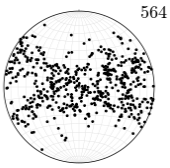


0440_1
241.54m

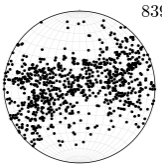


0440_2
241.63m

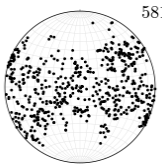


0440_3
241.73m

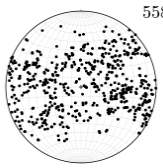


0440_4
241.82m

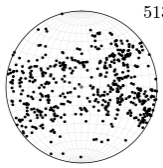


0440_5
241.91m

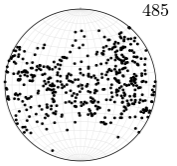


0440_6
242m

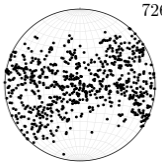


0442_1
242.64m

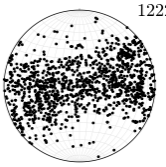


0444_1
243.74m

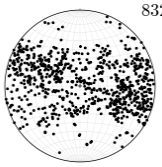


0446_2
244.93m

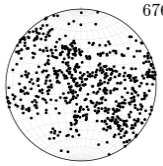


0448_1
245.94m

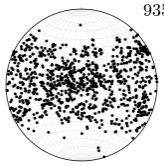


0450_1
247.04m

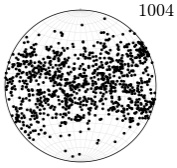


0452_1
248.14m

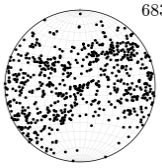


0455_1
249.79m

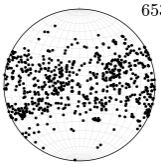


0455_2
249.88m

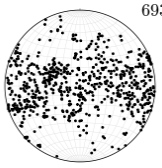


0455_3
249.98m

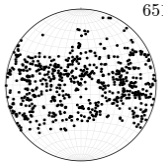


0455_4
250.07m

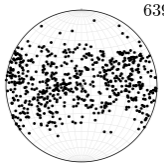


0455_5
250.16m

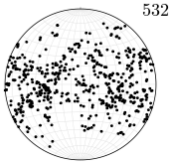


0455_6
250.25m

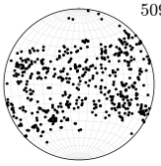


0477_1
261.89m

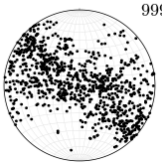


0477_2
261.98m

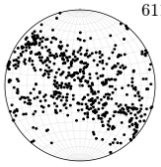


0477_3
262.07m

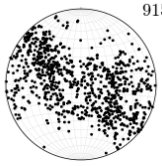


0477_4
262.17m

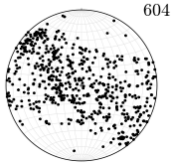

0477_6
262.35m

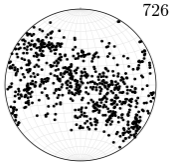


0486_1
266.84m

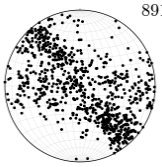


0486_2
266.93m

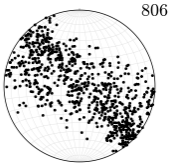


0486_3
267.02m

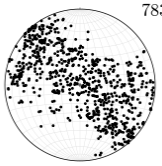


0486_4
267.12m

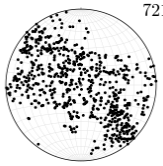


0486_5
267.21m

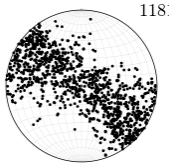


0486_6
267.3m

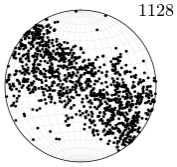


0495_1
271.79m

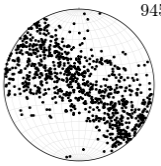


0495_2
271.88m

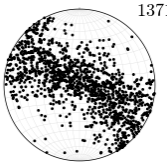


0495_3
271.98m

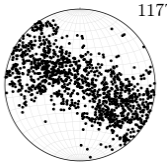


0495_4
272.07m

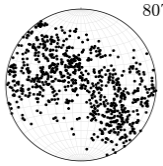


0495_5
272.16m

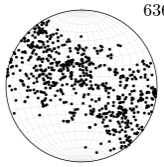


0495_6
272.25m

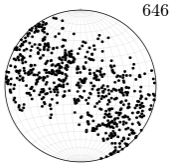


0504_1
276.74m

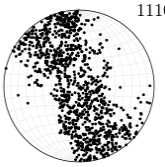


0504_2
276.83m

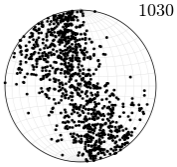


0504_3
276.93m

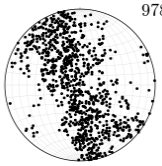


0504_4
277.02m

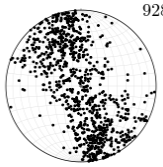


0504_5
277.11m

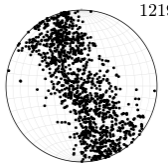


0504_6
277.2m

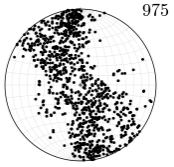


0505_1
277.29m

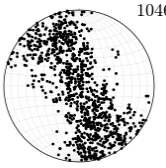


0505_2
277.38m

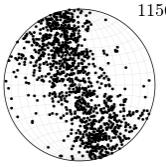


0505_3
277.48m

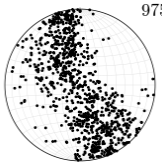


0505_4
277.57m

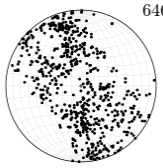


0505_5
277.66m

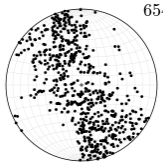


0505_6
277.75m

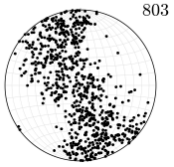


0526_1
288.84m

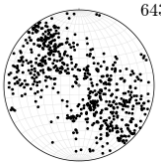


0526_2
288.93m

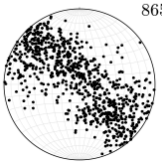


0526_3
289.02m

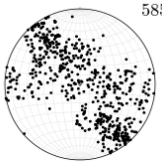


0526_4
289.12m

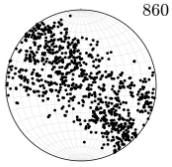


0526_5
289.21m

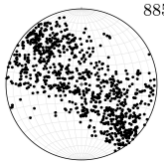

0526_6
289.3m

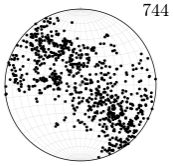


0535_1
293.79m

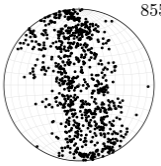


0535_2
293.88m

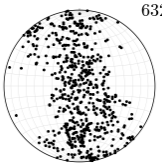


0535_3
293.98m

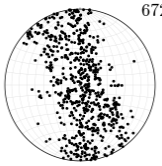


0535_4
294.07m

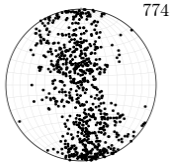


0535_5
294.16m

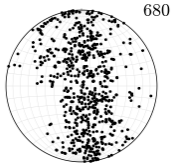


0535_6
294.25m

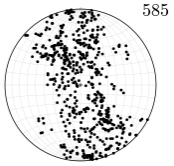


0550_1
302.04m

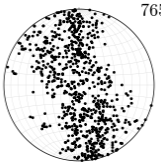


0550_2
302.13m

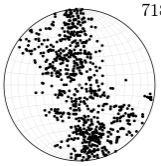


0550_3
302.23m

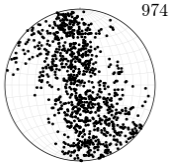


0550_4
302.32m

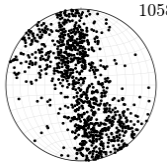


0550_5
302.41m

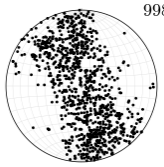


0550_6
302.5m

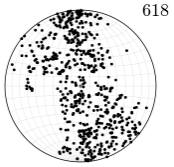


0551_1
302.59m

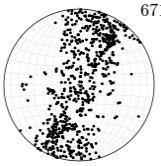


0551_2
302.68m

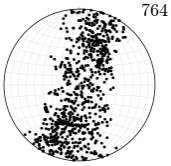


0551_3
302.77m

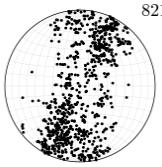


0551_4
302.87m

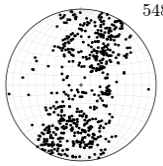


0551_5
302.96m

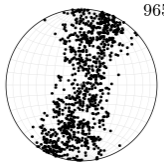


0551_6
303.05m

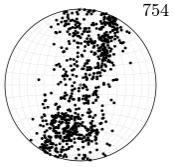


0566_1
310.84m

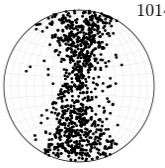


0566_2
310.93m

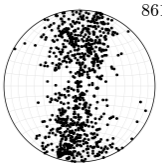


0566_3
311.02m

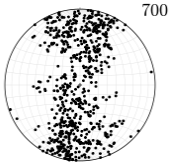


0566_4
311.12m

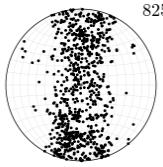


0566_5
311.21m

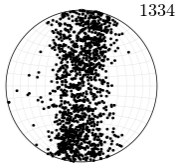


0566_6
311.3m

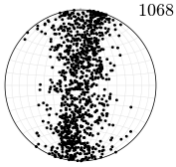


0582_1
319.64m

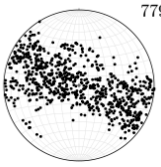


0582_2
319.73m

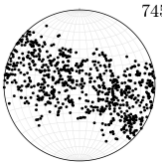


0582_3
319.82m

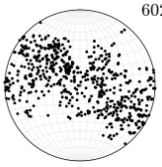


0582_4
319.92m

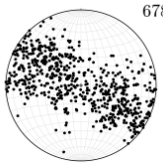


0582_5
320.01m

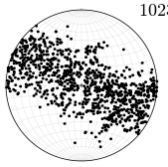

0582_6
320.1m

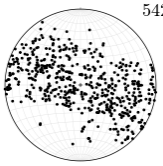


0583_1
320.19m

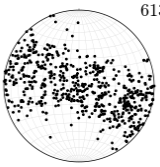


0583_2
320.28m

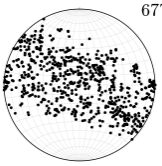


0583_3
320.38m

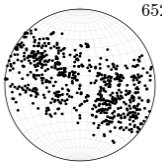


0583_4
320.47m

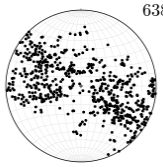


0583_5
320.56m

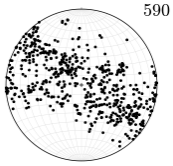


0583_6
320.65m

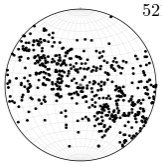


0596_1
327.34m

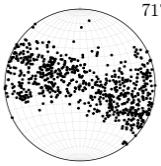


0596_2
327.43m

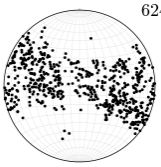


0596_3
327.52m

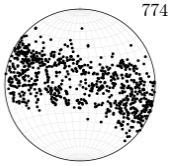


0596_4
327.62m

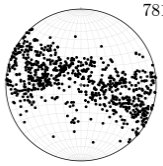


0596_5
327.71m

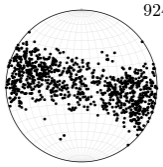


0596_6
327.8m

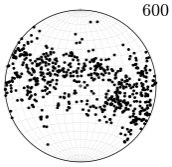


0597_1
327.89m

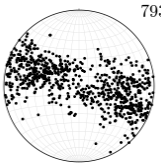


0597_2
327.98m

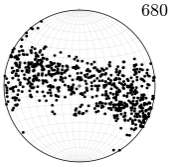


0597_3
328.07m

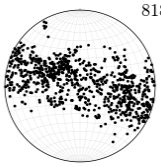


0597_4
328.17m

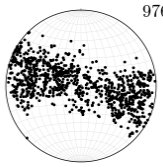


0597_5
328.26m

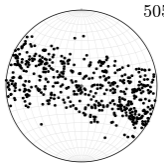


0597_6
328.35m

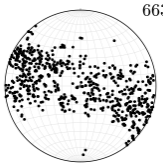


0599_1
328.99m

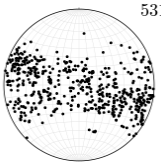


0599_2
329.08m

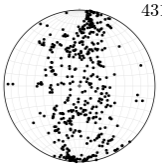


0599_3
329.18m

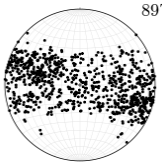


0616_1
338.34m

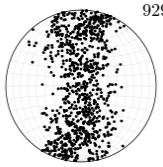


0616_2
338.43m

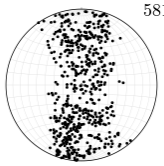


0616_3
338.52m

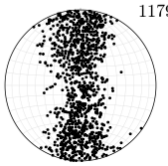


0616_4
338.62m

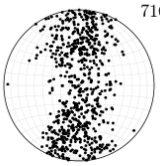


0616_5
338.71m

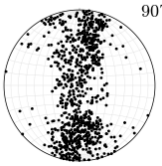


0616_6
338.8m

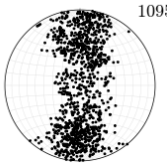


0636_1
349.34m

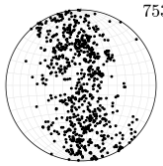


0636_2
349.43m

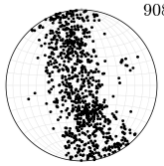

0636_3
349.52m

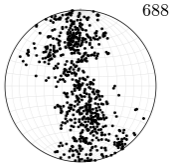


0636_4
349.62m

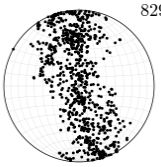


0636_5
349.71m

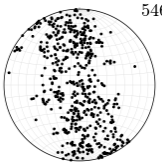


0636_6
349.8m

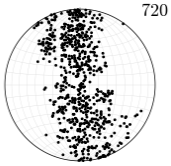


0646_1
354.84m

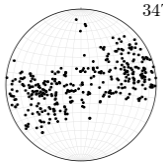


0646_2
354.93m

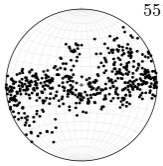


0646_3
355.03m

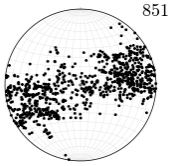


0646_4
355.12m

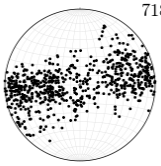


0646_5
355.21m

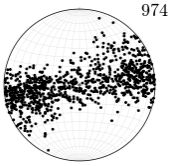


0646_6
355.3m

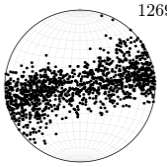


0657_1
360.89m

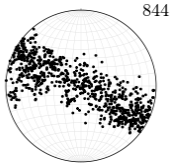


0657_2
360.98m

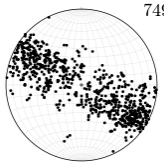


0657_3
361.07m

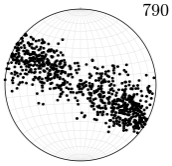


0657_4
361.17m

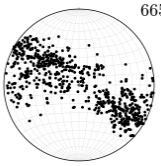


0657_6
361.35m

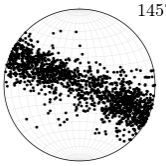


0666_1
365.84m

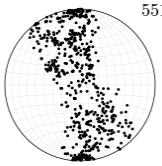


0666_2
365.93m

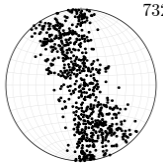


0666_3
366.03m

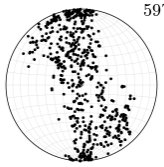


0666_4
366.12m

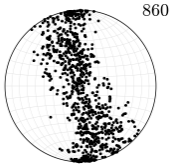


0666_5
366.21m

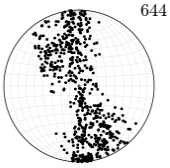


0666_6
366.3m

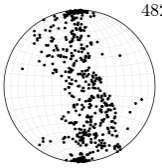


0686_1
376.84m

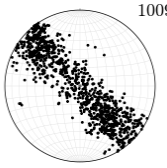


0686_2
376.93m

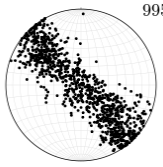


0686_3
377.03m

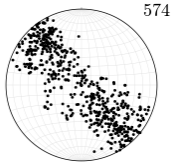


0686_4
377.12m

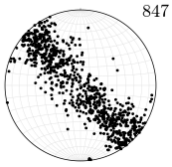


0686_5
377.21m

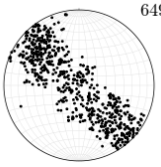


0686_6
377.3m

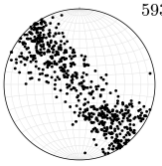


0724_1
397.74m

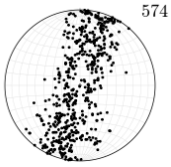


0724_2
397.83m

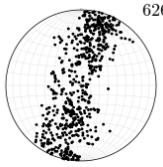


0724_3
397.93m

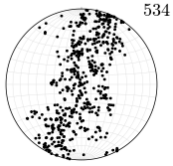

0724_4
398.02m

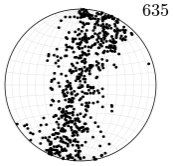


0724_5
398.11m

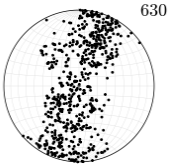


0724_6
398.2m

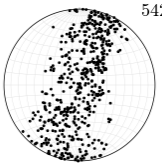


0756_1
415.34m

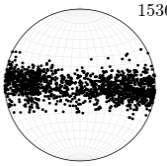


0756_2
415.43m

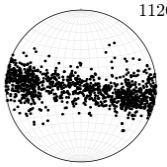


0756_3
415.53m

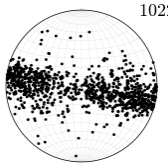


0756_4
415.62m

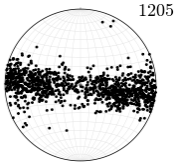


0756_5
415.71m

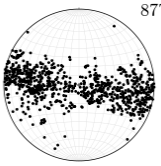


0756_6
415.8m

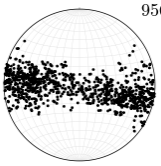


0776_1
426.34m

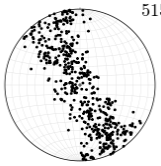


0776_2
426.43m

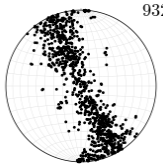


0776_3
426.53m

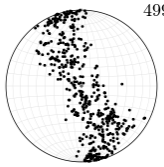


0776_4
426.62m

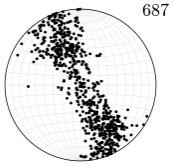


0776_5
426.71m

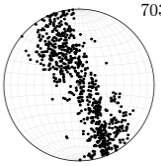


0776_6
426.8m

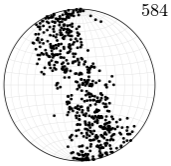


0796_1
437.34m

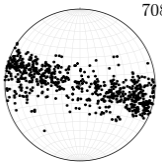


0796_2
437.43m

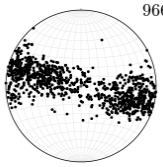


0796_3
437.53m

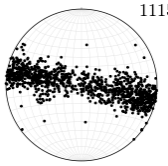


0796_4
437.62m

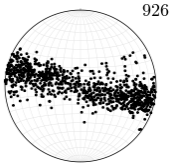


0796_5
437.71m

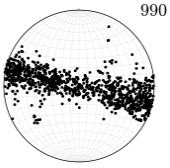


0796_6
437.8m

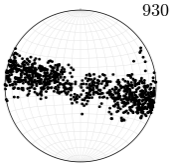


0816_1
448.34m

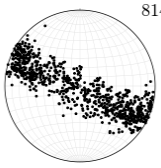


0816_2
448.43m

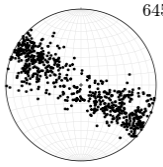


0816_3
448.53m

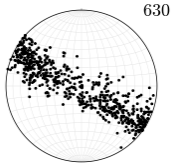


0816_4
448.62m

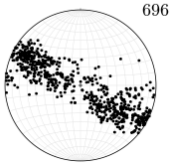


0816_5
448.71m

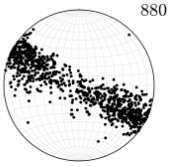


0816_6
448.8m

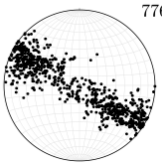


0836_1
459.34m

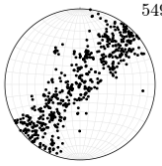


0836_2
459.43m

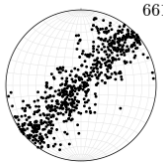


0836_3
459.53m

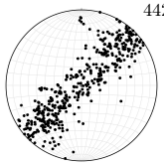

0836_4
459.62m

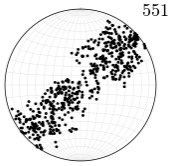


0836_5
459.71m

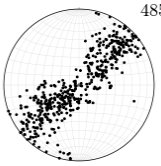


0836_6
459.8m

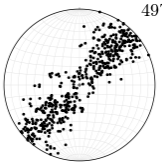


0837_1
459.89m

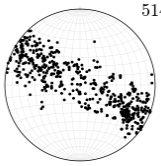


0837_2
459.98m

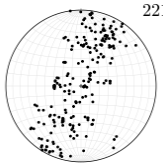


0837_3
460.07m

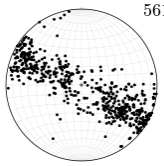


0866_1
475.84m

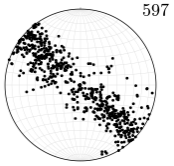


0866_2
475.93m

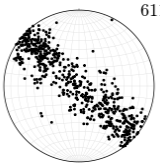


0866_3
476.03m

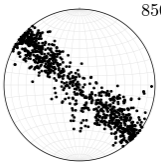


0866_4
476.12m

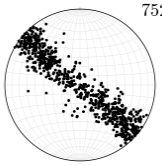


0866_5
476.21m

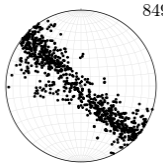


0866_6
476.3m

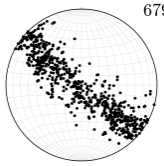


0896_1
492.34m

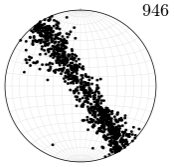


0896_2
492.43m

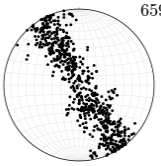


0896_3
492.53m

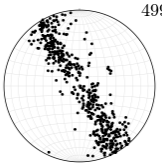


0896_4
492.62m

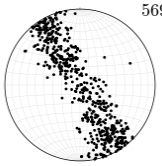


0896_5
492.71m

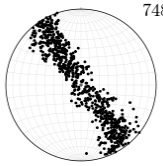


0896_6
492.8m

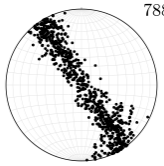


0936_1
514.34m

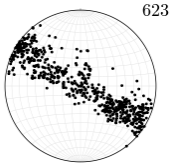


0936_2
514.43m

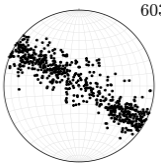


0936_3
514.52m

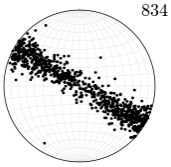


0936_4
514.62m

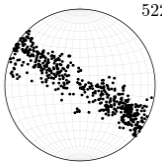


0936_5
514.71m

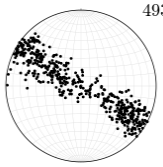


0936_6
514.8m

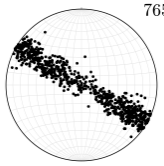


0956_1
525.34m

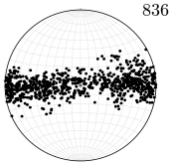


0956_2
525.43m

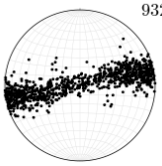


0956_3
525.52m

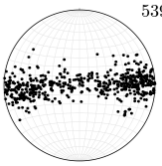


0956_4
525.62m

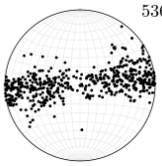


0956_5
525.71m

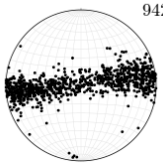


0956_6
525.8m

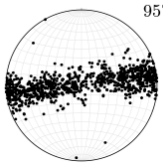

0977_1
536.89m

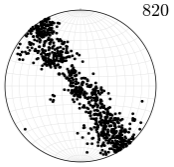


0977_2
536.98m

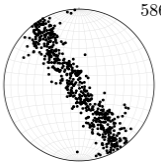


0977_3
537.08m

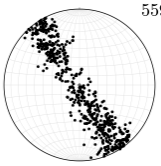


0977_4
537.17m

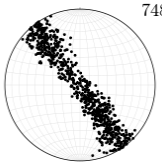


0977_5
537.26m

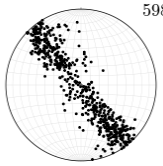


0977_6
537.35m

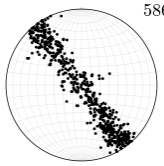


0995_1
546.79m

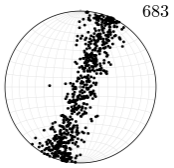


0995_2
546.88m

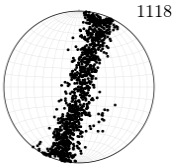


0995_3
546.98m

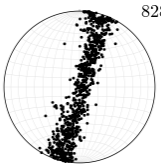


0995_4
547.07m

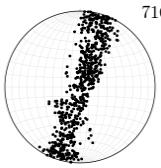


0995_5
547.16m

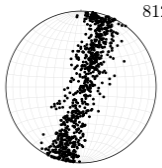


0995_6
547.25m

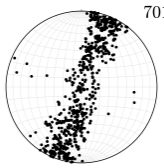


1000_1
549.54m

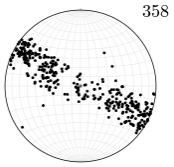


1000_2
549.63m

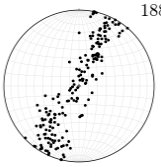


1000_3
549.73m

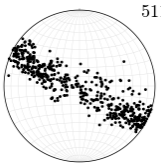


1016_1
558.34m

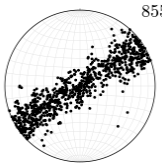


1016_2
558.43m

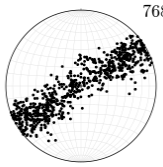


1016_3
558.52m

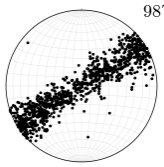


1016_4
558.62m

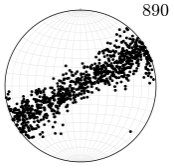


1016_5
558.71m

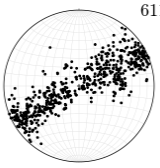


1016_6
558.8m

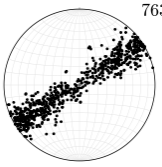


1057_1
580.89m

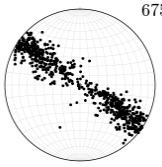


1057_2
580.98m

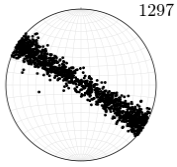


1057_3
581.08m

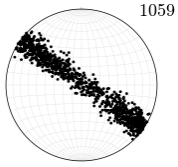


1057_4
581.17m

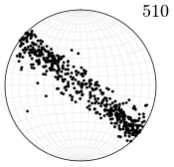


1057_5
581.26m

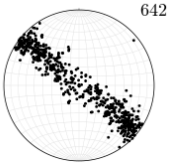


1057_6
581.35m

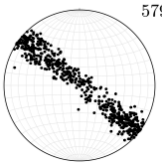


1096_1
602.34m

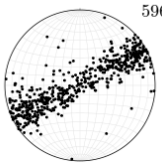


1096_2
602.43m

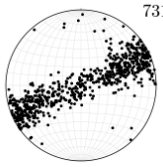


1096_3
602.52m

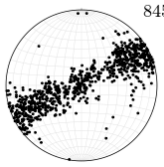

1096_4
602.62m

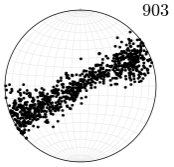


1096_5
602.71m

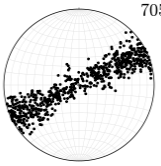


1096_6
602.8m

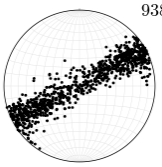


1116_1
613.34m

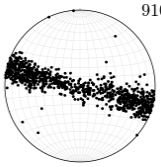


1116_2
613.43m

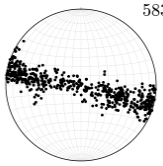


1116_3
613.52m

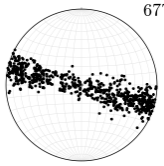


1116_4
613.62m

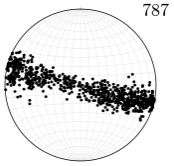


1116_5
613.71m

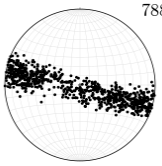


1116_6
613.8m

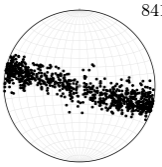


1146_1
629.84m

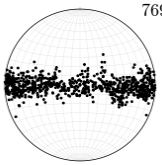


1146_2
629.93m

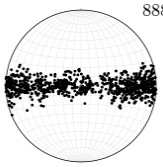


1146_3
630.02m

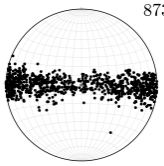


1146_4
630.12m

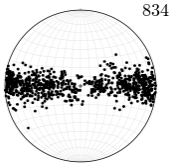


1146_5
630.21m

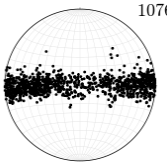


1146_6
630.3m

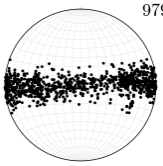


1174_stereo.png
NAm

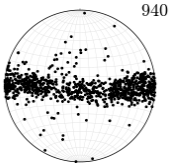


1185_1
651.29m

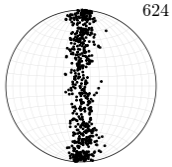


1185_2
651.38m

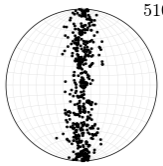


1185_3
651.48m

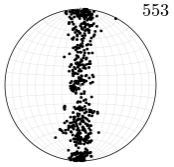


1185_4
651.57m

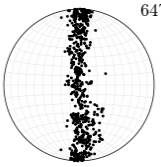


1185_5
651.66m

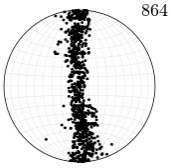


1185_6
651.75m

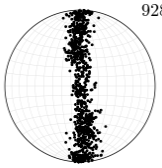


1208_1
663.94m

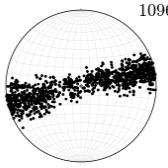


1208_2
664.03m

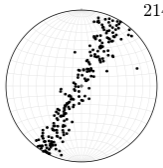


1208_3
664.12m

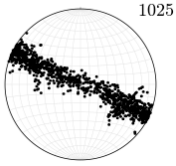


1214_1
667.24m

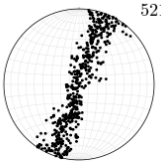


1214_2
667.33m

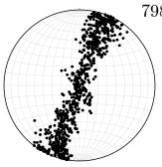


1214_3
667.43m

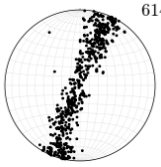


1214_4
667.52m

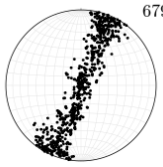


1214_5
667.61m

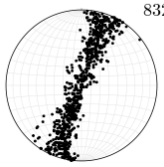

1214_6
667.7m

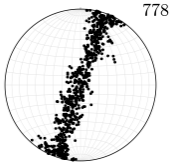


1247_1
685.39m

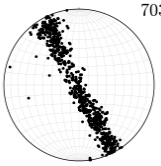


1247_2
685.48m

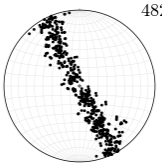


1247_3
685.58m

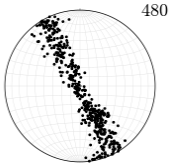


1247_4
685.67m

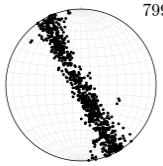


1247_5
685.76m

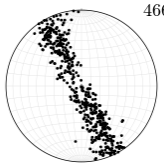


1247_6
685.85m

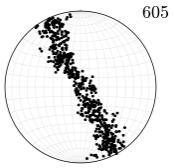


1276_1
701.34m

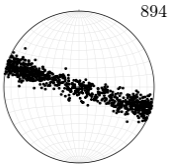


1276_2
701.43m

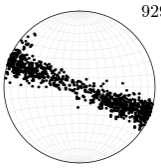


1276_3
701.52m

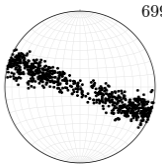


1276_4
701.62m

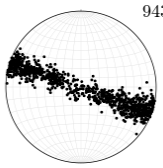


1276_5
701.71m

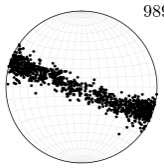


1276_6
701.8m

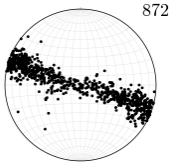


1315_1
722.79m

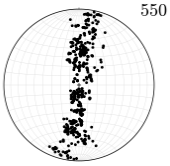


1315_2
722.88m

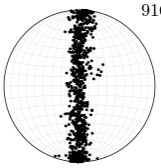


1315_3
722.98m

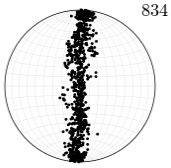


1315_4
723.07m

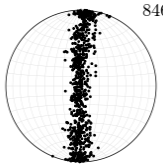


1315_5
723.16m

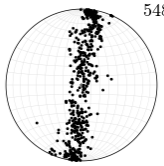


1315_6
723.25m

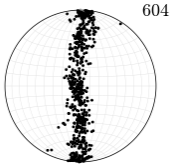


1346_1
739.84m

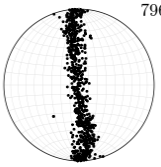


1346_2
739.93m

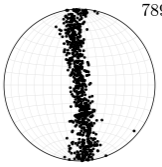


1346_3
740.03m

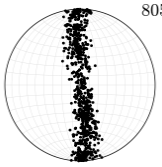


1346_4
740.12m

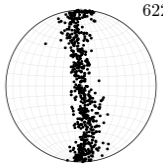


1346_5
740.21m

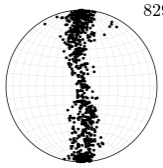


1346_6
740.3m

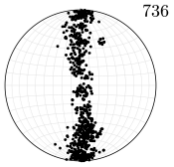


1377_1
756.89m

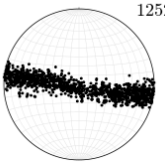


1377_2
756.98m

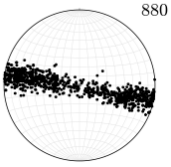


1377_3
757.08m

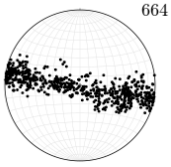


1377_4
757.17m

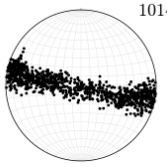


1377_5
757.26m

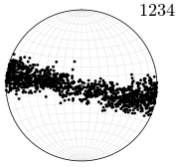

1377_6
757.35m

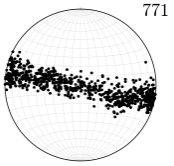


1400_1
769.54m

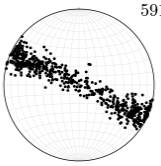


1400_2
769.63m

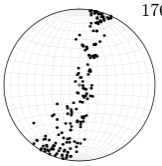


1400_3
769.73m

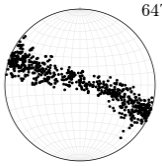


1406_1
772.84m

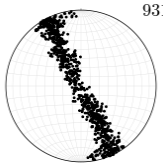


1406_2
772.93m

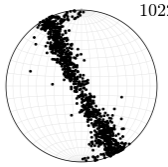


1406_3
773.03m

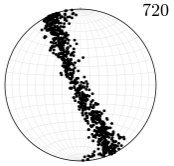


1406_4
773.12m

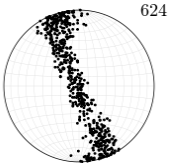


1406_5
773.21m

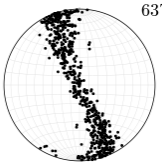


1406_6
773.3m

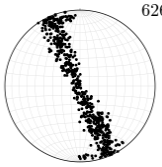


1444_3
793.93m

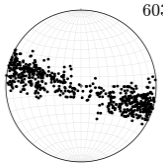


1444_4
794.02m

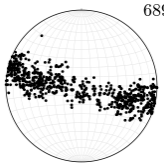


1444_5
794.11m

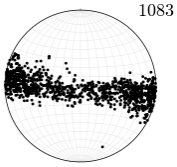


1444_6
794.2m

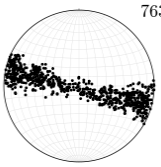


1475_1
810.79m

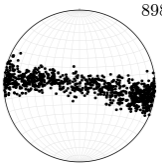


1475_2
810.88m

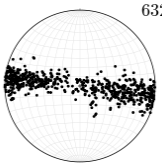


1475_3
810.98m

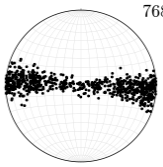


1475_4
811.07m

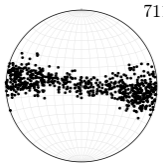


1475_5
811.16m

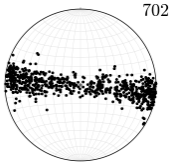


1475_6
811.25m

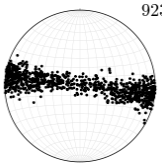


1507_1
828.39m

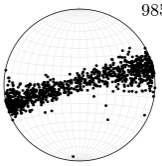


1507_3
828.58m

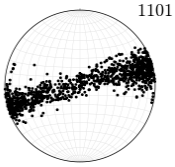


1507_4
828.67m

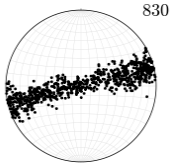


1507_5
828.76m

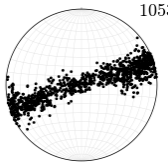


1507_6
828.85m

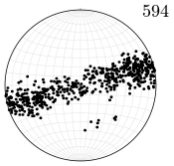


1546_1
849.84m

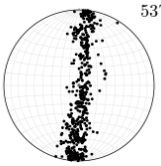


1546_2
849.93m

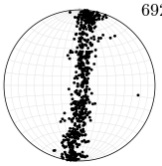


1546_3
850.03m

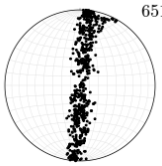


1546_4
850.12m

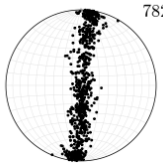


1546_5
850.21m

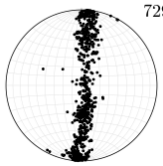

1546_6
850.3m

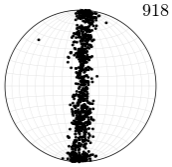


1558_1
856.44m

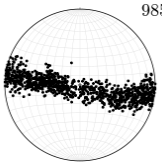


1558_2
856.53m

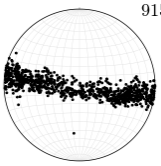


1558_3
856.62m

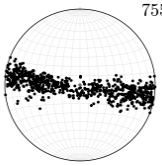


1558_4
856.72m

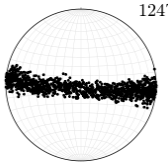


1558_5
856.81m

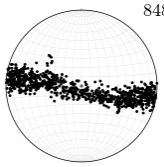


1558_6
856.9m

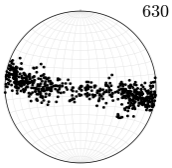


1588_1
872.94m

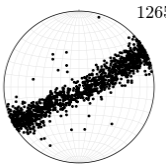


1588_2
873.03m

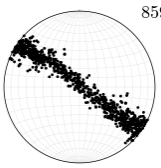


1588_3
873.12m

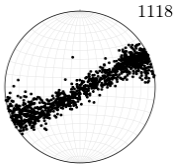


1588_4
873.22m

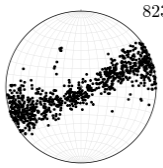


1588_6
873.4m

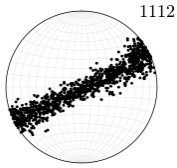


1606_1
882.84m

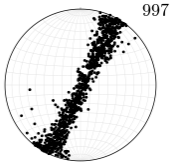


1606_2
882.93m

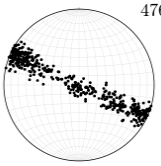


1606_3
883.03m

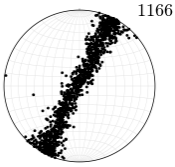


1615_1
887.79m

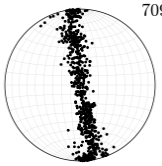


1615_2
887.88m

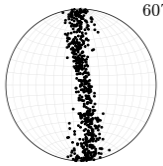


1615_3
887.98m

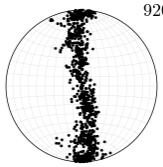


1615_4
888.07m

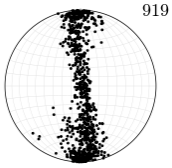


1615_5
888.16m

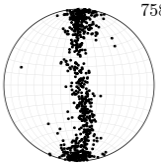


1615_6
888.25m

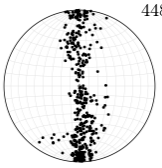


1637_1
899.89m

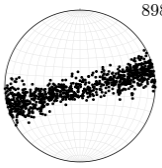


1637_2
899.98m

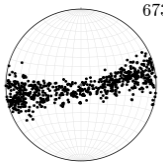


1637_3
900.08m

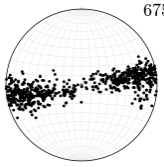


1637_4
900.17m

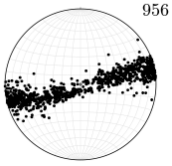


1637_5
900.26m

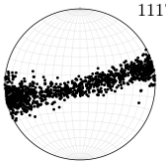


1637_6
900.35m

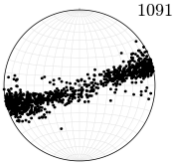


1933_1
1062.69m

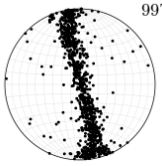


1933_2
1062.78m

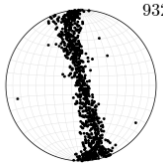


1933_3
1062.88m

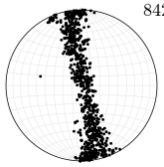

1933_4
1062.97m

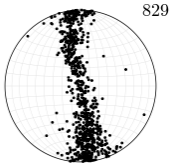


1933_5
1063.06m

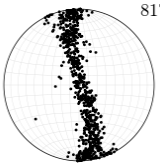


1933_6
1063.15m

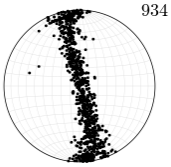


1965_1
1080.29m

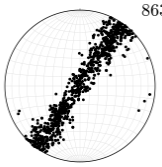


1965_2
1080.38m

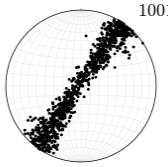


1965_3
1080.48m

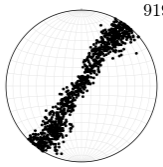


1965_4
1080.57m

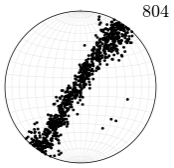


1965_5
1080.66m

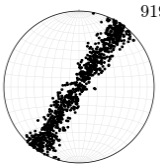


1965_6
1080.75m

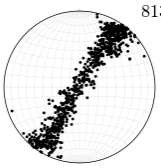


1996_1
1097.34m

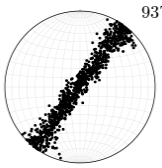


1996_2
1097.43m

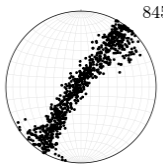


1996_4
1097.62m

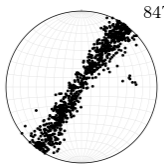


1996_5
1097.71m

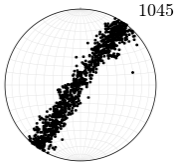


1996_6
1097.8m

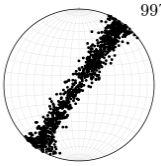


2026_1
1113.84m

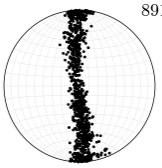


2026_2
1113.93m

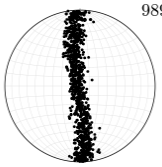


2026_3
1114.03m

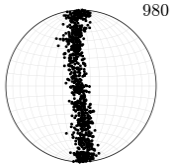


2026_4
1114.12m

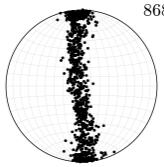


2026_5
1114.21m

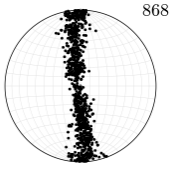


2026_6
1114.3m

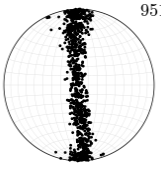


2056_1
1130.34m

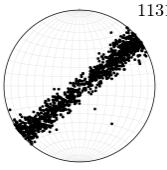


2056_2
1130.43m

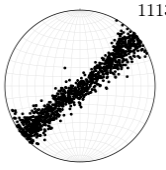


2056_3
1130.53m

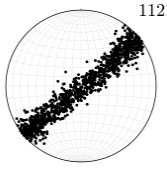


2056_4
1130.62m

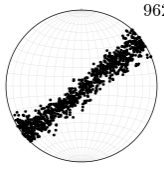


2056_5
1130.71m

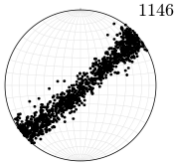


2056_6
1130.8m

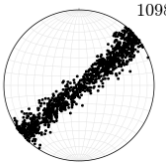


2075_1
1140.79m

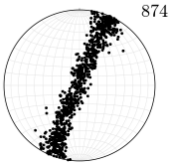


2075_2
1140.88m

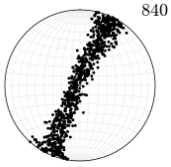


2075_3
1140.98m

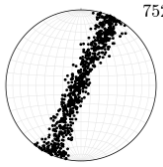


2075_4
1141.07m

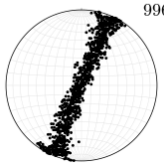

2075_5
1141.16m

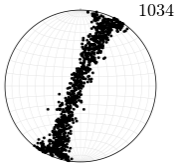


2075_6
1141.25m

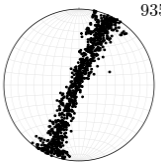


2106_1
1157.84m

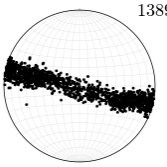


2106_2
1157.93m

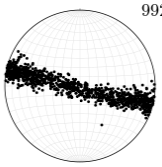


2106_3
1158.03m

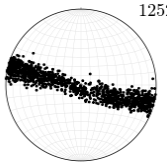


2106_4
1158.12m

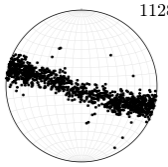


2106_5
1158.21m

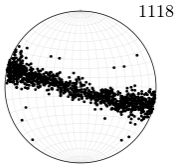


2106_6
1158.3m

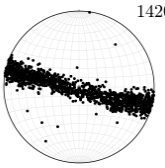


2136_1
1174.34m

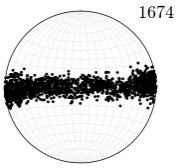


2136_2
1174.43m

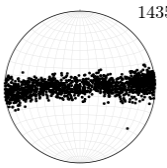


2136_3
1174.53m

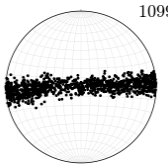


2136_4
1174.62m

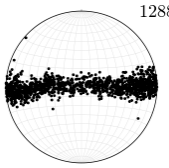


2136_5
1174.71m

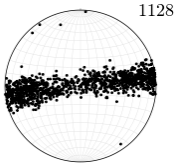


2136_6
1174.8m

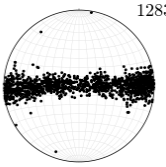


2156_1
1185.34m

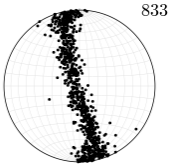


2156_2
1185.43m

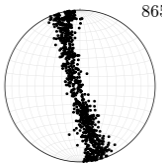


2156_3
1185.53m

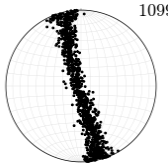


2156_4
1185.62m

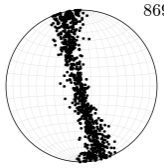


2156_5
1185.71m

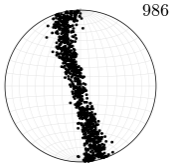


2156_6
1185.8m

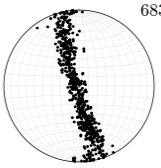


2176_1
1196.34m

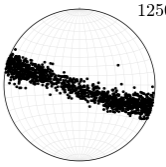


2176_2
1196.43m

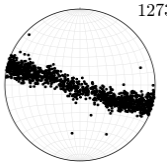


2176_3
1196.53m

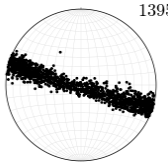


2176_4
1196.62m

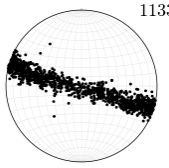


2176_5
1196.71m

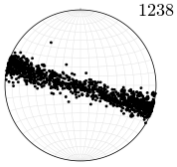


2176_6
1196.8m

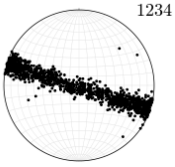


2206_1
1212.84m

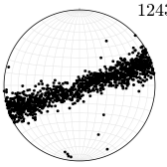


2206_2
1212.93m

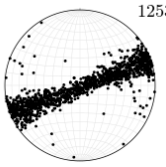


2206_3
1213.03m

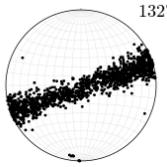


2206_4
1213.12m

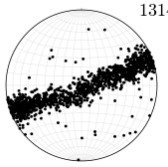

2206_5
1213.21m

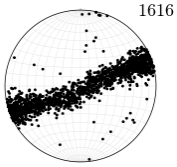


2206_6
1213.3m

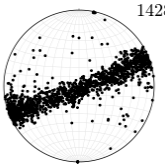


2221_1
1221.09m

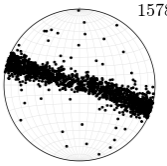


2221_2
1221.18m

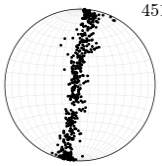


2221_3
1221.28m

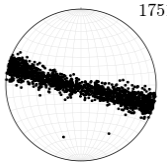


2222_1
1221.64m

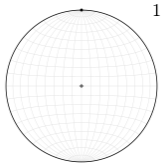


2236_1
1229.34m

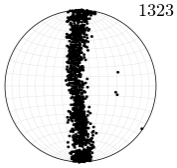


2236_2
1229.43m

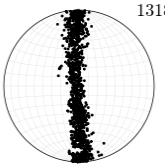


2236_3
1229.53m

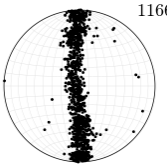


2236_4
1229.62m

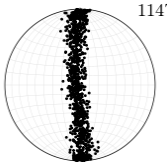


2236_5
1229.71m

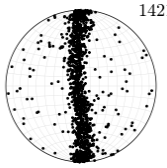


2236_6
1229.8m

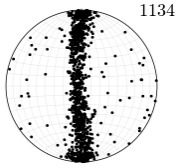


2256_1
1240.34m

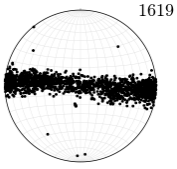


2256_2
1240.43m

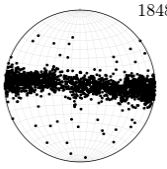


2256_3
1240.53m

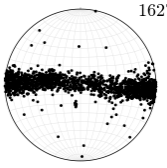


2256_4
1240.62m

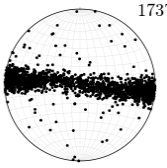


2256_5
1240.71m

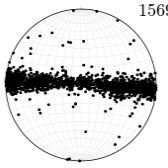


2256_6
1240.8m

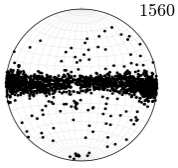


2286_1
1256.84m

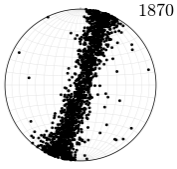


2286_2
1256.93m

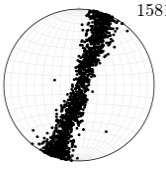


2286_3
1257.03m

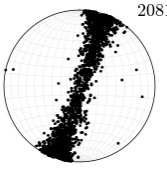


2286_4
1257.12m

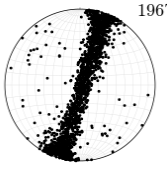


2286_5
1257.21m

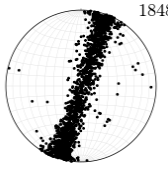


2286_6
1257.3m

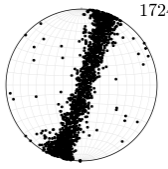


2316_1
1273.34m

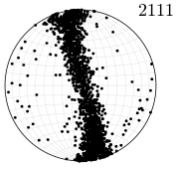


2316_2
1273.43m

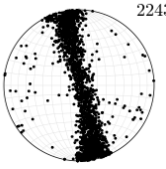


2316_3
1273.53m

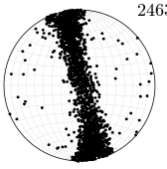


2316_4
1273.62m

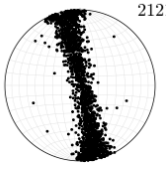


2316_5
1273.71m

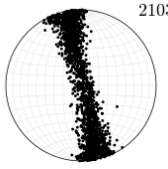


2316_6
1273.8m

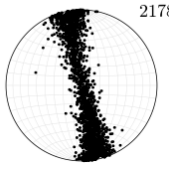

2356_1
1295.34m

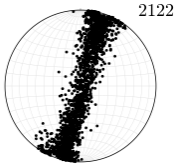


2356_2
1295.43m

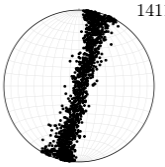


2356_3
1295.53m

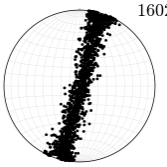


2356_4
1295.62m

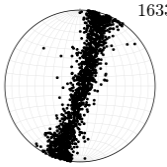


2356_5
1295.71m

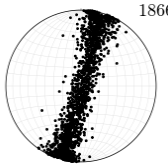


2356_6
1295.8m

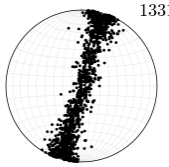


2386_1
1311.84m

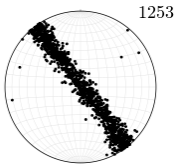


2386_2
1311.93m

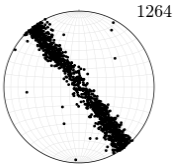


2386_3
1312.03m

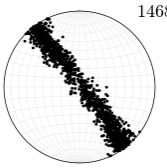


2386_4
1312.12m

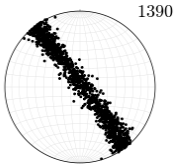


2386_5
1312.21m

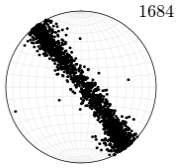


2386_6
1312.3m

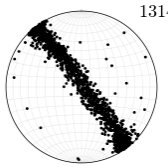


2416_1
1328.34m

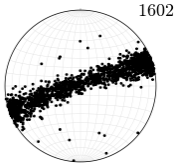


2416_2
1328.43m

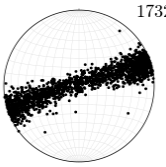


2416_3
1328.53m

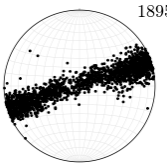


2416_4
1328.62m

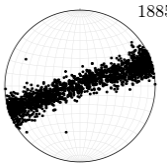


2416_5
1328.71m

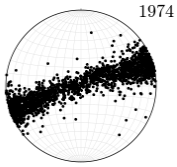


2416_6
1328.8m

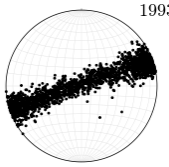


2436_1
1339.34m

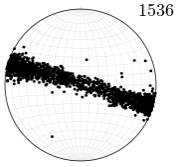


2436_2
1339.43m

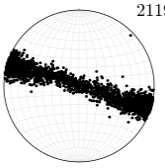


2436_3
1339.53m

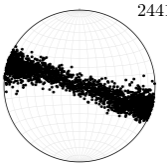


2436_4
1339.62m

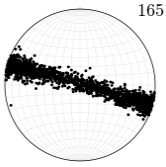


2436_5
1339.71m

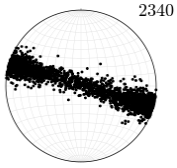


2436_6
1339.8m

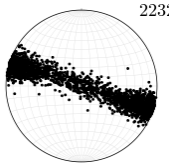


2446_1
1344.84m

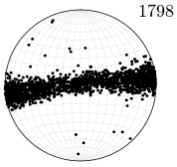


2446_2
1344.93m

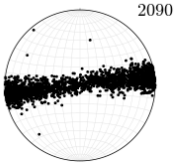


2446_3
1345.03m

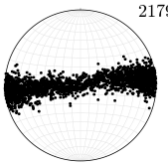


2446_4
1345.12m

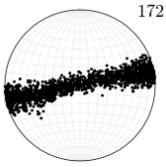


2446_5
1345.21m

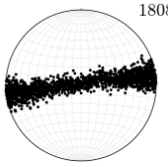


2446_6
1345.3m

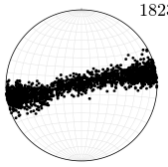

2475_1
1360.79m

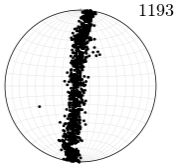


2475_2
1360.88m

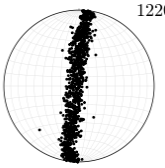


2475_3
1360.98m

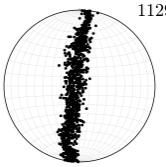


2475_4
1361.07m

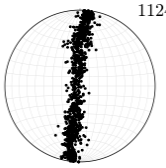


2475_5
1361.16m

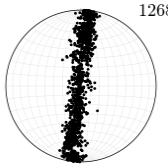


2475_6
1361.25m

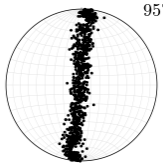


2486_1
1366.84m

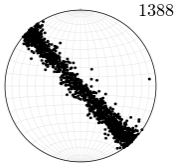


2486_2
1366.93m

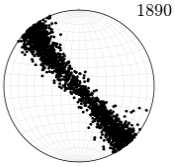


2486_3
1367.03m

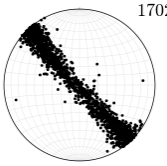


2486_4
1367.12m

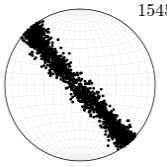


2486_5
1367.21m

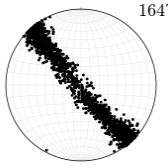


2486_6
1367.3m

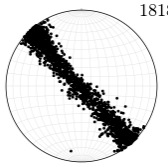


2506_1
1377.84m

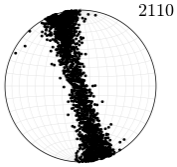


2506_2
1377.93m

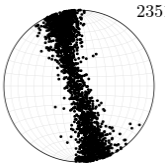


2506_3
1378.03m

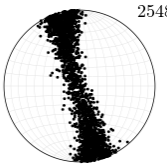


2506_4
1378.12m

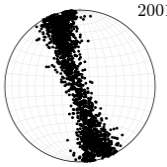


2506_5
1378.21m

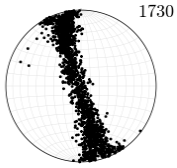


2506_6
1378.3m

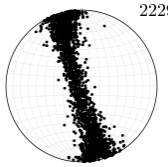


2535_1
1393.79m

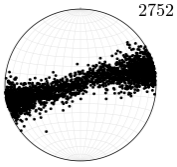


2535_2
1393.88m

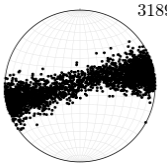


2535_3
1393.98m

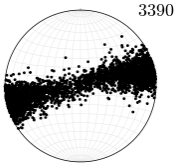


2535_4
1394.07m

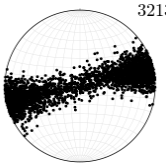


2535_5
1394.16m

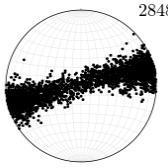


2535_6
1394.25m

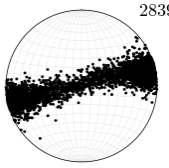


2565_1
1410.29m

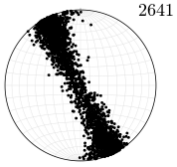


2565_2
1410.38m

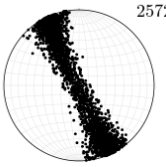


2565_3
1410.48m

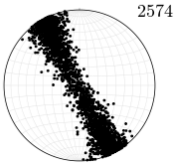


2565_4
1410.57m

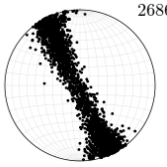


2565_5
1410.66m

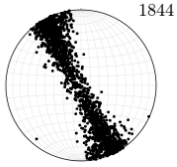


2565_6
1410.75m

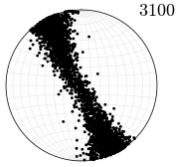

2596_1
1427.34m

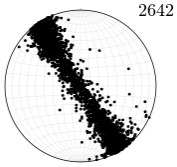


2596_2
1427.43m

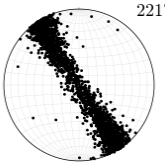


2596_3
1427.53m

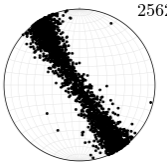


2596_4
1427.62m

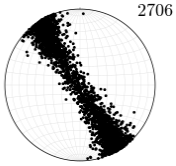


2596_5
1427.71m

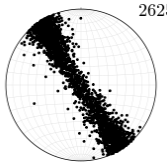


2596_6
1427.8m

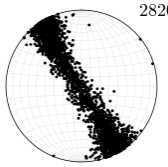


2600_1
1429.54m

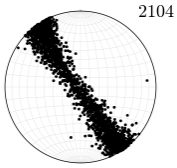


2600_2
1429.63m

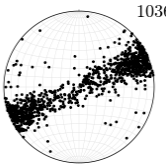


2600_3
1429.73m

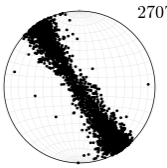


2600_4
1429.82m

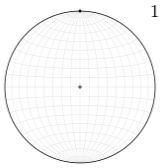


2600_5
1429.91m

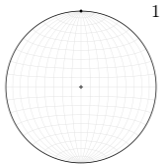


2600_6
1430m

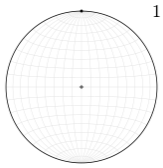


2626_1
1443.84m

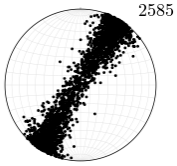


2626_2
1443.93m

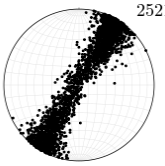


2626_3
1444.03m

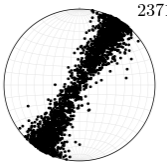


2626_4
1444.12m

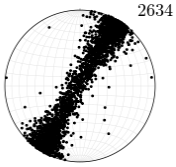


2626_5
1444.21m

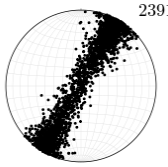


2626_6
1444.3m

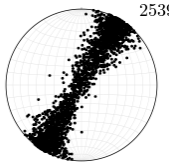


2635_1
1448.79m

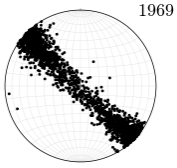


2635_2
1448.88m

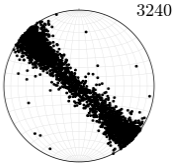


2635_3
1448.98m

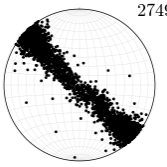


2635_4
1449.07m

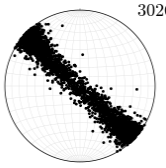


2635_5
1449.16m

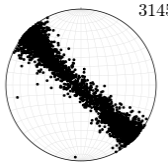


2635_6
1449.25m

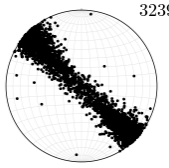


2666_1
1465.84m

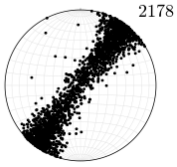


2666_2
1465.93m

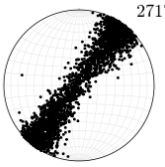


2666_3
1466.03m

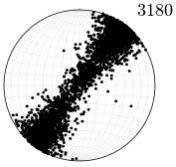


2666_4
1466.12m

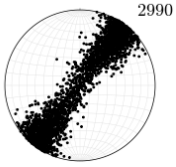


2666_5
1466.21m

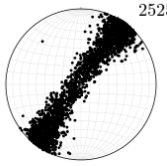


2666_6
1466.3m

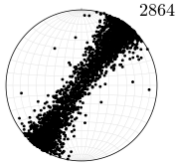

2696_1
1482.34m

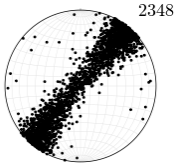


2696_2
1482.43m

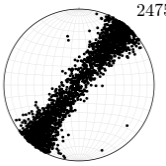


2696_3
1482.53m

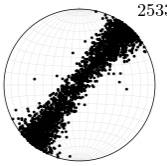


2696_4
1482.62m

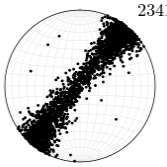


2696_5
1482.71m

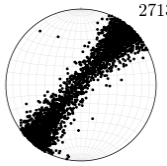


2696_6
1482.8m

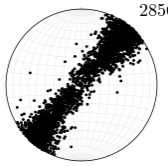


2726_1
1498.84m

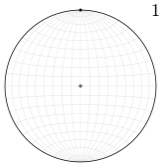


2726_2
1498.93m

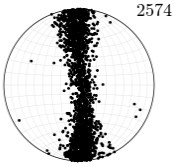


2726_3
1499.03m

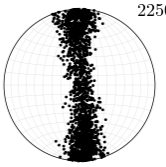


2726_4
1499.12m

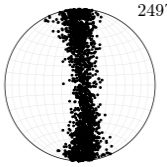


2726_5
1499.21m

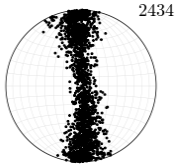


2726_6
1499.3m

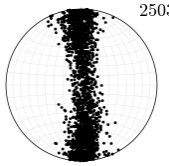


2756_1
1515.34m

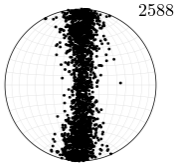


2756_2
1515.43m

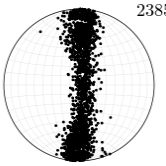


2756_3
1515.53m

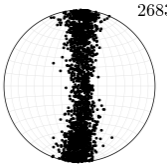


2756_4
1515.62m

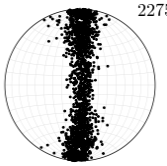


2756_5
1515.71m

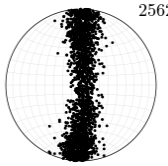


2756_6
1515.8m

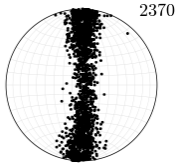


2786_1
1531.84m

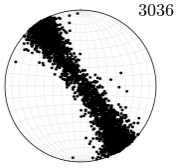


2786_2
1531.93m

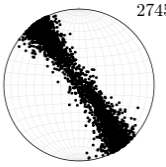


2786_3
1532.03m

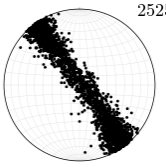


2786_4
1532.12m

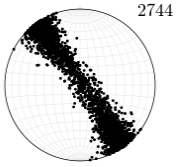


2786_5
1532.21m

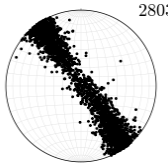


2786_6
1532.3m

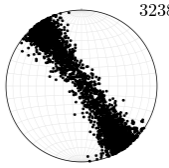


2817_1
1548.89m

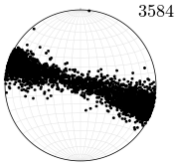


2817_2
1548.98m

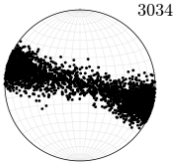


2817_3
1549.08m

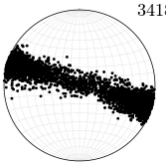


2817_4
1549.17m

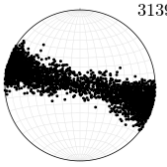


2817_5
1549.26m

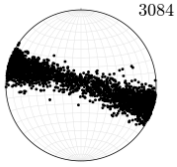


2817_6
1549.35m

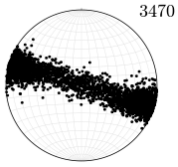

2846_1
1564.84m

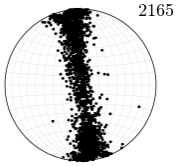


2846_2
1564.93m

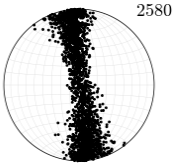


2846_3
1565.03m

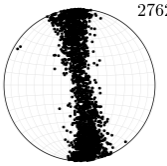


2846_4
1565.12m

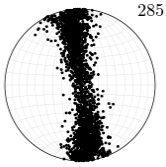


2846_5
1565.21m

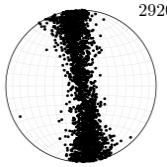


2846_6
1565.3m

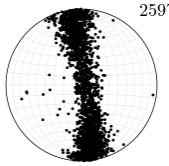


2876_1
1581.34m

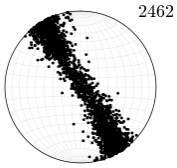


2876_2
1581.43m

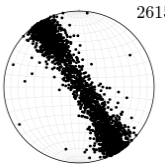


2876_3
1581.53m

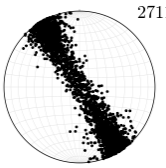


2876_4
1581.62m

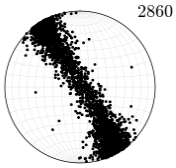


2876_5
1581.71m

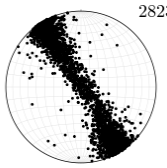


2876_6
1581.8m

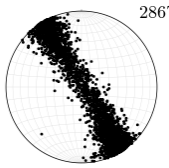


2906_1
1597.84m

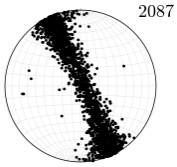


2906_2
1597.93m

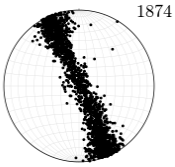


2906_3
1598.03m

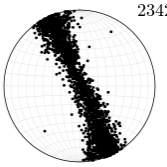


2906_4
1598.12m

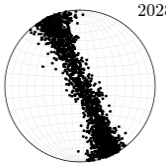


2906_5
1598.21m

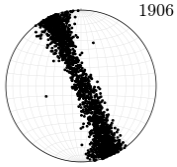


2906_6
1598.3m

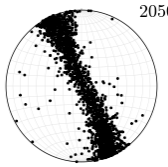


2936_1
1614.34m

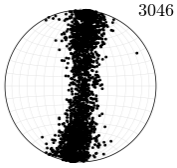


2936_2
1614.43m

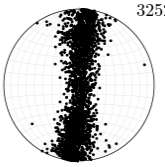


2936_3
1614.53m

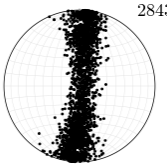


2936_4
1614.62m

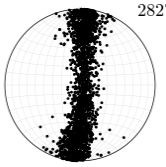


2936_5
1614.71m

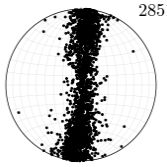


2936_6
1614.8m

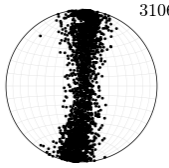


2966_1
1630.84m

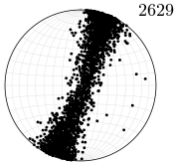


2966_2
1630.93m

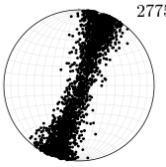


2966_3
1631.03m

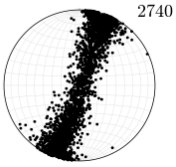


2966_4
1631.12m

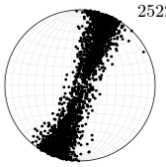


2966_5
1631.21m

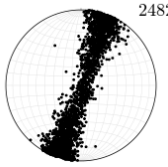


2966_6
1631.3m

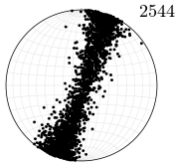

2997_1
1647.89m

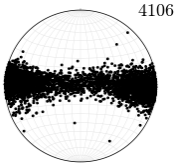


2997_2
1647.98m

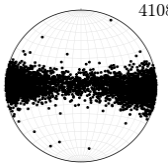


2997_3
1648.08m

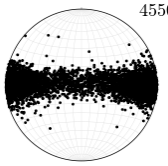


2997_4
1648.17m

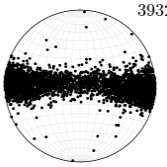


2997_5
1648.26m

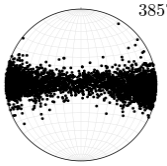


2997_6
1648.35m

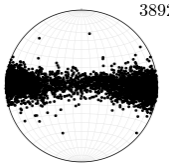


3027_1
1664.39m

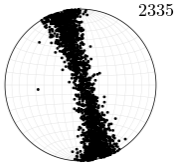


3027_2
1664.48m

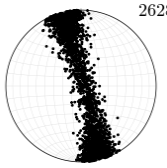


3027_3
1664.58m

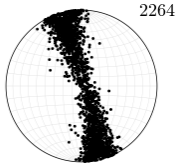


3027_4
1664.67m

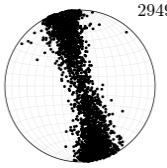


3027_5
1664.76m

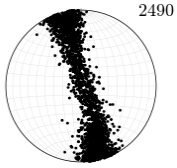


3027_6
1664.85m

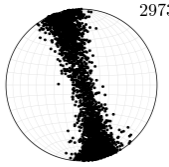


3056_1
1680.34m

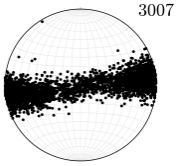


3056_2
1680.43m

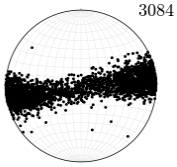


3056_3
1680.53m

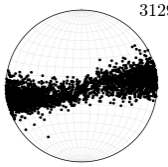


3056_4
1680.62m

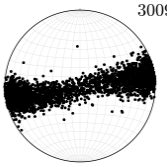


3056_5
1680.71m

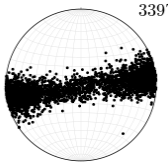


3056_6
1680.8m

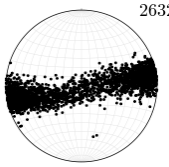


3086_1
1696.84m

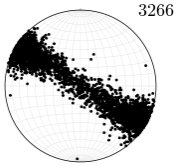


3086_2
1696.93m

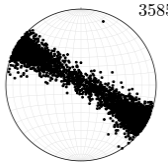


3086_3
1697.03m

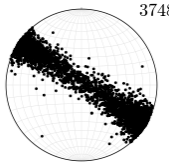


3086_4
1697.12m

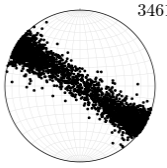


3086_5
1697.21m

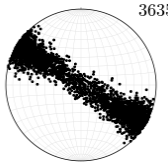


3086_6
1697.3m

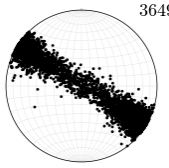


3117_1
1713.89m

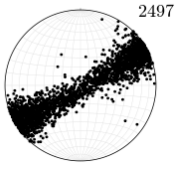


3117_2
1713.98m

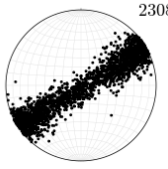


3117_3
1714.08m

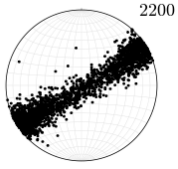


3117_4
1714.17m

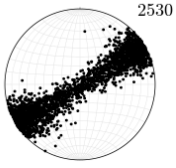


3117_5
1714.26m

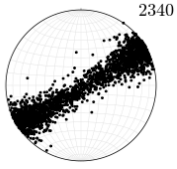


3117_6
1714.35m